

The role of semaphorin-3A in the development of metabolic dysfunction-associated steatotic liver disease (MASLD)

Inaugural-Dissertation

zur Erlangung des Doktorgrades
der Mathematisch-Naturwissenschaftlichen Fakultät
der Heinrich-Heine-Universität Düsseldorf

vorgelegt von

Sydney Miriam Balkenhol

aus Erfurt

Düsseldorf, August 2024

aus dem Institut für Stoffwechselfysiologie
der Heinrich-Heine-Universität Düsseldorf

Gedruckt mit der Genehmigung der
Mathematisch-Naturwissenschaftlichen Fakultät der
Heinrich-Heine-Universität Düsseldorf

Berichtersteller:

1. Prof. Dr. Eckhard Lammert

2. Prof. Dr. Simone Prömel

Tag der mündlichen Prüfung

Table of Contents

Table of Contents	I
Annotations to this thesis	V
1. Summary	1
2. Zusammenfassung	2
3. Introduction	4
3.1. Liver	4
3.1.1. Mouse <i>versus</i> human liver.....	7
3.1.2. Lipid metabolism	8
3.2. Liver sinusoidal endothelial cells	9
3.2.1. Fenestrae	10
3.3. Metabolic dysfunction-associated steatotic liver disease.....	13
3.3.1. Development of MASLD	14
3.3.2. Treatment/Interventions for MASLD	17
3.3.3. LSECs in diseases	18
3.4. The semaphorins	19
3.4.1. Semaphorin protein family	19
3.4.2. Semaphorin-3A.....	22
3.4.3. Semaphorin-3A in diseases.....	23
3.5. Aim of this Thesis.....	25
4. Methods	27
4.1. Magnetic-activated cell sorting of mouse LSECs.....	27
4.1.1. Liver dissociation	27
4.1.2. Magnetic labelling and separation	27
4.2. Cell culture.....	28
4.2.1. SEMA3A-Fc treatment of mouse LSECs	28
4.2.2. Antibody, inhibitor, and serum treatments of LSECs	29

4.3.	Palmitic acid treatment of human LSECs	30
4.4.	SEM analysis	30
4.4.1.	Preparation for SEM analysis of cells	30
4.4.2.	Manual fenestrae quantification of LSECs	31
4.4.3.	Fenestrae quantification of LSECs using a deep learning workflow.....	34
4.4.4.	Fenestrae quantification of sinusoids using Fiji WEKA classifier.....	34
4.5.	Gene expression analysis.....	35
4.6.	Western blotting	35
4.6.1.	Protein isolation	35
4.6.2.	Bicinchoninic acid assay.....	36
4.6.3.	Western blotting.....	36
4.7.	PamGene kinase activity profiling	37
4.8.	Phalloidin staining.....	37
4.9.	Measuring corrected total cell fluorescence (CTCF)	38
4.10.	G-actin/F-actin <i>in vivo</i> assay biochem kit	38
4.11.	Serum parameters	38
4.12.	Animal handling.....	39
4.13.	Mouse liver perfusion.....	40
4.14.	VLDL secretion assay.....	41
4.15.	Statistics.....	41
4.16.	Personal contributions.....	42
5.	Results	44
5.1.	LSEC and fenestrae: establishment of quality and analysis	44
5.1.1.	Quality assessment of MACS-isolated mouse LSECs.....	44
5.1.2.	Development of a deep learning workflow for fenestrae analysis	45
5.1.3.	LSECs lose their fenestrae after 24 hours while SEMA3A-Fc treatment does not impair LSEC size or viability.....	48
5.2.	SEMA3A-mediated defenestration: mechanism of action.....	50
5.2.1.	SEMA3A decreases fenestrae frequency in a time- and concentration-dependent manner	50

5.2.2.	Inhibiting the SEMA3A subdomain of NRP1 ameliorates SEMA3A-induced defenestration in LSECs.....	52
5.2.3.	Kinase activity profiling of SEMA3A downstream signalling in LSEC	53
5.2.4.	Cofilin-1 phosphorylation is increased upon SEMA3A treatment	56
5.2.5.	LIMK1 inhibition impedes SEMA3A-induced defenestration in mouse LSECs	57
5.2.6.	Palmitic acid and SEMA3A affect the actin-cytoskeleton in LSECs.....	58
5.3.	The role of <i>Sema3a</i> in the development of MASLD.....	61
5.3.1.	Male <i>db/db</i> mice present with reduced LSEC fenestrations and porosity.....	61
5.3.2.	Blocking SEMA3A binding to NRP1 in <i>db/db</i> mice slightly affects hepatic steatosis	64
5.3.3.	Endothelial cell-specific deletion of <i>Sema3a</i> reduces hepatic steatosis and affects LSEC fenestrae.....	65
6.	Discussion	69
6.1.	LSEC and fenestrae: establishment of quality and analysis	70
6.1.1.	MACS isolation yields viable LSECs with satisfactory purity	70
6.1.2.	The deep learning workflow identifies and analyses fenestrae with a high accuracy	70
6.1.3.	MACS-isolated LSECs retain their size and do not lose fenestrae during short-termed experiments.....	72
6.2.	SEMA3A and fenestrae: mechanism of action.....	73
6.2.1.	LSEC porosity and fenestrae frequency negatively correlate with SEMA3A concentrations.....	73
6.2.2.	NRP1 is required for SEMA3A-induced defenestration in mouse LSECs.....	74
6.2.3.	Several kinases involved in actin-dynamics are activated by SEMA3A in mouse LSECs ...	75
6.2.4.	LIMK1 and cofilin-1 phosphorylation are required for SEMA3A-induced defenestration	77
6.2.5.	Palmitic acid and SEMA3A affect actin-dynamics by increasing the F-/G-actin ratio	78
6.3.	The role of <i>Sema3a</i> in the development of MASLD.....	79
6.3.1.	Male <i>db/db</i> mice are a suitable model for capillarization in early stages of MASLD.....	79
6.3.2.	Blocking SEMA3A binding to NRP1 in <i>db/db</i> mice might have a therapeutical value in the context of MASLD	80
6.3.3.	Long-term genetic interference of SEMA3A signalling improves VLDL secretion and hepatic steatosis	82

7.	Conclusion and Outlook	85
8.	List of Abbreviations	89
9.	Supplementary Data	98
9.1.	F-/G-actin western blot of human LSECs treated with palmitic acid	98
9.2.	F-/G-actin western blot of mouse LSECs treated with SEMA3A-Fc.....	98
9.3.	Western blots of mouse LSECs treated with IgG2a-Fc, SEMA3A-Fc, and LIMK i3	99
9.4.	Raw SEM images.....	100
9.5.	Deep learning workflow – post-analysis script	101
9.6.	<i>Sema3a</i> expression in <i>db/db</i> mice.....	102
9.7.	Organ weights of male <i>db/db</i> mice treated with NRP1 ^{SEMA3A}	103
9.8.	Relative organ weights of male <i>db/db</i> mice treated with NRP1 ^{SEMA3A}	104
9.9.	BioRender publication licenses.....	105
9.10.	PamGene – Upstream kinase analysis	109
9.11.	PamGene – Multiple Treatments <i>versus</i> control.....	110
10.	List of Tables and Figures.....	111
11.	References	113
12.	Declaration	132
13.	Acknowledgements.....	133

Annotations to this thesis

Parts of this thesis were adapted from my master thesis “The Role of Sema3A in the defenestration of liver sinusoidal endothelial cells” that was conducted between 2020-2021 at the Institute of metabolic physiology at the Heinrich Heine University.

Parts of this thesis were published in Eberhard and Balkenhol et al. (2024), particularly parts of the “Methods” section and figures including figure legends in the “Results” and “Conclusion and Outlook” section.

Author contributions adapted from the manuscript Eberhard and Balkenhol et al. (2024): D.E and S.B. designed, performed, analyzed and interpreted the experiments. D.E. performed mouse work, HFD experiments, analyses of mouse tissues, including immunostaining, ORO staining, perfusion of livers and quantification of sinusoids by SEM. S.B. isolated mouse LSECs and performed treatments with SEMA3A-Fc, anti-NRP1 antibodies, LIMK1 inhibitors, including SEM analyses and quantification, western blot analysis and F-actin/G-actin quantification and performed SEM analysis of *db/db* mice. A.K. B.F.-B. and C.U. established LSEC isolation by FACS, isolated LSECs from obese mice and provided cDNA. I.C. established cofilin-1 western blotting with MACS-isolated mouse LSECs. E.U. and T.D. guided S.B. through the deep-learning workflow. P.F. assisted S.B. with *db/db* mouse and human LSEC experiments. D.E. performed controls of data integrity and analyses. E.L. supervised and scientifically guided D.E. and S.B. through the study. D.E. and E.L. wrote the paper with help from S.B. All authors read and revised the paper.

S.B. contributed experimentally about 50% to the manuscript.

1. Summary

Metabolic dysfunction-associated steatotic liver disease (MASLD) is a metabolic disorder that affects more than 30% of the general population worldwide and has a steadily increasing prevalence. It is characterized by the build-up of fat in the liver and can lead to inflammation, cirrhosis, and finally hepatocellular carcinoma. The loss of fenestrae in liver sinusoidal endothelial cells (LSECs) is an event occurring in early stages of MASLD, preceding inflammation. LSECs line the smallest hepatic blood vessels and are characterized by small pores called fenestrae, which are suggested to allow the bi-directional exchange of lipoproteins between hepatocytes and blood.

Here we present the secreted protein semaphorin-3A (SEMA3A) as part of a mechanism regulating LSEC fenestrae, and thus as a potential contributor to early development of MASLD. *In vitro* we showed that culture dependent loss of fenestrations, cell contraction, and energy depletion do not impair fenestrae analysis in our short-termed experiments. Further, we developed a deep learning workflow which allows us to count and measure fenestrae in a quick and unbiased manner. Regarding the mechanism of action, we identified neuropilin-1 (NRP1) as the main receptor of SEMA3A in LSECs, and, by using kinase activity profiling, found two activators of LIM domain kinase 1 (LIMK1), a kinase which phosphorylates and thus inactivates cofilin-1. Further, we found that phosphorylation of cofilin-1 via LIMK1 is crucial for SEMA3A-induced defenestration in LSECs. Treatment of LSECs with palmitic acid showed visible effects on the F-actin cytoskeleton and induced *SEMA3A* transcription, while SEMA3A itself was able to increase the F-/G-actin ratio in LSECs. *In vivo* we were able to demonstrate the suitability of male *db/db* mice, i.e. obese and diabetic mice, as a viable model for defenestration in the setting of early hepatic steatosis. Lastly, short-term inhibition of SEMA3A-binding to NRP1 in *db/db* mice only slightly affected hepatic steatosis, while long-term genetic intervention via inducible endothelial cell-specific deletion of *Sema3a* in diet-induced obesity (DIO)-mice resulted in reduced macrovesicular steatosis, increased very low-density lipoprotein (VLDL) secretion and tendentially increased fenestrae frequency.

In summary, our data show how saturated fatty acids and DIO induce changes in the LSEC phenotype via SEMA3A by manipulation of the F-actin cytoskeleton, while a knock-out of *Sema3a* in the endothelium results in decreased hepatic lipid accumulation and increased fenestrae numbers. Thus, SEMA3A represents a potential therapeutic target for the treatment and prevention of MASLD.

2. Zusammenfassung

Die Metabolische Dysfunktions-assoziierte steatotische Lebererkrankung (MASLD) ist eine Stoffwechselstörung, die weltweit über 30% der Allgemeinbevölkerung betrifft und deren Prävalenz stetig zunimmt. Sie ist durch eine Ansammlung von Fett in der Leber gekennzeichnet und kann zu Entzündungen, Zirrhose und letztendlich zum Leberzellkarzinom führen. Ein frühes, jedoch kontrovers diskutiertes Ereignis bei mehreren Lebererkrankungen, einschließlich MASLD, ist der Verlust von Fenestrae in den Lebersinusoid Endothelzellen (LSECs). LSECs kleiden die kleinsten Blutgefäße der Leber aus und sind durch kleine Poren gekennzeichnet, die Fenestrae genannt werden und vermutlich den bidirektionalen Austausch von Lipoproteinen zwischen Hepatozyten und Blut ermöglichen, wodurch sie potenziell zum hepatischen Fettstoffwechsel beitragen.

Hier stellen wir das sekretierte Protein Semaphorin-3A (SEMA3A) als Teil eines Mechanismus vor, der LSEC-Fenestrierung reguliert und damit möglicherweise zur Entwicklung von MASLD beiträgt. *In vitro* zeigten wir, dass innerhalb einer kurzen Kultivierung der LSECs weder der kulturabhängige Verlust von Fenestrae noch Zellkontraktion oder Energieverlust die Analyse der Fenestrae beeinträchtigt. Außerdem haben wir einen Deep-Learning-Workflow entwickelt, der es uns ermöglicht Fenestrae schnell und unvoreingenommen zu zählen und zu messen. Bezüglich des Wirkmechanismus haben wir Neuropilin-1 (NRP1) als den Hauptrezeptor von SEMA3A in LSECs identifiziert und durch Kinase-Aktivitätsprofilung zwei Aktivatoren von LIM domain kinase 1 (LIMK1) gefunden, einer Kinase, die Cofilin-1 phosphoryliert und somit inaktiviert. Darüber hinaus fanden wir heraus, dass die Phosphorylierung von Cofilin-1 durch LIMK1 entscheidend für die SEMA3A-induzierte Defenestrierung in LSECs ist. Die Behandlung von LSECs mit Palmitinsäure zeigte sichtbare Effekte auf das F-Actin-Zytoskelett und induzierte die Transkription von *SEMA3A*, während SEMA3A in der Lage war, das F-/G-Actin-Verhältnis in LSECs zu erhöhen. *In vivo* konnten wir zeigen, dass männliche *db/db*-Mäuse, also diabetische und übergewichtige Mäuse, ein geeignetes Modell für die Defenestrierung im Rahmen einer frühen Lebersteatose sind. Weiterhin wirkte sich die kurzfristige Hemmung der Bindung von SEMA3A an NRP1 bei *db/db*-Mäusen nur geringfügig auf die hepatische Steatose aus, während eine langfristige genetische Intervention durch induzierbare endothelzellspezifische Deletion von *Sema3a* bei Mäusen mit einer Diät-induzierten

Adipositas (DIA) zu einer Verringerung der makrovesikulären Steatose und des Körpergewichts sowie zu einer deutlichen Zunahme der VLDL-Sekretion und einem tendenziellen Anstieg der Fenestrae-Häufigkeit führte.

Zusammenfassend zeigen unsere Daten, dass gesättigte Fettsäuren und DIA über SEMA3A durch Manipulation des F-Aktin-Zytoskeletts Veränderungen des LSEC-Phänotyps induzieren, während ein Knock-out von *Sema3a* im Endothel zu einer verringerten hepatischen Lipidakkumulation und einer erhöhten Anzahl von Fenestrae führt. Daher ist SEMA3A ein potenzielles therapeutisches Ziel für die Behandlung und Prävention von MASLD.

3. Introduction

3.1. Liver

The human liver is located in the upper right abdomen and has several vital functions such as protein and lipid metabolism, clearance of blood-borne waste, and the storage of glycogen¹⁻³. Blood is supplied by the portal vein, which supplies approximately 75% of the hepatic blood flow and provides nutrient-rich and oxygen-poor blood, and the hepatic artery, which supplies approximately 25% of the hepatic blood flow, providing oxygen-rich and nutrient-poor blood⁴. During organogenesis the liver is derived from the anterior part of the definitive endoderm and the septum transversum, though it has also been suggested that the pro-epicardial mesenchyme is required for normal hepatic development^{5,6}. Further, the liver has a remarkable regenerative capacity⁷.

Macroscopically, the liver is divided into lobes, while microscopically, it is organized into hepatic lobules, which are the structural and functional units of the liver⁸. The lobules consist of hepatocytes, a central vein, lymphatic vessels, and the portal triad, which itself is comprised of the hepatic artery, the portal vein, and a bile duct⁸. With six portal triads around the central vein, the lobules are given a hexagonal shape (**Figure 1**), whereas a triangular subunit of the hexagon is called acinus⁸. Due to this structural organisation, different oxygenation zones within the acini exist^{9,10}. Zone one, being closest to the portal triad, receives the most oxygenated blood, while zone three, being closest to the central vein, receives the least oxygenated blood⁹. Depending on the zone, hepatocytes are specialized differently; in zone one hepatocytes perform tasks such as gluconeogenesis and β -oxidation, while in zone three glycolysis and lipogenesis take place^{9,11,12}.

The four main cell types of the livers are the hepatocytes, liver sinusoidal endothelial cells (LSECs), Kupffer cells (KC), and hepatic stellate cells (HSC) (**Figure 2**)⁵. Hepatocytes are the parenchymal cells of the liver and responsible for detoxification, immune cell activation, protein synthesis, glycogen storage and gluconeogenesis, and the lipid metabolism^{1,13,14}. Additionally, they secrete bile into the bile canaliculi, small tubular structures between adjoining hepatocytes, which eventually transport the bile to larger bile ducts and the gallbladder (**Figure 2**)¹⁵. There, the bile is stored and concentrated, and, when triggered by the ingestion of food, released through the common bile duct into the duodenum^{16,17}. The

primary task of bile is to ease the digestion of lipids by aiding the dispersion of large lipid droplets into smaller micelles, ultimately increasing lipid absorption¹⁶. Furthermore, bile is the main excretion route for bilirubin, which is a degradation product of hemoglobin^{16,18}.

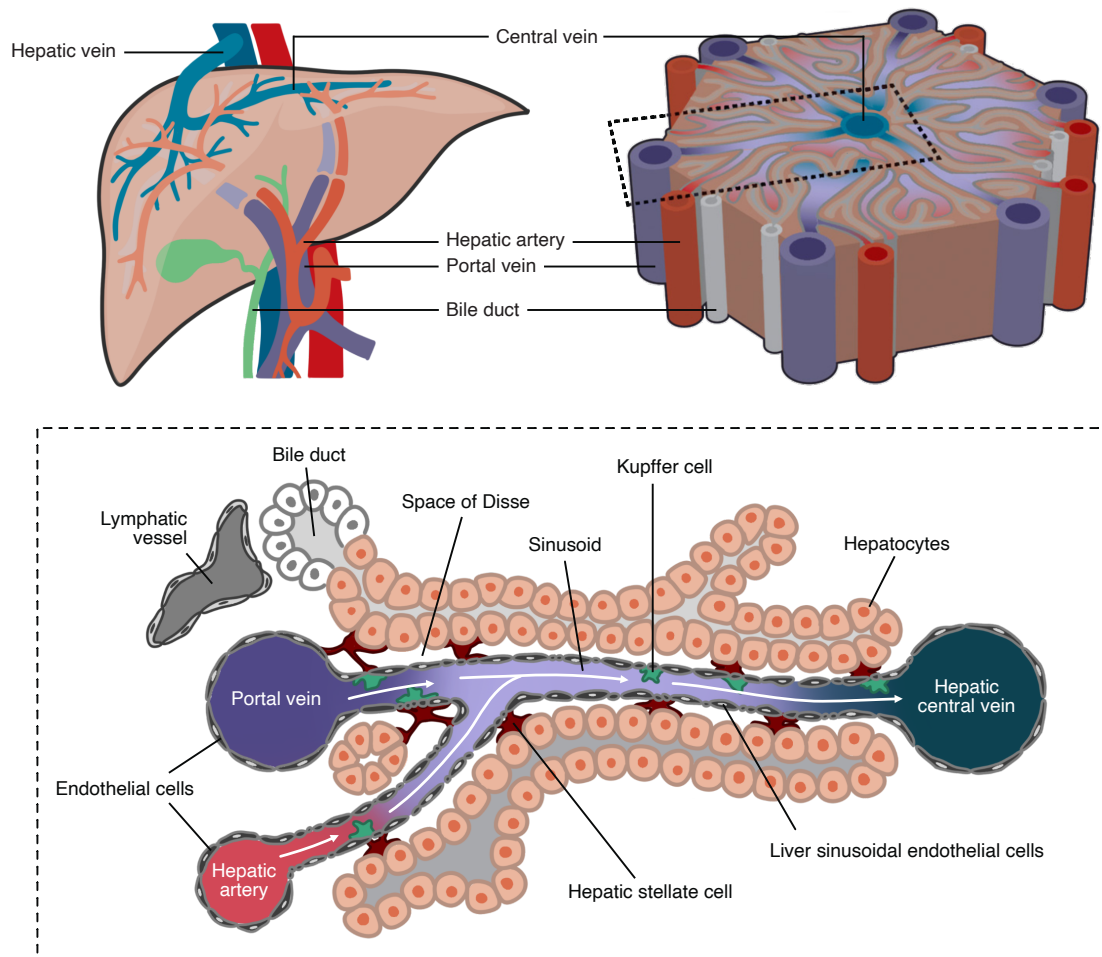


Figure 1. Liver architecture.

Here, the liver with its blood supply (upper left) and the hepatic lobules (upper right) in their hexagonal arrangement are shown. The dashed outline shows where, within the hexagon, the hepatic lobule shown in further detail (bottom) is located. Together, the bile duct, portal vein, and hepatic artery comprise the portal triad. The direction of the blood flow is indicated by the white arrows. Illustrated by Sydney Balkenhol, modified from Ficht et al.¹⁹

LSECs line the smallest blood vessels of the liver, the sinusoids²⁰. LSECs will be described in further detail in the chapter [Liver sinusoidal endothelial cells](#). KCs, also known as Kupfer-Browicz cells, are tissue-resident macrophages in the liver, located within the lumen of the liver sinusoids and can be attached to LSECs²¹⁻²³. As KCs are part of the innate immune response, their main task is to remove debris and bacteria from the bloodstream as well as apoptotic cells^{22,23}. In response to infection and/or inflammation, KCs produce large amounts of inflammatory cytokines, oxygen radicals, and tumour necrosis factor alpha

(TNF- α)^{21,22}. Other than monocyte-derived macrophages, KCs have a certain regenerative capacity, which allows the KC population in the liver to be held constant²⁴.

HSCs are pericytes which have long protrusions wrapping around the sinusoids^{25,26}. HSCs are localized in-between LSECs and hepatocytes, called space of Disse (Figure 2), named after the German anatomist Joseph Disse²⁷. Under healthy, physiological conditions HSCs are in a quiescent stage in which they primarily store vitamin A^{28,29}. Alternative roles during quiescence have not yet been indubitably proven, but some research attributes HSCs an antigen-presenting role²⁸. Further, HSCs are reactive towards endothelial-derived endothelin-1 (ET-1) and nitric oxide (NO) which can result in either contraction or relaxation³⁰. As a consequence HSCs can constrict and regulate the capillary blood flow to a certain extent³⁰. Upon liver injury, regardless of the trigger being infection, drugs, or liver diseases, HSCs convert into their active form, i.e. smooth muscle actin-expressing contractile myofibroblasts^{26,31}. In their active state HSCs release vast amounts of extracellular matrix (ECM) proteins such as collagen type 1, and can contract more strongly²⁶. If this state is permanent, the deposition of collagen scar tissue, i.e. fibrosis, can result in cirrhosis³².

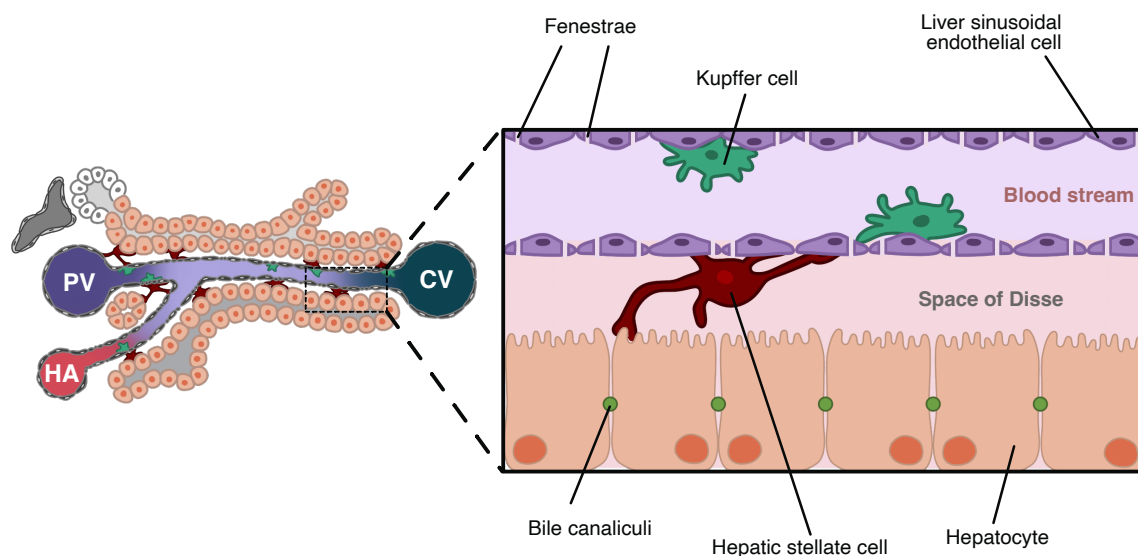


Figure 2. Liver cell types.

Here, the four main cell types of the liver and their location within the hepatic lobules (left) are shown schematically. From the hepatic artery (HA) and portal vein (PV), blood flows towards the central vein (CV) via the sinusoids. The sinusoids are lined by the liver sinusoidal endothelial cells which have fenestrae that allow a bi-directional exchange of molecules between the blood flow and the hepatocytes. Inbetween liver sinusoidal endothelial cells and hepatocytes, i.e. the space of Disse, hepatic stellate cells are located. Situated in the lumen of the liver sinusoids are Kupffer cells. Between the hepatocytes are the bile canaliculi, which collect the bile produced by hepatocytes and channels it into larger bile ducts. Illustrated by Sydney Balkenhol, inspired by Ficht et al.¹⁹

As previously mentioned, the liver has a remarkable regenerative capacity^{7,33}. It is the only visceral organ that, upon removal of up to 70% of its volume, can fully regenerate in a relatively short time span³⁴. This is due to hepatocytes having a nearly unlimited regenerative capability which has been shown by several liver recolonization models⁷. During regeneration, certain growth factors have been shown to play a major role such as hepatic growth factor (HGF), epidermal growth factor receptor (EGFR), and most recently, myeloid-derived growth factor (MYDGF)^{35,36}.

In summary, the liver is a multi-functional organ, which is important for several physiological functions and harbours an extraordinary regenerative capacity.

3.1.1. Mouse *versus* human liver

The liver to body weight ratio scales proportionally in mammals and is therefore the same in mice as in humans³⁷. Structurally, in humans the liver lobes are divided into the left, right, quadrate, and caudate lobe, while in mice the lobes are divided into the left, right, median, and caudate lobe³⁸⁻⁴⁰. Both human and mice have a gallbladder, while rats, which belong to the same subfamily (*murinae*) as mice, do not have one⁴¹.

Functionally, the livers in mice and humans are fundamentally congruent, however, there are major differences regarding liver disease progression⁴². Even though mice are the most commonly used animal model for liver diseases, which is due to their availability and cost-efficiency, there are major differences regarding gene regulation in the liver, susceptibility towards certain diseases as well as disease progression⁴³. In one study a hepatitis B drug candidate resulted in the death of five individuals during a clinical trial, while mice, dogs and monkeys were not susceptible towards the hepatotoxic effect of the drug⁴⁴. Further, a comparative transcriptomics analysis of mouse and human livers revealed that many genes and biological pathways exhibit species-specific regulation in the setting of hepatic steatosis⁴⁴. To be able to translate therapeutical studies with mice to humans, it is crucial to be aware of the differences and similarities between mice and humans, and any studies should be interpreted with great care^{42,43}.

In summary, while the mouse and human liver share most functional and structural aspects, they differentiate considerably regarding their gene regulation and during liver disease progression.

3.1.2. Lipid metabolism

Upon the ingestion of food, lipid droplets are dispersed by bile into micelles, which are broken down further into monoglycerides and fatty acids by the pancreatic lipase⁴⁵. Monoglycerides and fatty acids are then absorbed by enterocytes in the small intestine, recombined into triglycerides (TGs), and transported with cholesterol in the form of chylomicrons or chylomicron remnants to the adipose tissue and the hepatocytes via the bloodstream⁴⁶. During transportation, and in proximity to adipose and muscle tissue, lipoprotein lipase (LPL) hydrolyses TGs into free fatty acids which can then be absorbed by muscle cells and adipocytes⁴⁷. This process results in the conversion of chylomicrons into chylomicron remnants, which are small enough to pass through fenestrae in the liver⁴⁸. The subsequent uptake of fatty acids is facilitated by fatty acid transport proteins (FATP) and cluster of differentiation 36 (CD36)⁴⁹. CD36 specifically assists with the uptake of long-chain fatty acids and is regulated by peroxisome proliferator-activator receptor gamma (PPAR γ), a receptor functioning as a transcription factor, regulating fatty acid storage and glucose metabolism^{50,51}. Due to their hydrophobic nature, fatty acids cannot move freely in the cytosol but need to be transported by fatty acid binding proteins (FABP)⁵². FABP1, which is the prevalent isoform in the liver, aids the storage, transportation, and utilization of fatty acids and also affects expression of peroxisome proliferator-activator receptor alpha (PPAR α) which can induce the transcription of fatty acid oxidation-related genes^{53,54}.

In order to be exported again, stored fatty acids are turned into very low-density lipoprotein (VLDL) particles⁵⁵. To this end, TGs and cholesterol esters are relocated to apolipoprotein (Apo) B-100, which is mediated by microsomal triglyceride transfer protein (MTTP) and takes place in the endoplasmic reticulum (ER)^{46,56}. Depending on the number of TGs present, the resulting VLDL particle varies considerably in size¹. Upon reaching full maturity after passing through the Golgi apparatus, the VLDL particle is secreted back into the bloodstream⁵⁷.

If stored fatty acids are oxidized, they are transported to the mitochondria, peroxisomes, or the ER where either β - or ω -oxidation takes place¹. Both are the process of breaking down fatty acids into acetyl-CoA, however, β -oxidation takes place in the mitochondria and the peroxisome while ω -oxidation takes place in the ER^{1,58}. PPAR α can induce expression of genes needed for fatty acid oxidation (FAO) such as pyruvate dehydrogenase kinase 4

(*PDK4*), acyl-CoA oxidase 1 (*ACOX1*), and carnitine palmitoyltransferase 1 (*CPT1*), resulting in ATP generation but also large amounts of reactive oxygen species (ROS), which can induce oxidative stress^{59,60}. FAO usually occurs upon long periods of fasting and is necessary for the process of ketogenesis⁶¹.

De novo lipogenesis on the other hand can be triggered by hyperinsulinemia and/or a diet rich in carbohydrates and low in fat^{62,63}. Here, fatty acids are synthesized from acetyl-CoA subunits and undergo a series of elongation and esterification steps until they are either stored or secreted as VLDL particles¹. Those processes are regulated by two main transcription factors: carbohydrate regulatory element-binding protein (ChREBP) and sterol regulatory element-binding protein (SREBP) 1c⁶⁴. As the name suggests, ChREBP is activated by carbohydrates, while SREBP1c is activated downstream of the insulin pathway^{64,65}. Increased *de novo* lipogenesis has been found to occur in the setting of obesity and MASLD^{1,66}.

Taken together, the liver is the major site for the lipid metabolism, with lipid import and *de novo* lipogenesis increasing hepatic TG levels, and VLDL export and β -/ ω -oxidation decreasing hepatic TG levels.

3.2. Liver sinusoidal endothelial cells

LSECs are specialized endothelial cells which line the liver sinusoids²⁰. They have several functions including regulation of the blood flow, scavenging of blood borne waste, and ensuring HSC quiescence⁶⁷. LSECs make up only 3% of the liver volume, yet they account for 15-20% of the total liver cell population⁶⁸. LSECs can release different vasodilating agents, such as NO, upon shear stress through activation of endothelial nitric oxide synthase (eNOS), and the transcription factor Kruppel-like factor 2 (KLF2)⁶⁷. KLF2 reduces vasoconstrictive agents such as ET-1, which, just like NO, can exert an effect on HSC, keeping them in a non-vasoconstrictive, quiescent state⁶⁷. As long as LSECs are differentiated, they prevent HSC activation, a point which is further described in LSECs in diseases⁶⁹.

On their surface, LSECs express several endocytosis and scavenger receptors, such as stabilin-1 and -2, which both allow for extremely rapid internalization of waste molecules, making them part of the reticuloendothelial system and innate immune response^{70,71}. LSECs

are also able to perform clathrin-mediated endocytosis, allowing them to clear macromolecular waste from the blood⁷².

Another noteworthy feature of LSECs is that they do not have a basal lamina which allows direct access of solutes into the space of Disse⁷⁰. This feature, however, is lost during dedifferentiation, e.g. during liver disease or aging, where a basal lamina is generated⁷⁰. The most distinctive characteristic of LSECs are the fenestrae, small pores which are suggested to allow the bi-directional exchange of metabolites, lipids, and other solutes^{73,74}. They are, depending on the species, between 50-200 nm in diameter, and highly dynamic structures^{75,76}. Fenestrae are organized into sieve plates, which usually consist of 10-100 fenestrae^{74,77}.

Under normal conditions, LSECs regenerate either through self-renewal or residential sinusoidal endothelial cell progenitors (RSECP), which make up 1-7% of the LSEC population⁷⁸. Upon acute liver injury, LSECs regenerate from two different cell populations: RSECP and bone-marrow derived LSECs^{1,79}. In the setting of partial hepatectomy, the proliferation and mobilization of bone-marrow derived LSECs doubled, displaying their major contribution to liver regeneration^{67,79}.

In conclusion, fenestrated LSECs are crucial for HSC quiescence and the bi-directional exchange of molecules, and their ability to clear blood borne waste plays an important role in the innate immune response.

3.2.1. Fenestrae

Fenestrae are essential structures for the filtering of blood and the bi-directional exchange of metabolites between the bloodstream and the hepatocytes. In the past decades, fenestrae have also been suggested to be essential for the uptake and secretion of lipids⁸⁰⁻⁸³. Fenestrated endothelial cells are present in the liver, bone marrow, spleen and partially in the brain⁸⁴.

Fenestrae are present in most mammals, but also in fish and birds^{85,86}. Their size varies strongly; rabbits are reported to have the smallest fenestrae on average, with 55-64 nm, while humans and baboons have the largest fenestrae with 50-300 nm and 92-116 nm, respectively⁸⁷.

Several substances and factors, both exogenous and endogenous, are known to have an effect on fenestrae number and size. Alcohol for example, both acute and chronic, increases the diameter of fenestrae, while chronic abuse decreases their number⁸⁷. Nicotine on the other hand decreases both number and diameter, linking chronic smoking with atherosclerosis^{74,87,88}. Fraser et al. showed that the uptake of cholesterol, a relatively large lipid, depends on the size of fenestrae⁸⁸. Therefore, they postulated that nicotine, via reduction of fenestrae diameter, promotes atherosclerosis^{83,88}. Serotonin, adrenalin, and ET-1 also reduce the fenestrae diameter, while acetylcholine, prostaglandin E1, and endotoxin increase the diameter^{87,89}. Further, fasting has also been shown to increase fenestrae diameter⁹⁰. On the other hand, events such as hepatectomy, low temperature (4°C), and hepatic steatosis, have been suggested to decrease fenestrae number⁸⁷.

Essentially, fenestrae are structures of the cytoskeleton, surrounded by a fenestrae-associated cytoskeleton ring, consisting of actin and myosin^{91,92}. Braet and Wisse have conducted several studies investigating how fenestrae are formed. They found the so-called fenestrae-forming centre (FFC) which is a dynamic structure and moves within a sieve plate, entailing the formation of multiple fenestrae^{87,92}. The process of fenestrae formation has been proposed to begin with the clearance of small cytosolic areas and re-organization of the actin cytoskeleton^{87,93}. Subsequently, a circular microridge forms as opposite membranes start to move closer together until membrane fusion occurs and ultimately a fenestra is formed⁹³. In the past years, spectrin, an actin cross-linking scaffold protein, and lipid rafts have emerged as important structures for fenestrae maintenance and location of fenestrae formation^{77,94}. In 2014 it has been suggested that plasmalemma vesicle associated protein (PLVAP) facilitates pore formation since *Plvap*-deficient mice had low sinusoidal porosity, however, in 2019 another research group found no difference between *Plvap*-deficient and wildtype mice, suggesting that further research is needed to classify its role in fenestrae formation^{81,95,96}.

In general, fenestrae are highly dynamic structures, a circumstance that has been extensively investigated by Zapotoczny et al. via atomic force microscopy (AFM)^{76,94,97}. Here they showed that the average life span of fenestrae is 20 minutes, whereas some fenestrae only appear for 2 minutes and others for over an hour⁹⁷. Apparently, some fenestrae can also close and reappear⁹⁷. Moreover, they were able to detect the FFC as described by Wisse et al⁹⁷. Besides AFM and structured illumination microscopy (SIM), the only other methods

to image fenestrae in live cells are stimulated emission depletion (STED) microscopy and *direct* stochastic optical reconstruction microscopy (*d*STORM)^{75,98,99}. Due to their extremely small size, imaging fenestrae *in vivo* is currently impossible⁷⁵.

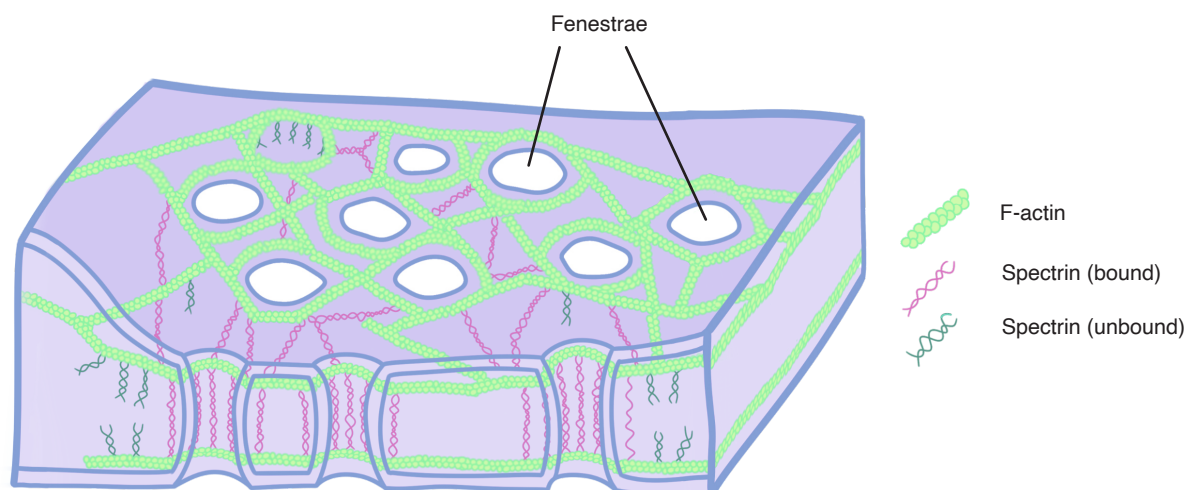


Figure 3. Fenestrae structure in LSECs.

3D cross-section of an LSEC. A ring of filamentous actin (F-actin) is located around each fenestra, and spectrin, bound and unbound, stabilizes them. Illustrated by Sydney Balkenhol, inspired by Szafranska et al.⁹⁵

The exact mechanisms behind fenestrae formation are not fully understood yet, however four main hypotheses, as outlined by Szafranska et al., have been put forward; (de)polymerization of actin regulates fenestrae number, calcium ions regulate fenestrae diameter, fenestrae are located in between lipid drafts, and spectrin is involved in the opening and closing of fenestrae (**Figure 3**)⁹⁵. Fenestrae are known to be affected by several liver diseases and loss of fenestrae has been stated as a definitive pre-cursor of HSC activation^{67,100}. The exact factors behind dedifferentiation of LSECs during diseases remain elusive, but Hammoutene et al. have suggested that excessive dietary macronutrients, including lipids, carbohydrates, and gut microbiota-derived products play a role⁸². Besides different liver diseases, aging is a long-known cause of loss of fenestrae^{101,102}. The smaller size and lower number of fenestrae in older people is presumably an important factor in age-related atherosclerosis and other comorbidities¹⁰³⁻¹⁰⁵.

In summary, fenestrae are dynamic structures of the cytoskeleton, and their size and number can be changed by several factors, however, the precise mechanisms have not yet

been fully elucidated. Additionally, fenestrae are important for the exchange of small molecules between the bloodstream and the hepatocytes.

3.3. Metabolic dysfunction-associated steatotic liver disease

In February 2024 the term non-alcoholic fatty liver disease (NAFLD) was re-termed into metabolic dysfunction-associated steatotic liver disease (MASLD) as this term more proficiently stresses the impact of the often-underlying metabolic disease rather than pointing to the fact that alcohol abuse is not the cause¹⁰⁶⁻¹⁰⁸. Risk factors for MASLD include obesity, type 2 diabetes mellitus (T2D), and the metabolic syndrome^{109,110}. By definition, steatosis is present when the liver consists of more than 5% intrahepatic fat¹¹⁰. When steatosis and inflammation coincide, metabolic dysfunction-associated steatohepatitis (MASH, previously termed non-alcoholic steatohepatitis) sets in, eventually followed by fibrosis, cirrhosis, and hepatocellular carcinoma (HCC)^{111,112}. More than 30% of the world's population suffers from MASLD, however, this number strongly varies depending on the country¹¹³. It has been estimated that the prevalence of MASLD will reach 55.7% in 2040, with the greatest overall and relative increase in China^{114,115}.

Many studies investigated the influence of ethnicity and race on the prevalence and development of MASLD^{116,117}. Based on a report in 2021 the Hispanic population in North America had the highest MASLD prevalence with 37%, followed by the non-Hispanic white population with 29.3%, while the non-Hispanic black population had the lowest prevalence of 24.7%^{106,117}. Additionally, a mutation in patatin-like phospholipase domain-containing protein 3 (PNPLA3), which is associated with a higher risk for MASLD, is more common in the Hispanic population¹¹³. There are also significant differences between the sexes regarding the development of MASLD^{118,119}. Specifically, 22-42% of men are estimated to be affected compared to only 13-24% of premenopausal women¹²⁰. Reasons for the differences are poorly understood, however, female hormones such as estrogens are thought to have a protective effect by regulating lipid metabolism, suppressing inflammation, and promoting hepatocellular regeneration^{120,121}.

In summary, the prevalence of MASLD has been steadily increasing over the past decade. Further, the male, Hispanic population is more affected than the female, non-Hispanic population.

3.3.1. Development of MASLD

Besides obesity, T2D, and the metabolic syndrome being known risk factors (**Figure 4**), there are also people which develop steatosis due to severe undernutrition, common in certain eating disorders and famine-related malnutrition¹²². This has been suggested to be due to an increased expression of genes associated with *de novo* lipogenesis and glucose metabolism abnormalities¹²². Furthermore, there are people who are neither over- nor underweight, who do not suffer from T2D and still develop hepatic steatosis¹²³.

Other than the circumstances of diet and exercise, there are certain genetic factors that can have a significant impact on the severity of MASLD development^{124,125}. The most known is PNPLA3, which is a lipid droplet-associated protein and helps to regulate both lipogenesis and lipolysis¹²⁶. A single nucleotide substitution results in an increased risk for hepatic steatosis, MASH, and fibrosis¹¹⁷. Further, a missense mutation in transmembrane 6 superfamily 2 (TM6SF2), a lipid transporter whose activity is required for VLDL secretion, increases the risk of MASLD by 35% and results in severe hepatic steatosis¹¹⁷. Lastly, an inactivating mutation in membrane-bound O-acyltransferase domain containing 7 (MBOAT7), an enzyme which is important for phospholipid remodelling, is associated with an increased severity of hepatic steatosis¹¹⁷.

Simple steatosis, i.e. benign accumulation of fat in the liver, does not necessarily entail liver damage and usually does not result in discomfort or other symptoms that might be noticed by patients¹²⁷⁻¹²⁹. The best method to determine the presence and grade of steatosis is a biopsy, however, this is a highly invasive procedure and might also yield wrong results as steatosis can often be unevenly distributed^{110,130}. Alternatively, non-invasive methods can be used to determine the presence of hepatic steatosis, whereas MRI-derived proton density fat fraction (MRI-PDFF) is currently the non-invasive method with the highest diagnostic accuracy^{131,132}. Furthermore, several blood serum parameters, such as alanine aminotransferase (ALT) and aspartate aminotransferase (AST), can be measured, however a single factor as an undisputable determinant for MASLD has not yet been found¹³³. The lack of simple, reliable, and non-invasive methods contributes to the fact that most cases of MASLD are detected in advanced stages¹³⁴. An important vascular manifestation of early stages of MASLD is the defenestration, also called capillarization, of LSECs^{67,69,80,82,135,136}.

When steatosis and inflammation coincide, MASH sets in (**Figure 4**)¹³⁷. Upon long-term steatosis, hepatocytes store exceedingly large amounts of lipids and increase in size¹³⁸⁻¹⁴⁰. Over time a phenomenon called hepatocyte ballooning is known to occur, where hepatocytes bulge out and push their nucleus closer to the cell membrane¹⁴¹. At a certain point, hepatocytes can reach their maximum storage capacity and induce apoptosis, an event which releases damage-associated molecular patterns (DAMPs), extracellular vesicles (EVs), and harmful lipids¹⁴². Upon this event, the macrophages of the liver, the KC, are attracted and release copious amounts of inflammatory cytokines^{142,143}. Common cytokines are TNF- α , interleukin 6 (IL-6), the chemokine (C-C motif) ligand 2 (CCL2), as well as the inflammation marker high-sensitivity C-reactive protein (hs-CRP)¹⁴⁴. Those exacerbate hepatocyte damage and promote inflammation¹⁴³. Based on Day and James the progression of hepatic steatosis, the first hit, to MASH requires the involvement of certain factors, such as genetic, epigenetic, and dietary factors, called the second hit, a proposition which has been termed the two-hit hypothesis¹⁴⁵. This hypothesis has been renamed into the multiple-hit hypothesis, which now includes multiple factors acting alongside each other and also includes factors such as insulin resistance, gut microbiota, and hormone secretion from adipose tissue¹⁴⁶. Both hypotheses, however, agree on the fact that certain factors have to coincide in order for simple steatosis to turn into steatohepatitis^{145,146}. With regard to the whole body, inflammation of the liver is associated with a rise in cortisol levels and enlarged periportal lymph nodes^{147,148}.

Upon liver injury caused by steatohepatitis, HSC can be activated by several different factors, such as dedifferentiated, i.e. capillarized, LSECs and/or osteopontin^{80,136}. Osteopontin is a secreted phosphoprotein which is usually found in the bile duct epithelium and known to be a key player in the process of HSC activation¹⁴⁹⁻¹⁵². In the setting of fibrosis, osteopontin acts as a chemoattractant for neutrophils and macrophages in necrotic areas¹⁴⁹. Osteopontin also acts as a cytokine further promoting fibrosis, yet factors regulating osteopontin expression are incompletely understood¹⁴⁹. In the setting of liver injury, osteopontin expression is induced and increased in hepatocytes, KCs and HSCs themselves, resulting in a vicious cycle of HSC activation and further increased osteopontin expression^{149,151}. Additionally, osteopontin directly upregulates collagen-I production by activating high-mobility group box-1 (HMGB1) in HSCs¹⁵¹.

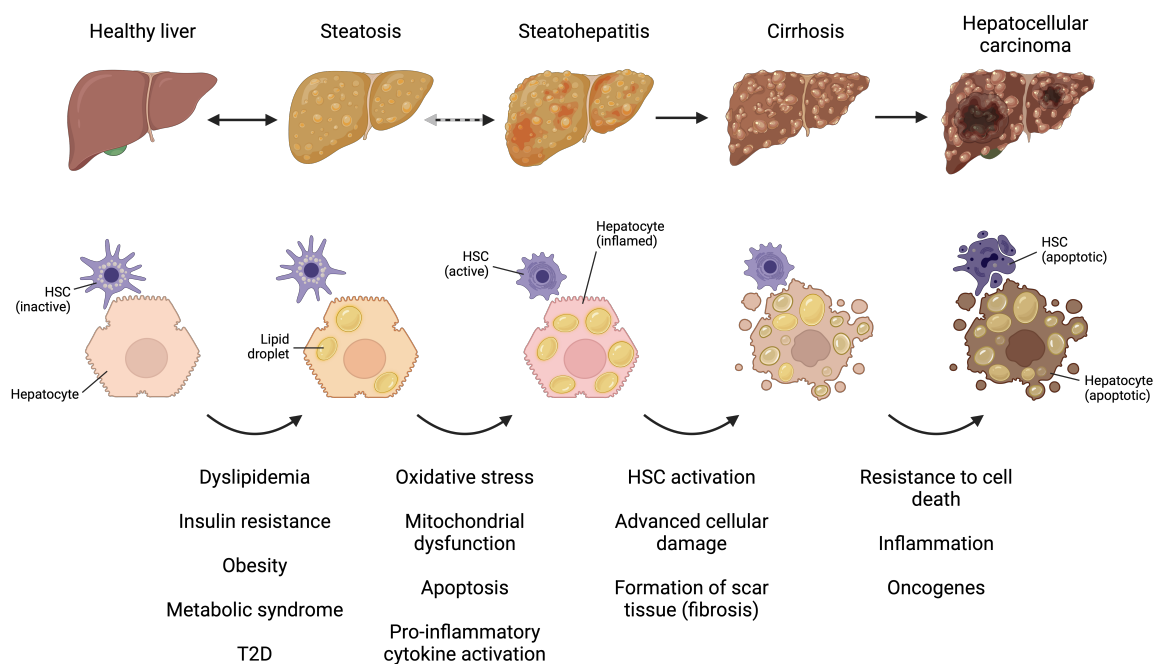


Figure 4. MASLD Progression.

The healthy liver is characterized by inactive HSCs and little to no lipid accumulation. Steatosis can be caused by dyslipidaemia, insulin resistance, obesity, the metabolic syndrome, and is characterized by the formation of lipid droplets. The progression to steatohepatitis can be triggered by oxidative stress, mitochondrial dysfunction, apoptosis, and proinflammatory cytokine activation, and is usually accompanied by HSC activation and macrophage infiltration. Persistent HSC activation, advanced cellular damage, and formation of scar tissue can then result in fibrosis and cirrhosis¹⁵³. With ongoing inflammation, the resistance to cell death in cancer cells, and induction of oncogenes, hepatocellular carcinoma (HCC) can arise¹⁵⁴. Created with BioRender.com.

Short-term activation of HSCs and the subsequent formation of scar tissue may be reversible, and thus might not lead to serious health effects^{155,156}. However, the longer ECM production perseveres, the more scar tissue is produced¹⁵⁷. At a certain point, severe fibrosis is termed cirrhosis, with fibrotic bands, parenchymal nodules, and vascular distortion (**Figure 4**)¹⁵⁸. Cirrhosis poses serious long-term health effects such as portal hypertension, liver cell dysfunction and progression to HCC¹⁵⁹⁻¹⁶¹. There is a large amount of research solely focussed on discovering drugs which halt or even reverse the process of fibrosis, however, to this day no approved anti-fibrotic drug is available in the European market, making liver transplantation the only viable option^{162,163}. Approximately 15% of people in need of a transplant die before matching a donor, and, according to the global observatory on donation and transplantation, transplantation only covers 10% of the global need^{164,165}. While approximately 20% of people progress from MASLD to MASH, 34-42% progress from MASH to fibrosis. Over time, 15% progress from fibrosis to cirrhosis, and from there 2.4-12.8% will develop HCC¹⁶⁶⁻¹⁶⁹. HCC is currently the leading cause for liver transplantation, however, as aforementioned, the demand for liver transplants does not

match the availability^{164,165}. An alternative is the removal of the cancerous tissue; however, only 5-10% of HCC are suitable for removal, and the recurrence rate is 50-60%^{170,171}. HCC has very poor survival predictions, with the average prognosis being nine months in individuals with untreated HCC¹⁷².

In conclusion, MASLD is a multifactorial disease which develops over time, and can result in simple steatosis but also more serious disease manifestations such as cirrhosis and HCC. While simple steatosis is reversible and usually does not pose serious health effects, cirrhosis and HCC cause irreversible damage to the liver and have poor survival predictions.

3.3.2. Treatment/Interventions for MASLD

Several treatment options for MASLD exist, depending on the stage of the disease. First, since approximately 75% of MASLD patients have T2D, there are diabetic, insulin sensitivity increasing, medications^{1,153}. Additionally, since many studies have shown that weight loss can often resolve hepatic steatosis, lifestyle interventions such as a change of diet and exercise are often recommended¹⁷³. Since 2022 the weight loss drug tirzepatide (brand name: Mounjaro) is widely used to induce weight loss via glucagon-like peptide-1 receptor (GLP-1R) and gastric inhibitory polypeptide receptor (GIP-R) agonism¹⁷⁴. As of November 2023, another GLP-1R agonist drug, semaglutide (brand name: Ozempic) has been released and while tirzepatide has stronger weight loss effects, semaglutide has been shown to reduce cardiovascular risks associated with T2D¹⁷⁵⁻¹⁷⁷.

Despite several drugs being currently under investigation regarding specifically targeting hepatic steatosis, none have so far been approved. Since the full mechanics behind steatosis still have to be determined, and MASLD is a multifactorial disease, the development of new drugs is challenging. Still, there are several drugs in stage II and III trials which have promising results. One of them is vitamin E, which has been shown to improve AST and ALT levels, steatosis and to some extent fibrosis, however, more long-term studies are needed to ensure the overall safety of vitamin E supplementation¹⁷⁸. Another promising treatment is obeticholic acid, a farnesoid X receptor agonist, which has been shown to improve liver histology and ALT/AST levels via inhibition of inflammatory signalling and HSC activation¹⁷⁹⁻¹⁸². Further, in a phase III trial, a liver-directed, thyroid hormone receptor β -selective agonist, i.e. resmetirom, was shown to resolve MASH in up to 29.9% of patients while

improving fibrosis by at least one stage in 24.2%¹⁸³. Since its administration also posed serious side effects, more long-term studies are required, however, in March 2024 it has been approved for use in the USA^{183,184}.

In sum, regardless of extensive research, there is still a lack of liver-specific therapies/drugs which halt or even reverse the development of MASLD.

3.3.3. LSECs in diseases

LSECs are part of the innate immunity and mediate the immune response during acute and chronic liver diseases¹⁸⁵. During early stages of MASLD, LSECs have been shown to lose their fenestrae, a process called capillarization, where they also develop a basement membrane¹³⁵. The mechanism behind this process has not yet been elucidated, however, excessive amounts of lipids, carbohydrates, and gut microbiota-derived products are thought to be essential triggers⁸². Several hypotheses exist which explain how capillarization might lead to hepatic steatosis, mostly focusing on the exchange of lipids through fenestrae: VLDL particles might not be able to leave the space of Disse, while chylomicron remnants may not be able to enter it^{1,80,81}. Conversely, as chylomicron remnants are not able to reach the hepatocytes anymore, *de novo* lipogenesis may be activated⁸¹. However, in order to be able to specifically, pharmaceutically target LSEC capillarization, the pathways behind the loss of fenestrae and their mediators need to be further investigated.

At early stages of MASH, LSECs actually have anti-inflammatory properties, however, in more advanced stages they start to exhibit a pro-inflammatory phenotype, where they copiously express intracellular adhesion molecule 1 (ICAM1) and vascular cell adhesion molecule 1 (VCAM1), as well as TNF- α , IL-6, IL-1, and CCL2^{80,186-188}. Those mediators activate neighbouring Kupffer cells and thus further promote progression from MASH to fibrosis¹⁸⁷. Here, the crosstalk between LSECs and HSCs is crucial¹⁸⁹. When LSECs capillarize and/or express pro-inflammatory cytokines, such as vascular adhesion protein 1 (VAP-1), they participate majorly in HSC activation⁸². Upon their activation, HSCs differentiate into myofibroblasts, producing large amounts of extracellular matrix compounds such as collagen, fibronectin, and laminin^{29,190}.

Advanced fibrosis can evolve to cirrhosis over time, a setting in which defenestrated LSECs contribute to portal hypertension¹³⁶. Additionally, circulating endothelial progenitor cells stimulate LSECs with vascular endothelial growth factor (VEGF) and platelet-derived growth factor (PDGF) which can induce migration of HSCs, vessel formation, and production of collagen, ultimately promoting disease progression^{187,191}. Should cirrhosis progress to HCC, the expression of LSEC marker proteins, i.e. stabilin-1, stabilin-2, and lymphatic vessel endothelial hyaluronan receptor 1, starts to decrease^{192,193}. On the other hand, expression of integrins increases, which allows cancer cells to adhere at a greater capacity¹⁹⁴. Further, increased ICAM1 expression, which aids leukocyte adherence, promotes the infiltration of HCC^{136,142,194,195}. Thus, LSEC dysfunction can greatly contribute to HCC progression and growth¹³⁶.

In summary, LSEC dysfunction during each stage of MASLD has a significant impact on disease progression and worsening. This makes LSECs an important target regarding the treatment of MASLD, as their phenotype can decide between a healthy and a diseased liver.

3.4. The semaphorins

3.4.1. Semaphorin protein family

The semaphorin protein family consists of seven different classes, whereas classes 1 and 2 are only found in invertebrates, classes 3-7 in vertebrates, and class V is only present in viruses (**Figure 5**)¹⁹⁶. The first semaphorin to be discovered was semaphorin-1A (SEMA1A), which was originally named Fascilin IV, in the context of growth cone guidance in the grasshopper embryo in 1992¹⁹⁷. While there are many differences among the groups, one thing they all have in common is the sema and the PSI (Plexin, semaphorin, and integrin) domain, the former being highly conserved among species and consisting of a conserved set of cysteine residues, forming multiple disulfide bonds which stabilize the structure^{196,198}. The PSI domain is a cysteine-rich module found in several signalling molecules, including plexins, semaphorins, integrins, and attractins¹⁹⁹. While some semaphorins are secreted, others have transmembrane domains, glycosylphosphatidylinositol (GPI) linkers, or thrombospondin type 1 repeats which act as membrane linkers^{196,200}. Some groups also have a single C2-class immunoglobulin (Ig)-like domain while others have a basic domain, consisting of several highly basic amino acids, which together with the sema domain is

important for receptor binding^{196,201}. Each of the domains and combination thereof are important for their function and receptor binding abilities¹⁹⁶.

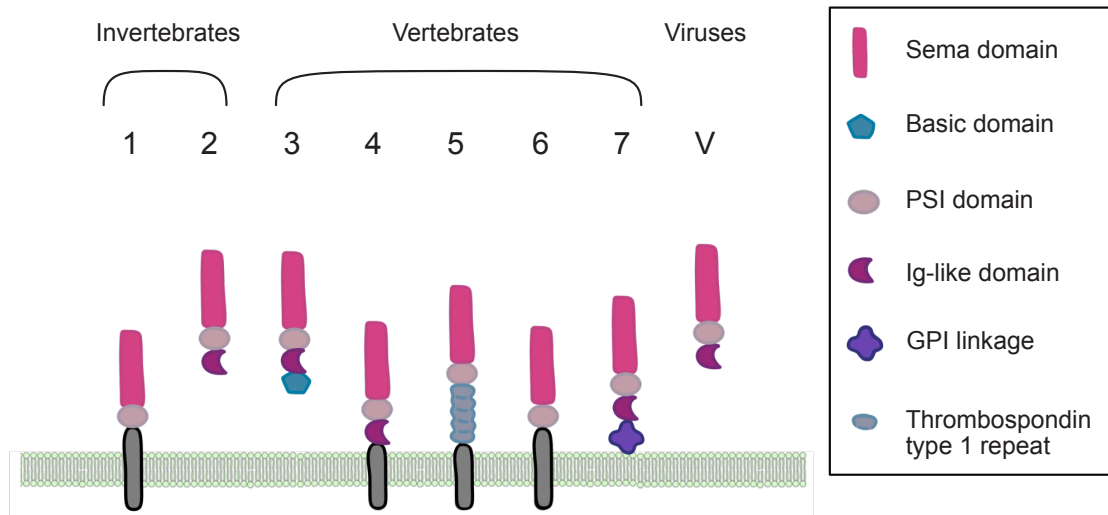


Figure 5. The semaphorin protein family and their structures.

Each class of semaphorins has a sema domain and a PSI domain. Classes 1 and 2 are only found in invertebrates, 3-7 in vertebrates, and V in viruses. While classes 2, 3, and V are secreted, the other classes are either membrane bound or linked. PSI = Plexin, semaphorin and integrin, Ig = Immunoglobulin, GPI = Glycosylphosphatidylinositol. Illustrated by Sydney Balkenhol, inspired by Jiao et al. and Yazdani et al.^{196,202}.

One receptor family which all classes, except class 2, can bind to are the plexins²⁰³. Plexins also have a PSI domain and a sema domain which aids the binding to semaphorins²⁰⁴. While most classes can directly bind to plexins, class 3 semaphorins need a co-receptor, such as a neuropilin-1 (NRP1) or -2 (NRP2), which then recruits a class A or D plexin, forming a holoreceptor complex (**Figure 6**)^{205,206}. In this complex, plexins are the signal transducing unit²⁰⁷. The only exception is SEMA3E, which can exert an effect by binding to plexin-D1 directly as well as through NRP1²⁰⁸. Further, SEMA3A binds to NRP1 and plexin-A1-4, while SEMA3F binds to NRP2 and forms a complex with plexin-A3²⁰⁹. SEMA6D is additionally able to transduce a signal via VEGFR2 and SEMA7A can signal through $\alpha 1\beta 1$ integrin (**Figure 6**)^{196,209}.

In general, semaphorins are multifunctional proteins which have pleiotropic roles in several organs throughout embryogenesis and adulthood^{210,211}. They regulate many processes which range from cell migration, angiogenesis, cell adhesion, apoptosis, and cytoskeleton organization²¹². Their expression is crucial in early development of the nervous system and the heart and changes during maturation^{213,214}. Their expression patterns can also change

in the setting of diseases such as schizophrenia, Alzheimer's, cancer, autoimmune disorders, and neurodegenerative diseases^{215,216}. In those pathologies, semaphorins can act both as suppressors and promoters of the disease, again underlining their diverse functions^{202,215,217}.

To summarize, semaphorins are multifunctional proteins that are expressed in nearly every tissue and their roles and intracellular downstream actions are manifold.

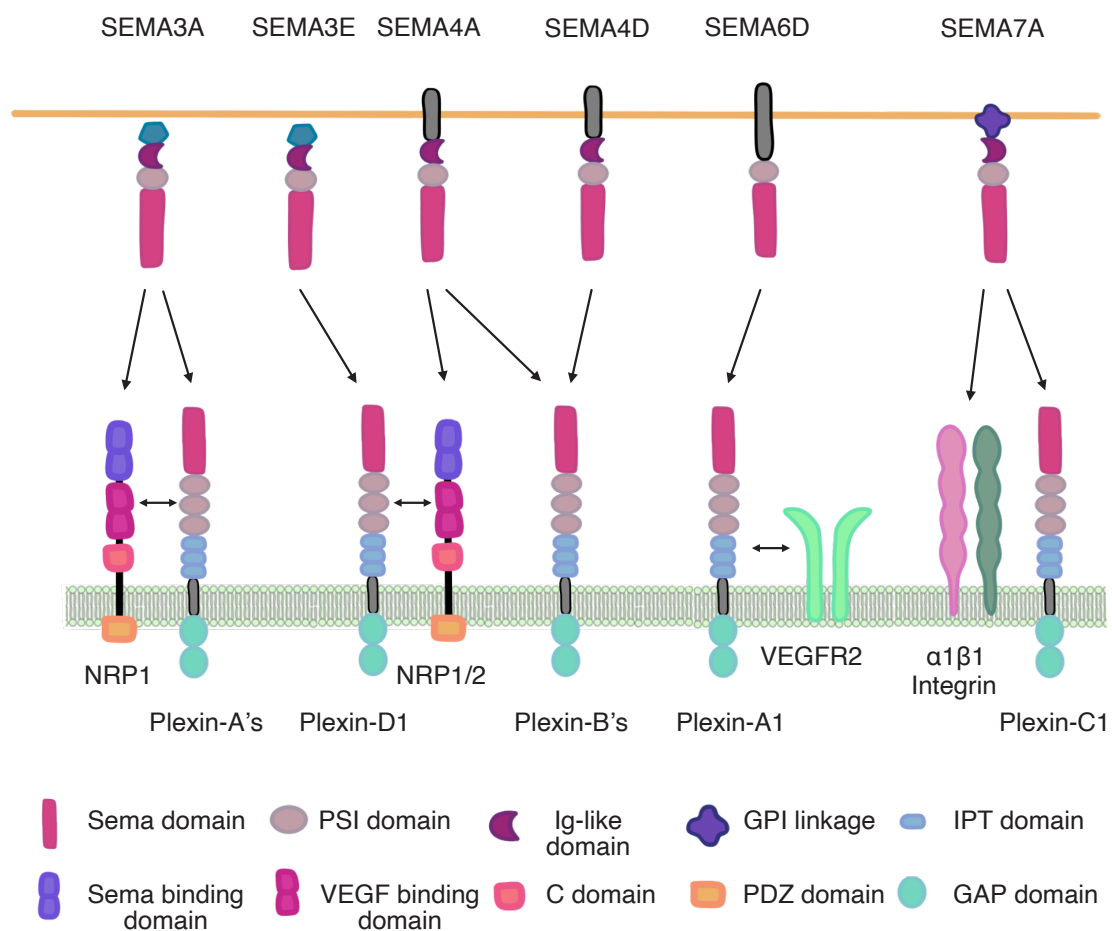


Figure 6. The semaphorins and their receptors.

Here, selected semaphorin-receptor interactions are shown. SEMA3A binds to NRP1 which forms a holoreceptor complex with plexin-A1-4. SEMA3E on the other hand can transduce a signal by directly binding to plexin-D1, while SEMA4A binds to NRP1/2 first. SEMA4A and SEMA4D can also bind to type B plexins. SEMA6D can bind to plexin-A1 which then recruits VEGFR2. SEMA7A can bind to both $\alpha 1\beta 1$ integrin and plexin-C1 to convey a signal. NRP1 = Neuropilin-1, VEGFR2 = Vascular endothelial growth factor receptor 2, PSI = Plexin, semaphorin, and integrin, Ig = Immunoglobulin, GPI = Glycosylphosphatidylinositol, IPT = Ig-like, plexins, transcription factors, VEGF = Vascular endothelial growth factor, PDZ = Post synaptic density protein (PSD95), drosophila disc large tumor suppressor (Dlg1), and zonula occludens-1 protein (zo-1), GAP = GTPase-activating proteins. Illustrated by Sydney Balkenhol, modified from Zhou et al.²⁰⁹.

3.4.2. Semaphorin-3A

SEMA3A was first discovered in 1993 in the context of neuronal growth cone collapse in the brain of chickens, where it was initially named collapsin²¹⁸. It is a class 3 semaphorin, thus a secreted signalling molecule, and consists of a C2-class immunoglobulin-like and a basic domain next to the PSI and sema domain^{196,219}. Even though its role was first described in the nervous system, it is expressed in endothelial and epithelial cells and almost every type of tissue such as gut, heart, kidney, neurons, teeth, adipose tissue, bone, and even the umbilical cord¹⁹⁶. Depending on the tissue and stage of development, SEMA3A's functions range from bone formation, growth cone collapse, vasculogenesis, to cell death, proliferation, adhesion, aggregation, and migration, as well as cytoskeletal organization¹⁹⁶. As previously mentioned, SEMA3A binds to the receptor NRP1 which then forms a holoreceptor complex with a type A plexin, in which plexin conveys the intracellular signal²⁰⁰. The probably most investigated role of SEMA3A is its function in neuronal development²²⁰. Here, SEMA3A results in the collapse of growth cones via LIM domain kinase 1 (LIMK1) and cofilin-1, resulting in cytoskeletal reorganization²²¹. Besides the nervous system, SEMA3A has also important functions in the bone, where it promotes osteoblastic bone formation and inhibits adipocyte differentiation, having an osteoprotective effect²²².

Since NRP1 is also a receptor for VEGF-A there has been a lot of controversy regarding the question whether SEMA3A and VEGF-A are opponents or affiliates²²³⁻²²⁵. Although SEMA3A and VEGF-A bind to different sub-domains of NRP1, they do not directly compete, however, SEMA3A might sterically prevent the binding of VEGF-A and *vice versa*^{223,226}. Additionally, while SEMA3A recruits plexin as a co-receptor, VEGF-A recruits VEGFR2²²⁵. The recruiting of different co-receptors results in different, yet not necessarily opposing downstream actions²²⁵. Bachelder et al. showed that SEMA3A and VEGF-A are rather co-operators than competitors regarding chemotaxis of carcinoma cells and that their ratio is more important than their concentrations regarding their chemotactic rate²²⁷.

To conclude, SEMA3A has numerous functions and plays an important role from embryogenesis through adulthood. While the essential receptors are known, many components of SEMA3A downstream signalling have not yet been discovered.

3.4.3. Semaphorin-3A in diseases

SEMA3A is known to play a pathogenic role in several diseases, such as diabetic nephropathy and retinopathy, different types of cancer, and renal fibrosis²²⁸⁻²³¹.

During diabetic nephropathy, which is the chronic loss of kidney and specifically podocyte function during T2D, SEMA3A is increased in podocytes, and inhibition of SEMA3A binding via *Plxna1* deletion in podocytes has been shown to ameliorate albuminuria and improve renal insufficiency²³⁰. Further, direct inhibition of SEMA3A with vinaxanthone, a fungal peptide, resulted in podocyte recovery²³². In renal fibrosis, SEMA3A is increased in the proximal tubulus and inhibition of SEMA3A with vinaxanthone also resulted in amelioration of several disease-associated events²²⁸. Similarly, upon diabetic retinopathy, which constitutes deterioration of the blood-retinal barrier, SEMA3A is induced in the neuronal retina and precipitates breakdown of endothelial barrier function, whereas neutralization of SEMA3A ameliorated vascular leakage²³¹.

Findings regarding the role of SEMA3A in cancer are antagonistic, as SEMA3A shows both promoting and inhibitory effects on cancer cell migration^{233,234}. In breast, prostate, and lung cancer for example, *SEMA3A* expression was found to positively correlate with survival as it inhibits tumour growth and metastasis, whereas in colon and pancreatic cancer it promotes tumour invasion²³³. Regarding breast cancer however, there is also evidence that SEMA3A can both inhibit and promote cancer cell migration via different pathways²³⁵. Recently, Andryszak et al. found positive expression of *SEMA3A* in tumour vessels in 91 out of 98 cases, pointing to a more pathological role in tumour progression²³⁶.

In neurons, SEMA3A acts as a factor which triggers the collapse of growth cones, a fact which reflects negatively on nerve damage, as it prevents axons from rewiring upon injury²³⁷. Zhang et al., however, have shown that inhibition of SEMA3A during spinal cord injury, with direct application of the inhibitor to the site of injury, enhanced axon regeneration and motor function recovery^{238,239}. Further, in the context of ischemia-induced brain damage, a conditional knock-out of *Sema3a* protected the brain from ischemia-induced damage caused by elevated vascular permeability²⁴⁰.

In the liver of rats, *Sema3a* has been shown to be downregulated upon partial hepatectomy, whereas treatment with recombinant SEMA3A attenuated LSEC migration and induced LSEC apoptosis²⁴¹. Further, SEMA3A serum concentrations were found to be significantly

upregulated in MASLD, however, they decreased again at the stage fibrosis²⁴². Conversely, in the setting of HCC, *SEMA3A* has been shown to be overexpressed in humans and upregulation of *SEMA3A* expression in mice promoted HCC progression²⁴³. *SEMA3A* signalling may also indirectly affect the lipid metabolism, via its role in lymphatic valve and vessel formation²⁴⁴. Lymphatic valves play a major role in the absorption of dietary lipids and *SEMA3A* binding to NRP1 is necessary for lymphatic valve and vessel maturation²⁴⁴⁻²⁴⁶. In summary, *Sema3a*/*SEMA3A* is upregulated or secreted to a higher extent in several diseases, and inhibiting *SEMA3A* has been shown to be beneficial towards recovery. However, in some types of cancer, increased *SEMA3A* expression has been shown to inhibit tumour growth. Thus, inhibiting *SEMA3A* can have both disease promoting and inhibiting effects, highlighting the importance of research regarding tissue-specific *SEMA3A* inhibition.

3.5. Aim of this Thesis

SEMA3A is an unknown player in LSEC defenestration and MASLD, however, previous studies from our group suggest it plays a substantial role regarding disease progression. SEMA3A first came to our attention during the screening of differential mRNA expression in the livers of steatotic high-fat diet (HFD)-fed mice and LSECs of *db/db* mice where *Sema3a* expression was significantly increased²⁴⁷. Further research showed that LSECs express all the obligatory SEMA3A receptors, i.e. *Nrp1* and *Plxna1-4*, thus we concluded that SEMA3A can exert an effect on LSECs and is upregulated in the setting of hepatic steatosis. Further, heterozygous *Sema3a* knock-out mice exhibited less hepatic steatosis and more fenestrae²⁴⁷.

First, we will test the quality of MACS-isolated LSECs, the effect of SEMA3A-Fc on LSEC size and viability, and the effect of cell culture on fenestrations over time. In order to analyse fenestrae more efficiently with scanning electron microscopy, we aim to develop a deep learning workflow. Further, to evaluate the effect of SEMA3A-Fc on mouse LSECs *in vitro*, LSECs will be treated with different concentrations of SEMA3A-Fc. To better understand the intracellular mechanisms behind SEMA3A-induced defenestration, we will perform a kinase activity profiling (KAP). Based on the results of the KAP, we are going to perform western blot analysis of cofilin-1 phosphorylation upon SEMA3A-Fc treatment in isolated mouse LSECs. Additionally, we will investigate the effect of NRP1 inhibition, a SEMA3A receptor, and LIMK1 inhibition, the enzyme which catalyses cofilin-1 phosphorylation, regarding SEMA3A-induced defenestration. We also aim to analyse the effect of palmitic acid, a fatty acid that is often increased upon hepatic steatosis, on the expression of *SEMA3A* and F-/G-actin ratio in human LSEC, as well as the effect of SEMA3A on the F-/G-actin ratio in mouse LSECs to examine the effect of SEMA3A on the cytoskeleton.

As *db/db* mice are a well-studied model for T2D and steatosis, we will analyse their fenestrations to investigate their suitability as a mouse model for steatosis-induced defenestration. Lastly, we aim to test the therapeutic value of short-term SEMA3A inhibition in the setting of T2D and hepatic steatosis. Moreover, we are going to employ a genetic model where we perform a tamoxifen-induced, endothelial cell-specific knock-out of *Sema3a* (*iEC^{Sema3a}*) in mice which have diet-induced obesity (DIO) and hepatic steatosis, to evaluate the effect of long-term loss of endothelial cell-derived SEMA3A on fenestrae.

Furthermore, we will investigate the ability of *iEC^{Sema3a}* mice to secrete VLDL and study their fenestrations to examine their ability to export lipids from the liver into the bloodstream. In summary, the ultimate aim of this thesis is to elucidate the role of SEMA3A regarding the process of defenestration in LSECs and characterize the role of SEMA3A-induced defenestration in the development of MASLD.

4. Methods

4.1. Magnetic-activated cell sorting of mouse LSECs

4.1.1. Liver dissociation

To generate a single-cell suspension only consisting of LSECs, the liver dissociation kit (130-105-807) from Miltenyi was utilized. First, the PEB (phosphate-buffered saline (PBS), ethylenediaminetetraacetic acid (EDTA), bovine serum albumin (BSA)) solution was prepared by mixing 47.5 ml magnetic-activated cell sorting (MACS) rinsing solution (Miltenyi, 130-091-222) with 2.5 ml MACS BSA stock solution (Miltenyi, 130-091-376) per animal. This mixture was de-gassed on a magnetic mixer for 15 minutes and then stored on ice. After livers were collected from mice, they were transferred into a gentleMACS™ C tube (Miltenyi, 130-093-237) containing the dissociation mix (**Table 1**). The tube was closed and attached onto a sleeve of the gentleMACS Octo Dissociator after which the samples were resuspended and added onto a MACS SmartStrainer (70 µm, Miltenyi, 130-098-462). The flow-through was collected in a fresh 50 ml falcon tube. 5 ml DMEM (Gibco™, 11965092) were added to the C-tube to collect remaining cells and applied onto the strainer as well. Lastly, the falcons containing the separated cells, were centrifuged at 300 x g for 10 minutes.

Table 1. Components of the liver dissociation mix. All enzymes were stored at -20°C. Volumes account for the dissociation of one liver.

Components	Company	Volume
Enzyme D	Miltenyi	200 µl
Enzyme R	Miltenyi	100 µl
Enzyme A	Miltenyi	20 µl
DMEM	Gibco	4.7 ml
Total	-	5.02 ml

4.1.2. Magnetic labelling and separation

To isolate a single cell type from the generated single-cell solution containing all hepatic cell types, the immunomagnetic cell separation system with columns from Miltenyi was used. After the liver dissociation procedure, the supernatant was carefully aspirated and the

pellet resuspended with 5 ml PEB and centrifuged again at 300 x *g* for 10 minutes. Meanwhile, LS columns (Miltenyi, 130-042-401) for magnetic separation were equilibrated with 3 ml PEB. After centrifugation, the supernatant was removed, the pellet resuspended in 90 µl PEB and 10 µl of magnetic beads coupled to a CD146 antibody (Miltenyi, 130-092-007) were added. The falcons now containing the cell suspension and the magnetically labelled CD146 antibodies were put onto a rotator in the fridge (4°C) for 15 minutes. Afterwards, the cells were washed with 1 ml PEB and centrifuged at 300 x *g* for 10 minutes, then the supernatant was taken off and the pellet resuspended in 500 µl PEB. This cell suspension was now applied onto a previously equilibrated column and washed with 3 ml PEB two times, with the flow-through being collected. The columns were then removed from the magnetic field and with a plunger the magnetically labelled cells were washed out with 5 ml PEB onto the second column, to which a MACS SmartStrainer (Miltenyi, 130-098-458, 30 µm) was attached. After the column and the MACS SmartStrainer were washed two times with 3 ml PEB, the magnetically labelled cells were flushed out with 5 ml PEB into a fresh 15 ml falcon tube which was centrifuged at 900 x *g* for 3 minutes. Next, the supernatant was taken off and the pellet was resuspended in the amount of pre-warmed EBM-2 media with supplements (Lonza, CC-3162) which would result in 60.000 cells/well and then incubated at 37°C and 5% CO₂ for 4 hours, after which the cells could be further utilized. The wells were pre-treated for at least 30 minutes at RT with speed coating solution (PELOBioTech, PB-LU-000-0002-00, 500 µl/well).

4.2. Cell culture

4.2.1. SEMA3A-Fc treatment of mouse LSECs

After allowing MACS-isolated LSECs to grow for 4 hours, the cells were starved for another hour using EBM-2 media without supplements (Lonza, CC-3156). After one hour, the medium was aspirated again, and cells were treated with either a control protein (IgG2A-Fc, Recombinant Mouse IgG2A Fc Protein, R&D Systems, 4460-MG-100, Table 2), or different concentrations of recombinant semaphorin-3A (SEMA3A-Fc, Recombinant Mouse Semaphorin 3A Fc Chimera Protein, R&D Systems, 5926-S3-025, **Table 2**) in EBM-2 without supplements, however, the total amount of protein was always kept constant (**Table 3**).

After the cells were incubated at 37°C and 5% CO₂ for the desired amount of time, they were fixed in either PFA (4% in PBS) or Glutaraldehyde (2% in sodium cacodylate buffer).

Table 2. List of proteins used for LSEC treatment.

Protein	Company	Cat. No	Preparation
Recombinant Mouse IgG2A Fc Protein	R&D Systems	4460-MG-100	Reconstituted in 1 ml sterile PBS
Recombinant Mouse Semaphorin 3A Fc Chimera Protein	R&D Systems	5926-S3-025/CF	Reconstituted in 250 µl PBS containing 0.1% BSA

Table 3. Pipetting scheme for different concentrations of recombinant SEMA3A-Fc for a 24-well plate (500 µl).

Conditions [µg of SEMA3A-Fc/ml]	0	0.5	1	2
Recombinant Mouse IgG2A Fc Protein	10 µl	7.5 µl	5 µl	0 µl
Recombinant Mouse Semaphorin 3A Fc Chimera Protein	0 µl	2.5 µl	5 µl	10 µl

4.2.2. Antibody, inhibitor, and serum treatments of LSECs

After 4 hours of incubation, isolated mouse LSECs were treated with different types of anti-NRP1 antibodies (anti-NRP1^{SEMA3A}; Genentech, anti-NRP1^{Pan}; R&D Systems, AF566), whereas the anti-NRP1^{VEGF} antibody (Genentech) served as a control (**Table 4**). The antibodies were diluted with EBM-2 medium without supplements to a final concentration of 5 µg/ml, and the cells were incubated at 37°C and 5% CO₂ for 1 hour.

Mouse LSECs pre-treated with the LIMK1 inhibitor LIMKi 3, they were allowed to grow 4 hours and then incubated with LIMKi 3 (Tocris, Catalog No.: 4745) for 1 hour at 37°C and 5% CO₂. The inhibitor was diluted to a final concentration of 3 µM in EBM-2 medium without supplements and DMSO with a final concentration of 0.1%. As a control, the cells were treated with EBM-2 medium with the same concentration of DMSO (0.1%).

Table 4. Used blocking antibodies and their concentrations.

Antibodies	Company	Stock conc.	Final conc.
Nrp1-A (SEMA3A binding site)	Genentech	5.6 mg/ml	5 µg/ml
Nrp1-B (VEGF binding site)	Genentech	16.6 mg/ml	5 µg/ml
Nrp-1 blocking antibody (AF566)	R&D Systems	200 µg/ml	5 µg/ml

4.3. Palmitic acid treatment of human LSECs

LSECs were cultured in T75 flasks coated with Speed Coating Solution (PELOBiotech, PB-LU-000-0002-00) in microvascular EC growth medium supplemented with a microvascular EC growth kit enhanced (PELOBiotech, PB-MH-100-4099). For fatty acid treatments, LSECs (passage 4–6) were passaged in 12-well dishes coated with Speed Coating Solution (PELOBiotech, PB-LU-000-0002-00) and left to attach overnight. Thereafter, palmitic acid (Sigma-Aldrich, P5585) or fatty acid-free BSA (Sigma-Aldrich, A7039, lot SLCB3395) as a control were added to the cells and incubated for 2, 6, 18 or 24 hours. Finally, the medium was removed and the cells were collected in 350 μ l RTL lysis buffer (Qiagen) to isolate RNA, or fixed with PFA (4% in PBS) to stain F-actin.

4.4. SEM analysis

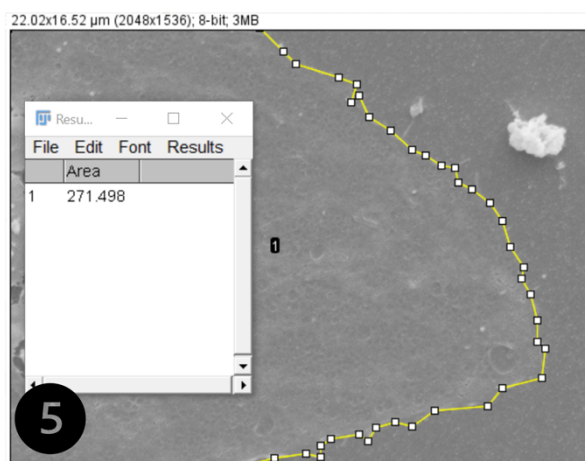
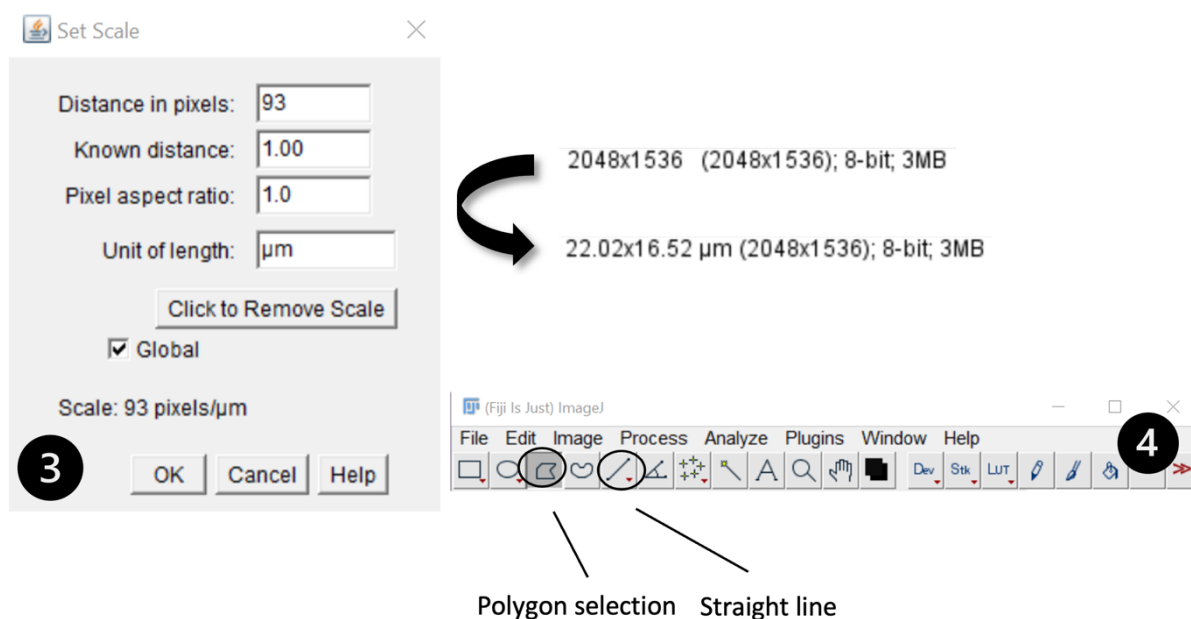
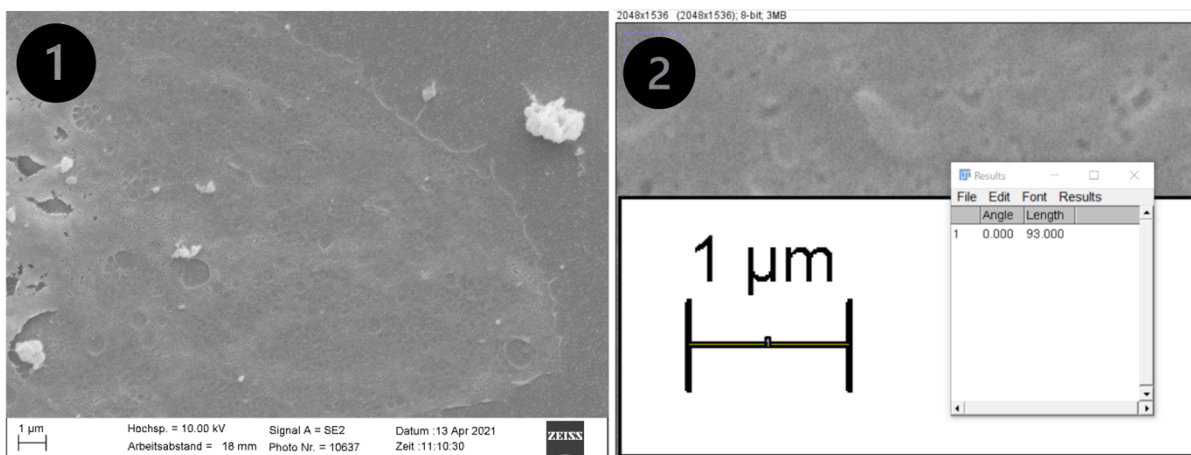
4.4.1. Preparation for SEM analysis of cells

After the cells have been treated, the glass plates were removed from the wells and transferred into a new 24-well plate already containing 500 μ l of glutaraldehyde solution (2% in sodium cacodylate buffer, for 2 ml of glutaraldehyde solution, 160 μ l of 25% glutaraldehyde (stock) solution were mixed with 1840 μ l sodium cacodylate buffer (0.1 M)) per well. The 24-well plates were then stored in the fridge overnight. The next day, the glutaraldehyde solution was taken off, and 500 μ l sodium cacodylate buffer (0.1 M) was applied onto each glass plate. Unless used for further experiments immediately, the cells were stored in the cacodylate buffer in the fridge. When the experiment was continued, the next steps were all performed under the fume hood. First, the sodium cacodylate buffer was taken off and the cells were incubated with 500 μ l OsO₄ (osmium tetroxide) solution (for 4 ml, 3 ml of 0.1 M sodium cacodylate buffer were mixed with 1 ml of 4% OsO₄) per well for 30 minutes. Next, the osmium solution was taken off and the cells were washed two times with 500 μ l of cacodylate buffer for 5 minutes. Then, 500 μ l of 70% ethanol was added into each well and incubated for 5 minutes. This step was repeated with 80% and 90% ethanol after which the glass plates were transferred into a 24-well plate containing 500 μ l of 100% ethanol and stored in the fridge until further use.

Next, the cells were chemically dried using TMS (Tetramethylsilane, ACROS Organics™, Thermo Fisher Scientific). Since TMS is extremely volatile, all steps were performed under the hood and the TMS was kept on ice during the experiment. Using a 5 ml plastic pipette, the TMS was added into each well, approximately until the volume doubled. After 30 minutes of incubation, TMS was again added until the volume doubled and incubated for 30 min. Thereafter, the cells were aspirated and a few drops of TMS were added into each well, just covering the glass plate, and incubated for 30 min. After the TMS was aspirated, a few drops of TMS were added into each well, and the plates were left under the hood to dry overnight. The next day, the plates were removed and attached onto SEM specimen stubs (12.5 mm Ø, 3.2 x 8 mm pin) using double sided adhesive circles. Using a sputter coater, the plates were coated with a thin layer of gold in a controlled and even manner. After this step, the samples were ready to be examined by the SEM. For image acquisition, the Leo 1430 VP SEM, Zeiss FIB-SEM 540 Crossbeam, or Zeiss SUPRA 55VP together with the Zeiss imaging software (SmartSEM), was utilized.

4.4.2. Manual fenestrae quantification of LSECs

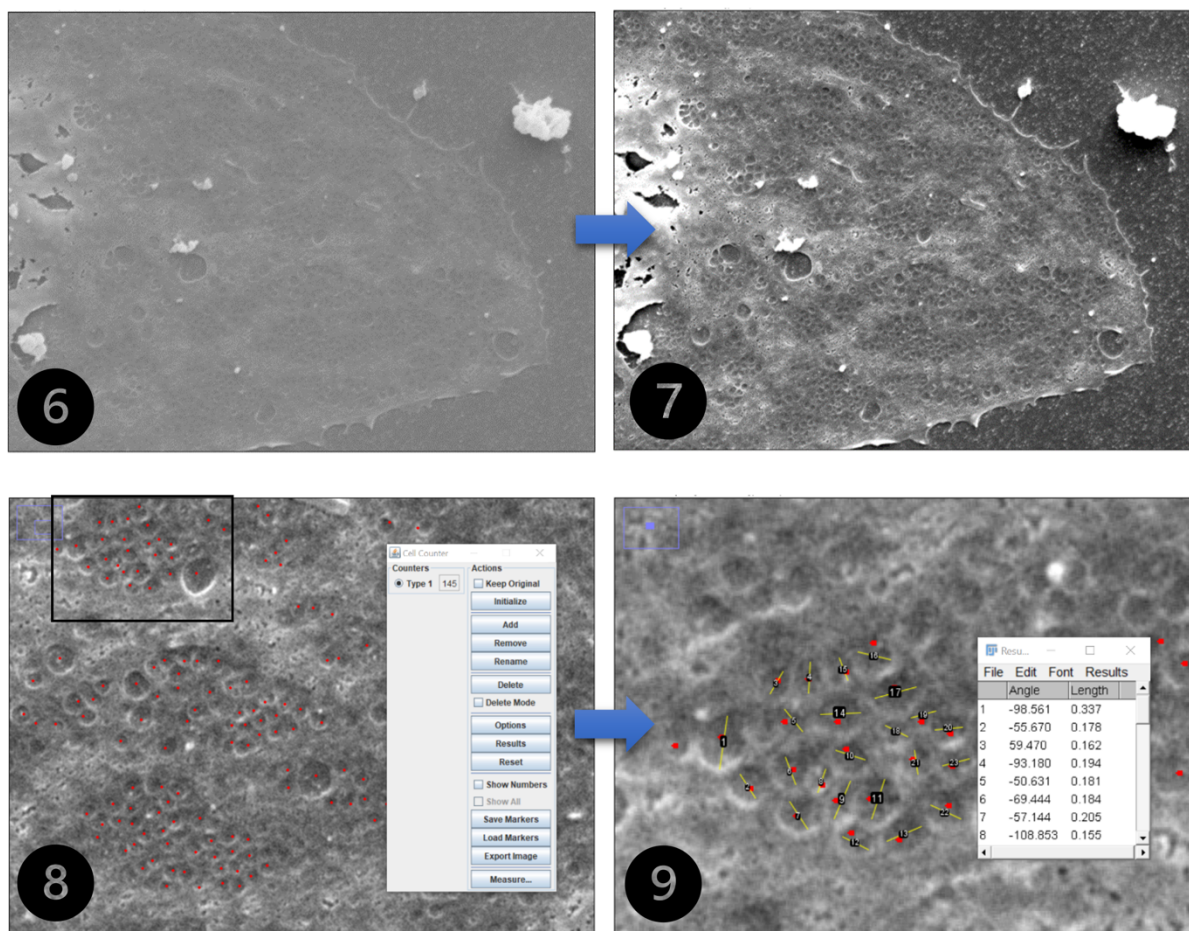
For the morphologic analysis of LSECs, the images obtained with the SEM were examined using the Fiji imaging processing package. Analysed features were the fenestrae frequency, i.e. the number of fenestrations per μm^2 , the LSEC porosity, i.e. the ratio of fenestrated area to the analysed cell area, and the fenestrae diameter. First, the scale was set from pixel to μm , in order measure all parameter in the intended unit. To do so, an image from the SEM with the scale bar on in was opened in Fiji (①) and the straight line tool (④) was used to determine the length of the scale bar in pixels (②). Those measurements were then used to set the scale (③, Analyze → Set scale...). Here, 1 μm correlated to 93 pixels in length.



Next, the cell area was determined, using the polygon selection tool (④). The outline of the cells was traced, and the area measured in μm^2 (⑤). In order to now count the number of fenestrae on the LSEC surface, the Cell Counter Plugin was utilized (Plugins → Analyze → Cell Counter → Cell counter). For a better resolution,

the contrast and brightness were adjusted and the processing tool “smooth” was applied (Image → Adjust → Brightness/Contrast, Process → Smooth, ⑥ before, ⑦ after). Then, the fenestrae were counted and a copy where all the fenestrae are flagged was saved (⑧), to aid the measuring of the fenestrae diameter. The diameter was measured using the

straight line tool and the measurements were given in μm (9), Length in table). All obtained measurements were used to calculate above mentioned parameters by using the formulas given in **Figure 7**.



$$\text{fenestrae area} = \pi r^2 \qquad r = \frac{d}{2}$$

$$\text{fenestration frequency } [\mu\text{m}^{-2}] = \frac{\text{number of fenestrae}}{\text{analysed cell area } [\mu\text{m}^2]}$$

$$\text{LSEC porosity } [\%] = \frac{\sum \text{fenestrae area } [\mu\text{m}^2]}{\text{analysed cell area } [\mu\text{m}^2]} \times 100$$

r = Radius
 d = Diameter
 Σ = Sum
 π = pi

Figure 7. Formulas used for the analysis of images taken of mouse LSECs with the SEM.

4.4.3. Fenestrae quantification of LSECs using a deep learning workflow

For the morphologic analysis of LSECs, the images obtained with the Zeiss FIB-SEM 540 Crossbeam or SUPRA 55VP were examined using a deep-learning workflow that is based on the uncertainty-aware variant of the Contour Proposal Network (CPN) and was developed together with Eric Upschulte and Dr. Timo Dickscheid from the Research Centre Jülich^{248,249}. This model was specifically chosen for its capability to directly predict object contours in biomedical image data, providing an accurate representation of object shapes and sizes. It uses a U-Net architecture with a ResNeXt-101 encoder^{250,251}. This setup utilized a pretrained network (ginoro_CpnResNeXt101UNet-fbe875f1a3e5ce2c) from the celldetection Python package (<https://github.com/FZJ-INM1-BDA/celldetection>), designed for multimodal cell segmentation. The model was fine-tuned using manual annotations and applied with an ensemble strategy. Computations were performed on the JUWELS supercomputer²⁵².

4.4.4. Fenestrae quantification of sinusoids using Fiji WEKA classifier

The SEM images of liver sinusoids were quantified using Fiji with help of the trainable WEKA segmentation plugin, a workflow developed by Dr. Daniel Eberhard^{253,254}. Firstly, an automatic contrast ("Normalize Local Contrast") was calculated for each SEM image and the polygon selection tool of Fiji was used to manually mark the area of interest (sinusoid area) and all non-sinusoid area and gaps were cleared. Next, fenestrae area and sinusoid cell surface area were identified using a data-set-trained-classifier segmentation (WEKA) algorithm in Fiji^{253,254}. The classifier was trained using typical images from the same scanning electron microscope before and stored in a classifier file. The classifier segmentation (WEKA) algorithm led to the generation of probability maps for cell surface area and fenestrae area. Finally, the maps were used to calculate the overall surface area of the sinusoid and also to quantify fenestrae using the "analyze Particles" feature which returns area and diameter of each object. Small objects (diameter < 35.68 nm), or objects with a low circularity (circularity < 0.50) were excluded from the analysis as fenestrae are expected to be round or oval in shape. The data was transferred to Excel (Microsoft) and the fenestrae frequency and LSEC porosity was calculated.

4.5. Gene expression analysis

To quantify gene expression in cells, mRNA was isolated using the RNeasy kit (QIAGEN). cDNA was synthesized using Oligo (dT) primers (Eurogentec) and MMLV reverse transcriptase (Promega) according to the suppliers' instructions. qPCR was performed on a Mx3000P (Agilent Technologies) or Quantstudio 5 (Applied Biosystems) qPCR Machine using Brilliant III Sybr green (Agilent Technologies). To exclude the involvement of unspecific PCR products, –RT controls were performed and PCR melting curves of each PCR product were evaluated. Samples with faulty dissociation curves (more than two peaks) were excluded from further analysis. PCRs for all samples were run in triplicate. Relative gene expression was calculated according to Schmittgen and Liva²⁵⁵ using the formula $2^{-(CT_{\text{gene of interest}} - CT_{\text{reference gene}})}$. Finally, individual samples were plotted as fold expression with respect to the mean of the control group.

Table 5. RT-qPCR primer sequences.

Gene	FW Sequence 3' → 5'	RV Sequence 5' → 3'	Species
<i>HPRT</i>	TGACACTGGCAAACAATGCA	GGTCCTTTTCACCAGCAAGCT	Human
<i>GAPDH</i>	CCTGTTCGACAGTCAGCCG	CGACCAAATCCGTTGACTCC	Human
<i>SEMA3A</i>	TGTTGGAGCAAAGGATCACA	TCTTTTCCAGCCCAGTTGCA	Human
<i>Rplp0</i>	GATGCCCAGGGAAGACA	ACAATGAAGCATTTTGGATAATCA	Mouse
<i>Sema3a</i>	GGATGGGTCCTCATGCTCAC	TGGTGCTGCAAGTCAGAGCAG	Mouse

4.6. Western blotting

4.6.1. Protein isolation

For protein isolation, LSECs were washed briefly with 1 ml of DPBS. Afterwards 180 µl of RIPA buffer was added to each well and incubated for 5 minutes on ice. Using the cell scraper, cells were then transferred into a new 1.5 ml Eppendorf tube. Those were put onto the cell disruptor (Disruptor genie, Scientific Industries) for 10 minutes and allowed to sit at 4°C for 15 minutes. Subsequently, the lysates were centrifuged at 4°C and 15.700 x g (Centrifuge 5415 R, Eppendorf). The supernatant was transferred into new 1.5 ml Eppendorf tubes and stored at -80°C until further use.

4.6.2. Bicinchoninic acid assay

To quantify the amount of protein in the samples from the protein harvest, a bicinchoninic acid (BCA) assay using the Pierce BCA protein assay kit (Thermo Scientific, 23225) was performed according to the manufacturer's instructions. For the western blot, all samples were filled up with H₂O to 30 µl and 10 µl of 4x Laemmli sample buffer (180 µl 4x Laemmli stock, 20 µl NaF, 40 µl Protease inhibitor (Roche), 10 µl β-Mercaptoethanol) was added. The samples were incubated at 95°C for 5 minutes for protein denaturation. Following, the samples were put on ice for immediate use.

4.6.3. Western blotting

A Mini-PROTEAN™ TGX Stain-Free™ Protein Gel was loaded with 5 µl of PageRuler Prestained Protein Ladder (Cat: 26616, Thermo Fisher) and 10 µl sample (each containing the same amount of protein) per lane. Gels were run at 120 V for approximately 40 minutes. The gel was immediately activated using UV light for 5 minutes. After imaging the gel, two ion transfer stacks and the blotting membrane were assembled in the transfer chamber of the Trans-Blot Turbo according to manufacturer's instructions (**Figure 8**). Following the transfer, the blot was imaged using the Bio-Rad ChemiDoc™ MP Imaging software. Then, the blot was blocked in 5% milk in 1 x PBST for 1 hour at room temperature.

To visualize cofilin-1 and phospho-cofilin-1, the blots were incubated for at least 16 hours or overnight in the primary antibody at 4°C on a horizontal shaker (antibodies: phospho-cofilin, Cell Signaling, 3313T, 1:750; cofilin, Cell Signaling, 5175T, 1:750, GAPDH, abcam, ab9485, 1:2500).

Afterwards the blots were washed three times with 1x PBST for 5 minutes and then incubated for one hour in the secondary antibody (antibodies: Anti-rabbit IgG, HRP linked antibody, Jackson Immuno Research, 711-035-152, 1:4000; Anti-rabbit IgG, HRP linked antibody, Invitrogen, G21234, 1:2000) on a horizontal shaker at room temperature. Blots were washed again three times with 1x TBST for 5 minutes before applying Pierce ECL Western Blotting substrate (32132, Thermo Fisher) onto the membrane to detect specific protein bands. The membrane was incubated in the substrate for 5 minutes and the ChemiDoc™ MP (Bio-Rad) and the ImageLab 4.1 software from Bio-Rad were used to develop and analyse images.

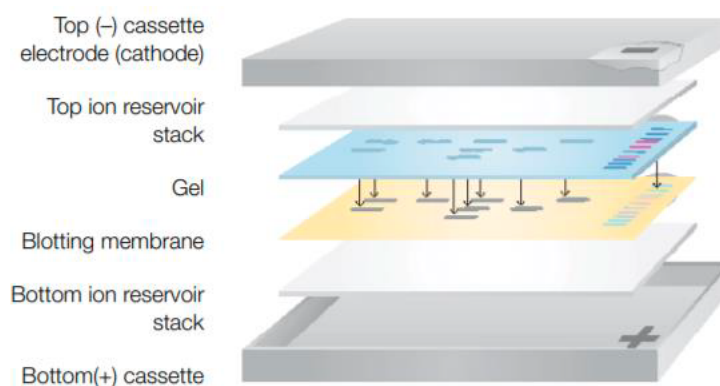


Figure 8. Picture of Trans-Blot Turbo assembly.

Picture was obtained from the Bio-Rad Trans-Blot Turbo System Instruction Manual (Catalog #1704150).

4.7. PamGene kinase activity profiling

To perform kinase activity profiling, mouse LSECs were isolated using MACS and cells were seeded at 1 million cells/well in a 6-well plate. After 4 hours, cells were starved for 1 hour and then treated for 10 minutes with 1 $\mu\text{g}/\text{ml}$ of either SEMA3A-Fc or IgG2a-Fc. Afterwards, the 6-well plate was put on ice, the culture medium was removed, and cells were washed with cold PBS. After removal of the PBS, the washing step was repeated. Lysis buffer (Halt Phosphatase Inhibitor Cocktail 1:100 and Halt Protease Inhibitor Cocktail EDTA free 1:50 in M-PER Mammalian Extraction Buffer) was added to the cells and cells were collected using a cell scraper. Cells were kept on ice and lysed by pipetting up and down several times over the course of 15 minutes. Samples were centrifuged for 15 minutes at $16.000 \times g$ at 4°C . The lysate was collected and transferred to a clean vial on ice. After snap-freezing in liquid nitrogen, samples were stored at -80°C until transport to the PamGene facility. The analysis and data-processing were performed by PamGene using the BioNavigator[®] software.

4.8. Phalloidin staining

To stain F-actin in LSECs, cells grown on glass plates were fixed with 4% PFA and washed with PBST (0.2% Triton-X100) three times. 5 μl of the stock solution (Alexa Fluor[™] 488 Phalloidin, A12379, Abcam) were diluted with 200 μl PBS for each sample. After 30 minutes

incubation in the dark at room temperature, plates were washed three times with PBST (0.2%), and cell nuclei were stained with DAPI (D9542, Sigma-Aldrich) prior to mounting.

4.9. Measuring corrected total cell fluorescence (CTCF)

Corrected total cell fluorescence (CTCF) was measured as described by Bora et al., 2021²⁵⁶. In Fiji the image was opened and the cell of interest was selected. Using Analyze > Measure, the integrated density, area, and mean grey value were measured. Additionally, a small area where no fluorescence was present was measured for the background fluorescence. Using those parameters, the CTCF was calculated according to the formula in **Figure 9**.

$$\text{CTCF} = \text{Integrated density} - (\text{Area of selected cell} \times \text{Mean fluorescence of Backgrounds})$$

Figure 9. CTCF calculation.

4.10. G-actin/F-actin *in vivo* assay biochem kit

To quantify F- and G-actin in LSECs, the G-Actin/F-Actin *In Vivo* Assay Biochem Kit from Cytoskeleton, Inc. (Cat. # BK037) was used. To this end, mouse LSECs were isolated using MACS, incubated for 4 h, starved for 1 h, and treated for 1 hour with 1 µg/ml of either SEMA3A-Fc (R&D Systems) or IgG2a-Fc (R&D Systems), while human LSECs were passaged and then treated as described previously. The division of F- and G-actin was performed according to the Kit's description. Afterwards, both fractions were analyzed using western blotting (antibodies used: Anti-Actin MAb (clone 7A8.2.1, Cat: AAN02-S). For quantification, a dilution series was used to generate a standard curve.

4.11. Serum parameters

To measure triglycerides, ALT, AST, total cholesterol, and HDL-Cholesterol in blood serum of mice (4 hours fasting), the Kenshin-2 Spotchem 4430 test stripes were used in combination with the SPOTCHEM EZ™ SP-4430. Values below <15 (n.d.) were defined as 15. The samples were measured according to the manufacturer's description. NEFA was measured using the NEFA-HR(2) Assay (FUJIFILM Wako Chemicals Europe GmbH) and insulin was measured using an ultra-sensitive rat insulin ELISA (Crystal Chem; Cat: 90060). HOMA-IR was

calculated as (insulin * glucose [ng/ml * ml/dl]/405) and Adipo-IR (free fatty acid × insulin [mmol/L/pmol]).

4.12. Animal handling

Male C57BL/6J mice (9-11-weeks-old, Janvier, France) and male and female *db/db.BKS* and *db/+.BKS* mice were used for gene expression studies and/or LSEC isolations. Intravenous NRP1-antibody injections (tail-vein) were performed by Dr. Paula Follert (Institute of Metabolic Physiology, HHU). 10-week-old male *db/db.BKS* mice were treated with 10 mg/kg body weight NRP1^{SEMA3A} antibody from Genentech or an isotype and concentration matched IgG control (BioCell, *InVivoPlus*[™], mouse IgG2a isotype control, clone C1.18.4, Cat #: BP0085, Lot #:833922A2), both in approximately 100 µl of NaCl (0.9%). The antibody or the control were administered every third day over the course of 16 days. Specifically, animals were taken out of the cage, put into a restrainer and, after warming the tail with 37°C water, either the antibody or the control were administered.

For conditional vascular endothelial cell specific deletion of *Sema3a*; *Cdh5-Cre^{ERT2}* mice²⁵⁷ were mated with floxed *Sema3a^{fl/fl}* (backcrossed to C57BL/6J) mice²⁵⁸, fed with HFD (D12492, Research Diets) for 10 weeks, injected with 75 mg/kg body weight of tamoxifen (Sigma, T5648) in peanut oil (Sigma, P2144) for 5 consecutive days and fed with HFD for an additional 10 weeks, all performed by Dr. Daniel Eberhard. *Cdh5-Cre^{ERT2}* mice were used as controls and were treated equally.

Genotyping was performed according to Taniguchi et al., Licht et al., and Madisen et al.²⁵⁸⁻²⁶⁰. All mice were held at 22°C (+/- 2°C), 55% (+/- 5%) humidity, lighting (6:00 a.m. - 6:00p.m.), fed with standard chow (Sniff, V1184-300; crude protein (N x 6,25) 23%; crude fat 6.1%; crude fiber 3.3 %; crude ash, 6.5%; starch 34.1%; sugar 5,1%; N free extracts 49.8%; energy from fat 16kJ%; protein 27kJ% and carbohydrates 57kJ%) or high-fat diet (D12492, Research Diets, energy from fat 60 kcal%; formulation: protein (200 g casein, Latic 30 Mesh; 3g cysteine L), carbohydrates (125 g Lodex 10, 72,8 g sucrose); fibre (50 g Solka Floc, FCC200); fat (245 g lard, 25 g soybean oil, USP), mineral (50 g S10026B); vitamin (2 g choline bitartrate, 1 g V10001C) and dye (0.05 g blue FD&C, Alum. Lake 35-42%)) and had free access to water.

4.13. Mouse liver perfusion

The perfusion was performed according to the protocol from Cogger et al.²⁶¹. After the livers were perfused, they were prepared for the SEM. First, the livers were washed at least three times with 0.1 M sodium cacodylate buffer in order to remove as much glutaraldehyde from the EM fixative buffer as possible as it can cross-react with the OsO₄ applied in the next step, resulting in artefacts on the SEM. Afterwards, the livers were incubated with 2% OsO₄ in 0.1 M sodium cacodylate buffer for 2 hours at room temperature. Next, in order to dehydrate the livers, they were rinsed with increasing concentrations of ethanol. First, they were incubated with 50% ethanol for 5 minutes, then three times for 5 minutes with 70% ethanol, three times for 5 minutes with 90% ethanol, two times for 5 minutes with 100% ethanol, and lastly two times for 10 minutes with 100% ethanol.

To finish, the livers were chemically dried with TMS (ACROS Organics™, Thermo Fisher Scientific). As TMS is extremely volatile, itself and the samples were constantly kept on ice and the next steps were performed under a fume hood. Roughly, the same amount of TMS as ethanol was applied onto the livers, to reach a 1:1 ratio of ethanol and TMS and allowed to incubate for 30 minutes. Afterwards, the same amount TMS was added again to reach a ratio of 1:2 of ethanol to TMS and incubated for 30 minutes after which the ethanol and TMS mixture was removed and pure TMS was added. After another 30 minutes, the TMS was removed and fresh TMS was added. Lastly, the tubes containing the livers were opened to allow the TMS to evaporate overnight under the hood.

The next day, the livers were placed onto specimen stubs (12.5 mm Ø, 3.2 x 8mm pin) using double sided adhesive circles. Using a sputter coater, the plates were coated with a thin layer of gold in a controlled and even manner. By coating the specimen with a conductive material, charge build-up on the specimen's surface is prevented. It is critical that the coating is thick enough to prevent charging (typically around 10 nm) but not thick enough to obscure specimen surface details. After this step, the samples were ready to be examined by the SEM. For image acquisition, the Leo 1430 VP SEM, Zeiss FIB-SEM 540 Crossbeam, and Zeiss SUPRA 55VP together with the Zeiss imaging software (SmartSEM), were utilized.

4.14. VLDL secretion assay

Mice were weighed and subjected to a 4-hour fast before undergoing the VLDL secretion test. In the test, 0.5 g/kg body weight (BW) of WR-1339 (Sigma, T8761) was intraperitoneally injected and blood was collected from the tail tip pre-injection and after 1, 2, 4 and 6 hours after Triton WR1339 injection using EDTA-coated tubes, followed by plasma preparation through a 10-minute centrifugation at 2.000 x *g*. Triglycerides were measured using a LabAssay Triglyceride kit (FUJIFILM Wako Chemicals Europe GmbH) according to the suppliers' instructions.

4.15. Statistics

All imaging analyses were performed under blinded conditions. Data were gathered and processed using Excel (Microsoft) and then transferred to GraphPad Prism to generate all graphs. All data points were plotted individually together with the mean and s.e.m. Statistical analyses were performed using GraphPad Prism Version 10.2.3 (347) for Macintosh (GraphPad Software, San Diego, CA). No statistical outlier tests were applied. If necessary, samples/data were solely removed based on technical issues during the experiments. A two-tailed unequal variances *t*-test (Welch's test) was used to determine statistical significance between two independent experimental groups. A pairwise Student's *t*-test was performed to determine statistical significance for samples of the same mouse. In case of multiple *t*-tests in the same analysis a multiple two-tailed *t*-test (paired or unpaired) with a two-stage step-up method according to Benjamini, Krieger and Yekutieli was used to correct for multiple comparisons and to detect significant discoveries. For more than two experimental groups with one or two factors, a one- or two-way analysis of variance (ANOVA) (with or without repeated measurements) was conducted. Multiple comparisons were corrected for using the Dunnett's, Tukey's, or Šidák's *post hoc* test. The *p*-value is displayed depending on its significance ($p < 0.05$) and whether it is mentioned in the results paragraph.

4.16. Personal contributions

Most of the experiments were performed by Sydney Balkenhol, supervised by Prof. Dr. Eckhard Lammert and Dr. Daniel Eberhard. This experiments/the contributors of this study were supported and funded by the Heinrich Heine University Düsseldorf, the DDZ, the German Research Foundation (DFG, La1216/6-1 and RTG 2576 vivid), the Federal Ministry of Health, the Ministry of Culture and Science of North Rhine-Westphalia, the German Center for Diabetes Research (DZD), the Schmutzler Foundation and European Community (HORIZON-HLTH-2022-STAYHLTH-02-01: panel A) to the INTERCEPT-T2D consortium, and the Hector Foundation under the project number MED2302. Sydney Balkenhol is supported by the Studienstiftung des Deutschen Volkes.

The training of the cell segmentation tool with SEM images of LSEC and the streamlining of the measurements of fenestrae (**Figure 11b-d**) was performed by Eric Upschulte under supervision of Dr. Timo Dickscheid, who received funding from the Priority Program 2041 (SPP 2041) 'Computational Connectomics' of the DFG and the European Union's Horizon Europe Programme under specific grant agreement no. 101147319 (EBRAINS 2.0 Project) and the Helmholtz Association's Initiative and Networking Fund through the Helmholtz International BigBrain Analytics and Learning Laboratory under the Helmholtz International Laboratory grant agreement, InterLabs-0015.

The analysis of the samples, generation of heatmaps, volcano plots and PCA of samples (**Figure 15a-c**) was performed solely by PamGene.

Human LSEC culture and palmitic acid treatment of human LSECs (**Figure 18a, d**) was performed by Dr. Daniel Eberhard. RT-qPCR analysis of human LSECs was performed by Andrea Köster (**Figure 18d**).

Intravenous administration of the NRP1^{SEMA3A}-blocking antibody in *db/db* (**Figure 21**) was performed by Dr. Paula Follert (funded by the 'Intra- and interorgan communication of the cardiovascular system' (IRTG 1902)) and Dr. Linda Große-Segerath. The measurement of non-esterified fatty acids (NEFA) and liver triglycerides (TG), as well as ORO stainings and analysis was performed by Dr. Daniel Eberhard (**Figure 21j-l**).

The generation of the *iEC^{Sema3a}* and *iEC^{wt}* mice, the VLDL secretion assay and measurement of physical parameters such as body weight, liver weight, blood insulin, blood glucose, and free fatty acids (**Figure 22a-d, i-k**), was performed by Dr. Daniel Eberhard.

The LSEC isolation from *db/db* mice was performed by Celina Uhlemeyer and Bengt-Frederik Belgardt (funded by the DFG within the Research Training Group GRK2576), while the RT-qPCR was performed by Dr. Daniel Eberhard and Andrea Köster (Supplementary Figure 6).

I thank S. Köhler (CAI, Heinrich Heine University Düsseldorf) and A. K. Bergmann (Core Facility, UKD Düsseldorf) for their help with SEM. I also acknowledge the Gauss Centre for Supercomputing (www.gauss-centre.eu) for funding this project by providing computing time through the John von Neumann Institute for Computing on the GCS Supercomputer JUWELS at Jülich Supercomputing Centre and the computing time granted through JARA on the supercomputer JURECA at Forschungszentrum Jülich. I am also grateful to Genentech for providing the NRP1-blocking antibodies.

5. Results

5.1. LSEC and fenestrae: establishment of quality and analysis

5.1.1. Quality assessment of MACS-isolated mouse LSECs

For upcoming cell culture experiments, it was important to ensure that the utilized LSEC isolation method results in fenestrated LSECs. Thus, we aimed to evaluate the quality of MACS (magnetic-activated cell sorting)-isolated LSECs, using the percentage of fenestrated LSECs as a determinant for well-isolated/healthy LSECs. Further, we were interested whether the magnetic beads used in MACS might impede the quantification of fenestrae. To this end, high-magnification scanning electron microscope (SEM) images of MACS-isolated LSECs (CD146⁺ cells) were taken, in that 60 cells were chosen at a random and analysed for the presence of fenestrations and magnetic beads. As to be seen in **Figure 10a** small circular specimens with a light appearance are to be found at magnifications of 58.56k with a size of approximately 50 nm, which is the size of a magnetic bead according to the manufacturer. Further, 60 cells/isolation were analysed for the presence of fenestrae (**Figure 10b**) showing a significantly higher number of fenestrated LSECs *versus* non-fenestrated LSECs (*av. 98.33% vs 1.67%, $p < 0.001$, Figure 10c*).

To conclude, magnetic beads can be found on MACS-isolated LSECs, while the vast majority of MACS-isolated cells presents with fenestrations, indicating the suitability of MACS-based methods for studying LSEC fenestration.

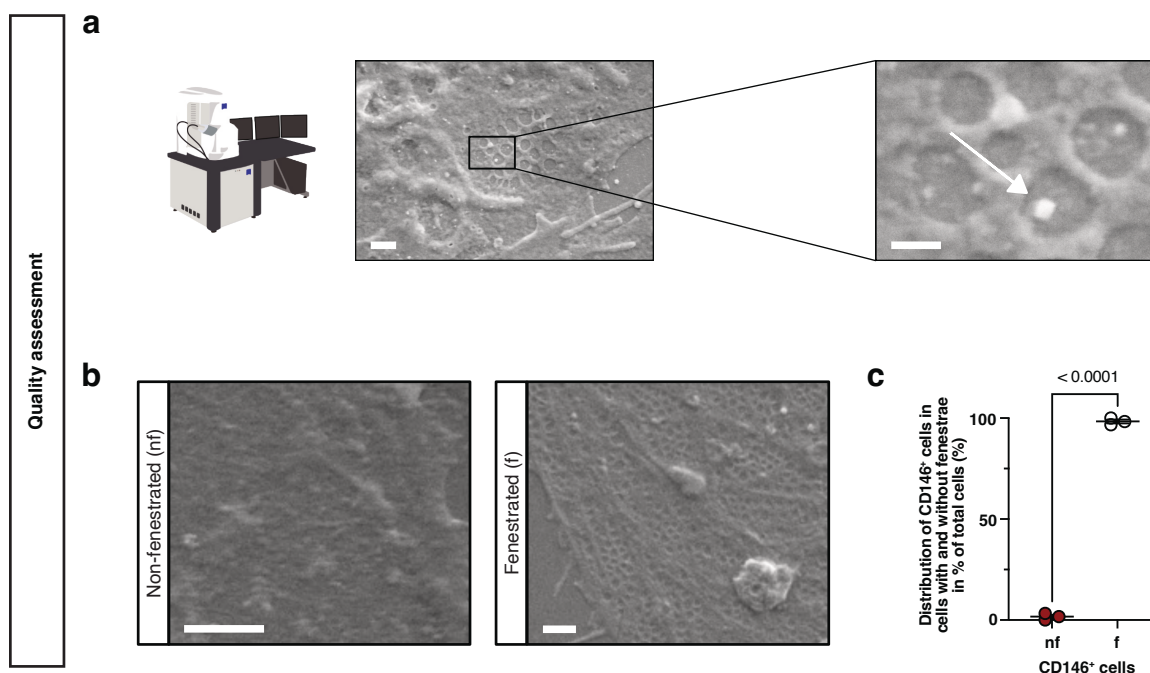


Figure 10. Quality assessment of MACS-isolated mouse LSECs.

a LSECs were isolated and incubated for 4 hours in EBM-2 media. An arrow points to a potential magnetic bead located within a fenestra, scale bars = 400 nm (left) and 100 nm (right, $n = 1$ LSEC isolation). For better visualisation, contrast and brightness were adjusted. The SEM was illustrated by Sydney Balkenhol. **b** After isolation, mouse LSECs were allowed to grow for 4 hours prior to SEM analysis. Example images representing non-fenestrated (nf), and fenestrated (f) CD146⁺ cells are shown. Scale bars = 1 μm. **c** Analyses of 60 randomly chosen cells regarding the occurrence of fenestrations. For statistical analysis a two-tailed unequal variances *t*-test was performed ($n = 3$). In the graph data points, mean \pm s.e.m., and the *p*-value are presented.

5.1.2. Development of a deep learning workflow for fenestrae analysis

Manual analysis of fenestrae is a time-consuming process which can be biased and take several days. In order to streamline this process, we collaborated with the Research Centre Jülich¹. Here we present a deep learning workflow (DLW), originally designed for multimodal cell segmentation, which was trained with previously analysed SEM images of fenestrated LSECs, and thus should be able to automatically detect and measure fenestrations in SEM images of mouse LSECs.

The first step of this process was to ensure that the segmentation tool is able to identify fenestrae. To this end we made overlays for SEM images where the fenestrae were coloured in white (**Figure 11a**). These images were used to train the DLW associated model, after which we could confirm that the model is indeed able to identify fenestrae (**Figure 11b**). In order to further improve the model and also measure fenestrae automatically, SEM images

¹ <https://www.fz-juelich.de/de/inm/inm-1/forschung/big-data-analytics>

with a manually drawn diameter for each fenestra were used as training data. To finally verify the functionality, we performed a correlation analysis of manually and automatically analysed images. For the interpretation, the output tables were parsed with a custom python script (Supplementary Figure 5) which determines the total fenestrae number, average diameter, and total fenestrae area. The cell area was measured manually.

As to be seen in **Figure 11c** the annotated SEM image shows a high density of recognized fenestrae. The results show a strong correlation between manually and automatically analysed images, regarding the fenestrae number ($R^2 = 0.9621$), frequency ($R^2 = 0.9376$), and diameter ($R^2 = 0.9254$), as well as LSEC porosity ($R^2 = 0.9642$, **Figure 11d**), displaying the predictive power of the DLW.

In summary, the DLW is able to identify fenestrae and analyse their diameter and number in SEM-obtained images of LSECs reliably and invariably.

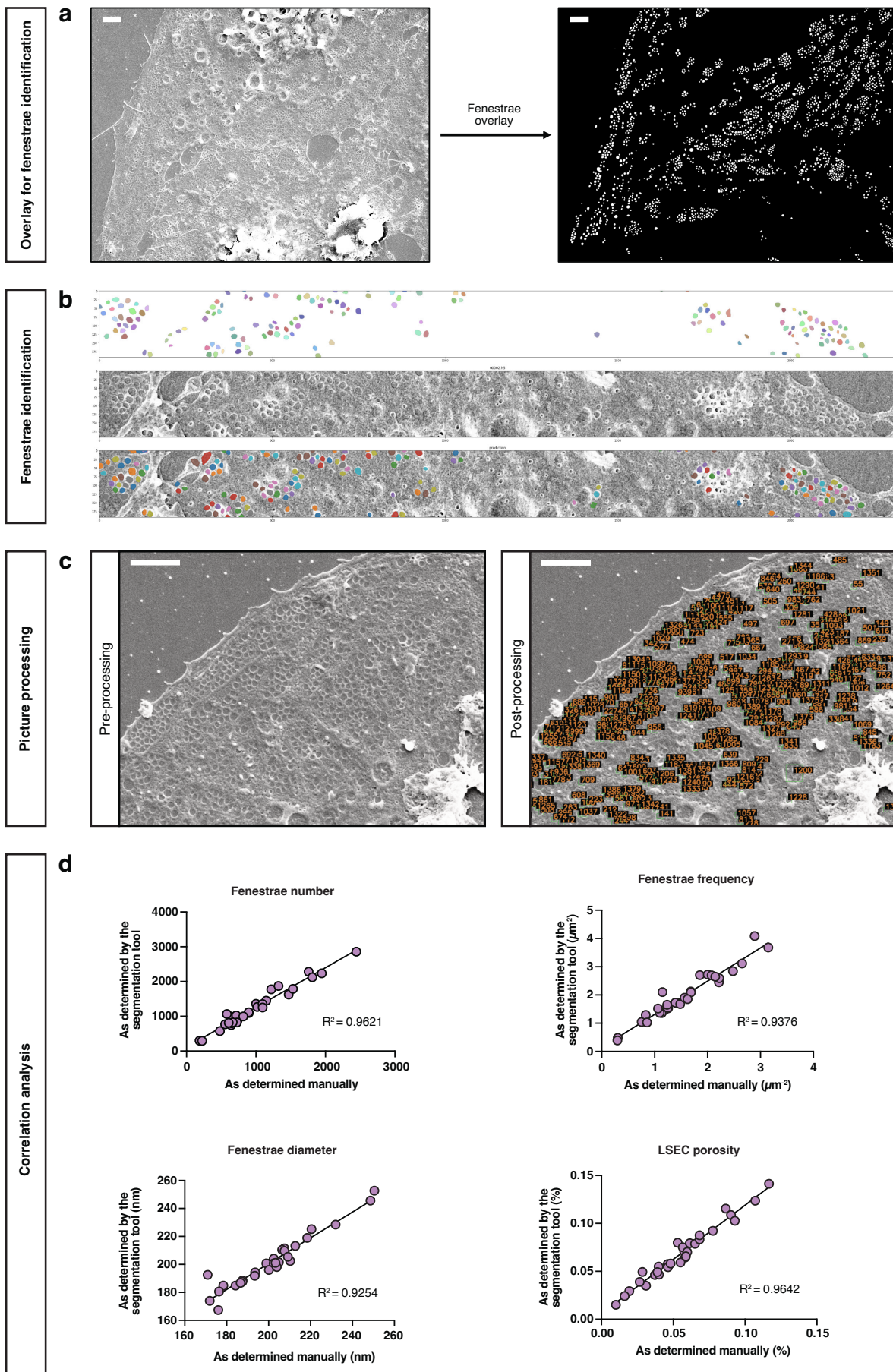


Figure 11. Deep learning workflow development.

a SEM image before (left) and after (right) overlaying the fenestrae, scale bars = 2 μm . **b** Fenestrae identification output. Identified fenestrae (top), original image (middle), and both merged (bottom). Generated by Eric Upschulte. **c** Example images of LSECs pre- (input file) and post-processing (output file) as received by the deep learning workflow. Scale bars = 2 μm . **d** Correlation analysis of 30 images which were analysed either manually or using the deep learning workflow regarding their fenestrae number, fenestrae frequency, fenestrae diameter, and LSEC porosity. Each dot represents one analysed image.

5.1.3. LSECs lose their fenestrae after 24 hours while SEMA3A-Fc treatment does not impair LSEC size or viability

Several studies have shown that cultured LSECs lose their fenestrations over time^{95,262}. In order to ensure that the experiments we will be conducting are not affected through cultivation-induced defenestration, we aimed to evaluate during which time period MACS-isolated LSECs defenestrate. Furthermore, we were interested whether SEMA3A-Fc would impair cell viability by reducing ATP levels or the size of fenestrae via cell shrinking/contraction.

Hence, mouse LSECs were isolated using MACS, allowed to adhere to glass plates for 4 hours, cultured for 1, 2, and 24 hours, and prepared for SEM analysis. For each time point, SEM images were taken and the cells were manually analysed for fenestrae diameter and number. Additionally, LSECs were starved for 1 hour and then treated with different concentrations of SEMA3A-Fc for another hour, after which the cell size, using DAPI and phalloidin staining, and intracellular ATP content, using the CellTiter Glo Assay, were measured.

Although cells were fenestrated at each of the time points, LSECs lost nearly half of their porosity after 24 hours compared to 1 hour (*av.* 5.84% vs 3.01%, $p = 0.2901$, **Figure 12d**), whereas the fenestrae diameter remained unchanged throughout all conditions (**Figure 12e**). The fenestrae frequency was significantly decreased after 24 hours compared to 1 hour (*av.* 1.838 μm^{-2} vs 0.693 μm^{-2} , $p = 0.0346$, **Figure 12c**).

Analysis of the cell size showed that the average cell size did not change, neither after treatment with low, nor high concentrations of SEMA3A-Fc (**Figure 12f**). Treatment of cells with SEMA3A-Fc also did not significantly change the amount of intracellular ATP detected (**Figure 12g**).

In conclusion, LSECs lose approximately 50% of their porosity in the first 24 hours of cultivation while short-term incubation with SEMA3A-Fc does not impair intracellular ATP content or cell size.

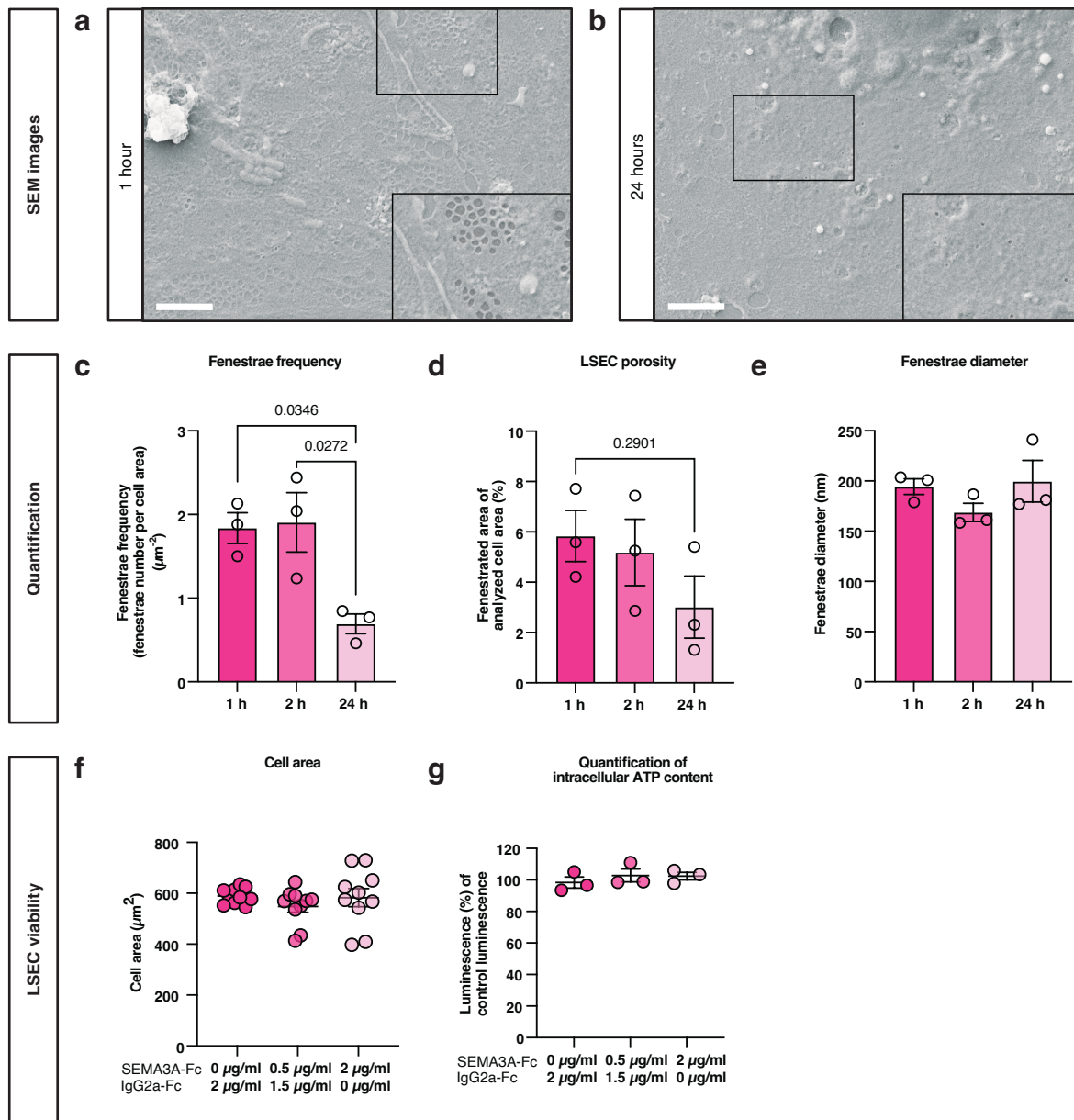


Figure 12. Cultured mouse LSECs lose fenestrae over time while SEMA3A-Fc does not affect cell size or ATP content.

a, b SEM images of isolated mouse LSECs which were cultured in EBM-2 medium with supplements for 1 (a) and 24 hours (b), after 4 hours pre-culture. The fenestrae were colorized with a digital charcoal pencil for better visualization. Scale bars = 2 μm . **c-e** Quantification of SEM images. For each condition, 10 images were analysed for fenestrae frequency (c), LSEC porosity (d), and fenestrae diameter (e). The analysis was performed manually. A one-way ANOVA with multiple comparisons (Tukey's *post hoc* test) was performed for statistical analysis ($n = 3$ independent LSEC isolations). **f** Effect of different SEMA3A-Fc concentrations on LSEC size. Cells were cultured for 4 hours, starved for 1 hour, and treated with SEMA3A-Fc and/or IgG2a-Fc for 1 hour. After fixation, phalloidin was used to stain F-actin fibers, and DAPI was used to stain cell nuclei. Cells were imaged using an AxioScope (Zeiss) and the NIS-Elements imaging software, and 10 images of each condition were obtained and analyzed using the Fiji image processing package. Per image, the cell size of at least 26 cells was measured. **g** The CellTiter-Glo Cell Viability Assay was performed after SEMA3A-Fc treatment of isolated LSECs to determine the amount of ATP present ($n = 3$ independent LSEC isolations). In all graphs data points, mean \pm s.e.m., and the p-values are presented.

5.2. SEMA3A-mediated defenestration: mechanism of action

5.2.1. SEMA3A decreases fenestrae frequency in a time- and concentration-dependent manner

A distinct feature of LSECs are fenestrae, small holes which are organized in sieve plates and thought to facilitate the bi-directional exchange of molecules and lipids between the hepatocytes and the bloodstream^{263,264}. The loss of fenestrae is an early hallmark of liver diseases such as MASLD and may disrupt the lipid metabolism^{67,80,82}. SEMA3A is a class 3 semaphorin, known to induce the collapse of neurons amongst other things, however, recent experiments by Daniel Eberhard indicate that SEMA3A may also play a role the defenestration of LSECs.

To further investigate this, we aimed to evaluate the effect of SEMA3A over time as well as increasing SEMA3A concentrations on LSEC morphology. To this end, LSECs were isolated from C57BL/6J mice and allowed to grow for 4 hours. Following, LSECs were starved and then treated with 0.5, 1 or 2 $\mu\text{g/ml}$ of SEMA3A-Fc or IgG2a-Fc for 1 hour, whereas the amount of total protein given was kept constant (2 $\mu\text{g/ml}$). Further, they were treated with 1 $\mu\text{g/ml}$ SEMA3A-Fc or IgG2a-Fc for 30, 60 and 90 minutes, whereas the amount of total protein given was kept constant (1 $\mu\text{g/ml}$). Subsequently, the cells were prepared for SEM analysis (**Figure 13a**). Analysis shows that with increasing SEMA3A-Fc concentrations, the fenestrae frequency (*av.* 1.991 μm^{-2} vs 0.534 μm^{-2} , $p = 0.0101$, **Figure 13c**) and LSEC porosity (*av.* 5.019% vs 1.682%, $p = 0.0024$, **Figure 13d**) decreased significantly. Meanwhile, the fenestrae diameter remained unchanged, except for fenestrae being slightly larger after treatment with 1 $\mu\text{g/ml}$ SEMA3A-Fc compared to the control (*av.* 172.6 nm vs 194.5 nm, $p = 0.0422$, **Figure 13e**). Further, after 30 minutes SEMA3A-Fc did not have a visible effect on fenestrae frequency or cell porosity, however, after 60 minutes the fenestrae frequency (*av.* 2.072 μm^{-2} vs 0.690 μm^{-2} , $p = 0.0131$, **Figure 13f**) and LSEC porosity (*av.* 7.036% vs 2.113%, $p = 0.0002$, **Figure 13g**) were significantly decreased. However, after additional 30 minutes (90 min total), the effects were not more pronounced as there was no significant difference in both fenestrae frequency and LSEC porosity between cells incubated for 60 minutes and 90 minutes. The fenestrae diameter remained constant throughout all conditions.

In summary, SEMA3A-Fc reduces LSEC fenestrations in a time- and concentration-dependent manner.

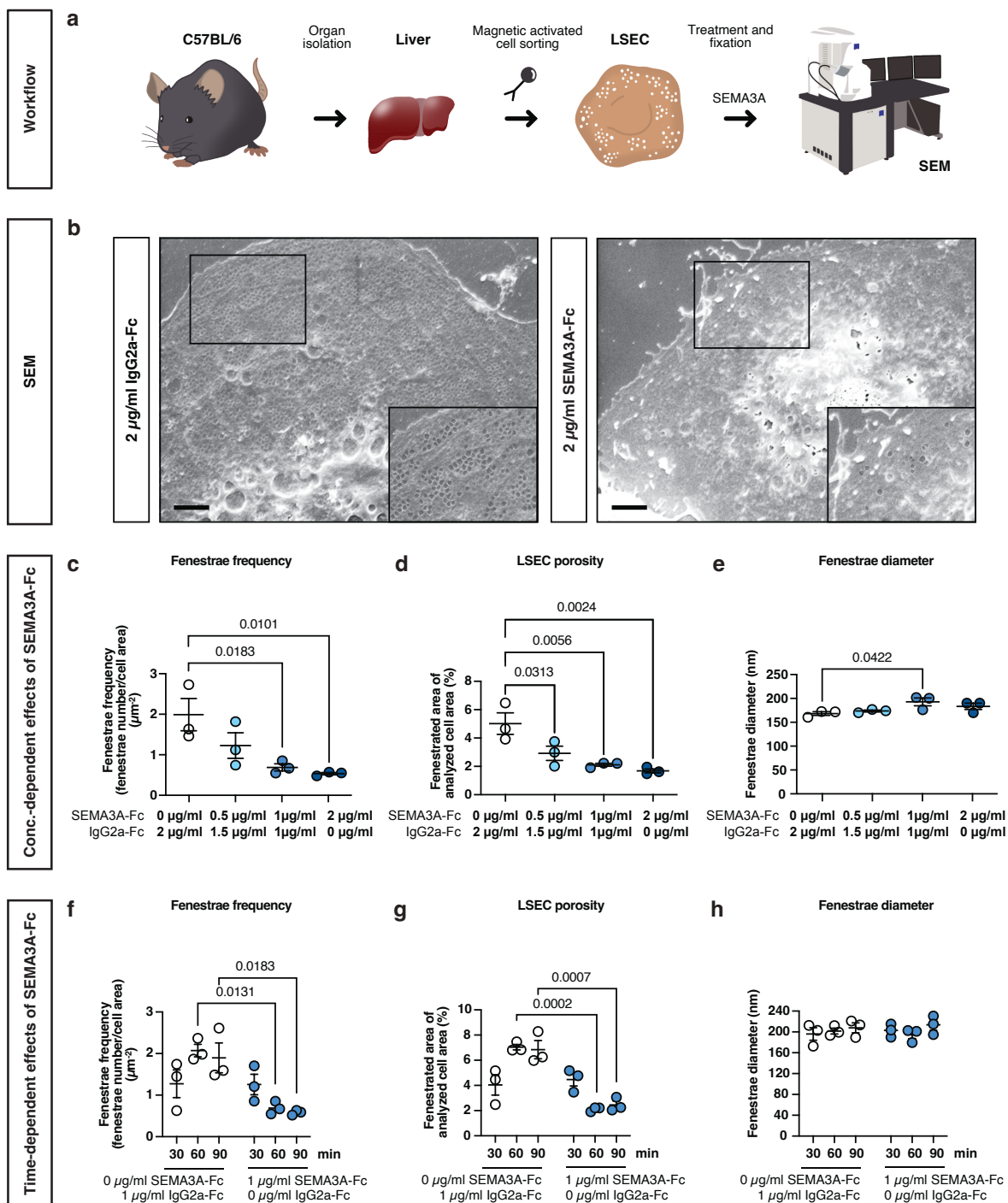


Figure 13. SEMA3A defenestrates LSECs in a concentration- and time-dependent manner.

a General workflow for LSEC experiments. Illustrations by Sydney Balkenhol. **b** SEM images of LSECs treated for 1 hour with SEMA3A-Fc and/or IgG2a-Fc. Brightness and contrast have been adjusted to enhance visibility. The fenestrae were colored with a digital charcoal pencil for better visualization. Scale bars, 2 μm . **c-d** Analysis of fenestrae frequency (c), LSEC porosity (d), and fenestrae diameter (e) of LSECs treated for 1 hour with SEMA3A-Fc and/or IgG2a-Fc concentrations as indicated ($n = 3$ independent LSEC isolations). The 1 $\mu\text{g/ml}$ SEMA3A-Fc values are from the experiment shown below. **f-h** Analysis of fenestrae frequency (f), diameter (g) and LSEC porosity (h) of LSECs treated with 1 $\mu\text{g/ml}$ SEMA3A-Fc or IgG2a-Fc for 30, 60 or 90 min ($n = 3$ independent LSEC isolations). For statistical analysis a two-tailed paired Student's *t*-test was performed in b, a one-way ANOVA with multiple comparisons (Dunnnett's *post hoc* test) in (c-e), and a two-way ANOVA with multiple comparisons (Tukey's *post hoc* test) in (f-h). For each condition, at least 5 images (taken from different LSECs) per experiment were analysed. In all graphs data points, mean \pm s.e.m. and the *p*-values are presented.

5.2.2. Inhibiting the SEMA3A subdomain of NRP1 ameliorates SEMA3A-induced defenestration in LSECs

Neuropilin-1 (NRP1) is a known receptor of SEMA3A; however, it has not yet been investigated whether it is needed specifically for SEMA3A-induced defenestration in mouse LSECs. To answer that question, we utilized three different blocking antibodies. Those antibodies specifically inhibit binding to the SEMA3A binding domain (NRP1^{SEMA3A}), the VEGF binding domain (NRP1^{VEGF}), or both subdomains of NRP1 (NRP1^{Pan}, **Figure 14a**) and were employed to test whether the effect of SEMA3A on fenestrae can be abrogated by preventing its interaction with NRP1.

Hence, isolated mouse LSECs were cultured for 4 hours, simultaneously starved and incubated with the above-mentioned antibodies for 1 hour, and then treated with 2 µg/ml of SEMA3A-Fc or IgG2a-Fc (control) for 1 hour. Afterwards, cells were prepared for SEM imaging and analysed using the previously described DLW. Results show, that upon only inhibiting the VEGF binding domain of NRP1, SEMA3A-Fc resulted in a significant decrease of both fenestrae frequency (*av.* 1.231 µm⁻² vs 0.549 µm⁻², *p* = 0.0062, **Figure 14c**) and LSEC porosity (*av.* 3.95% vs 1.79%, *p* = 0.0006, **Figure 14d**), while the fenestrae diameter remained unchanged (**Figure 14e**). Inhibition of either the SEMA3A binding domain or both subdomains eliminated the defenestrating effect of SEMA3A-Fc as the fenestrae frequency was not altered and LSEC porosity was increased (*av.* 3.404% vs 4.631%, *p* = 0.0348, **Figure 14d**). The fenestrae diameter remained unchanged (**Figure 14e**).

To summarize our findings, SEMA3A-Fc-induced defenestration appears to rely on the binding of SEMA3A to NRP1.

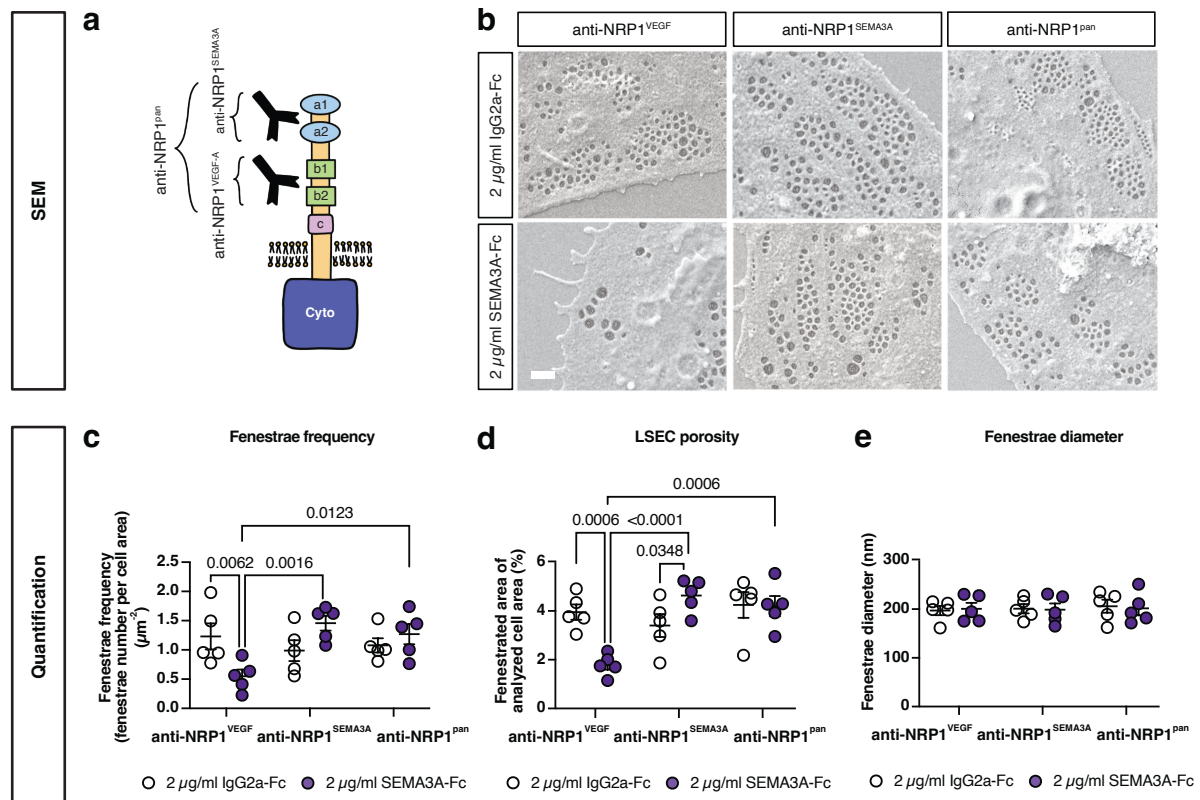


Figure 14. Inhibiting the SEMA3A subdomain of NRP1 ameliorates SEMA3A-induced defenestration in mouse LSECs.

a Schematic illustration of the NRP1 receptor and the binding sites of the anti-NRP1^{VEGF}, anti-NRP1^{SEMA3A} or anti-NRP1^{pan} antibodies. Illustrated by Sydney Balkenhol, inspired by Pan et al.²²³ **b** SEM images of LSECs first treated with anti-NRP1^{VEGF}, anti-NRP1^{SEMA3A} or anti-NRP1^{pan} for 1 hour and subsequently with either SEMA3A-Fc or IgG2a-Fc for 1 hour. Brightness and contrast have been adjusted to enhance visibility. The fenestrae were colored with a digital charcoal pencil for better visualization. Scale bar = 500 nm. **c-e**, Analysis of fenestration frequency (**c**), LSEC porosity (**d**), and fenestration diameter (**e**) of LSECs that were first treated with either anti-NRP1^{VEGF}, anti-NRP1^{SEMA3A} or anti-NRP1^{pan} for 1 hour, and subsequently treated with either SEMA3A-Fc or IgG2a-Fc for 1 hour. For statistical analysis a two-way ANOVA with multiple comparisons (Tukey's *post hoc* test) was performed. For each condition, at least five images (taken from different LSECs) were analyzed per experiment (n = 5 independent LSEC isolations). In all graphs data points, mean ± s.e.m., and the p-values are presented.

5.2.3. Kinase activity profiling of SEMA3A downstream signalling in LSEC

After showing that NRP1 is essential for SEMA3A-induced defenestration in LSECs (**Figure 14**), we performed kinase activity profiling (KAP) in order to get a more in-depth understanding of how SEMA3A affects fenestrations and thus the actin-cytoskeleton. To this end, we isolated mouse LSECs and performed a KAP of IgG2a-Fc *versus* SEMA3A-Fc treated LSECs measuring overall kinase activity of 196 protein tyrosine kinases (PTKs) and 144 serine-threonine kinases (STKs) using the PamChip® technology. Here, sample lysates are applied onto a porous membrane containing immobilized phosphorylation sites (hence referred to as phosphosites) on its surface. Those phosphosites are peptide representations of kinase targets/substrates. If those phosphosites are phosphorylated, a fluorescent antibody can bind to the phosphosite and a signal can be detected which is used to analyse

kinase activity. The analysis of the samples and statistical evaluation was performed solely by PamGene.

A heatmap shows that SEMA3A-Fc treatment generally resulted in higher kinase activity (**Figure 15a**) and a PCA (principal component analysis) identified the control condition of biological replicate 4 as an outlier which was therefore excluded from further analysis (**Figure 15b**). An MTvC (multiple treatment *versus* control) volcano plot identified 31 kinase targets via *t*-test which were differentially phosphorylated after SEMA3A treatment (**Figure 15c**). Of those 31 kinase targets, the most interesting ones regarding actin-dynamics were CREB1 (cAMP response element-binding protein), NF κ B (nuclear factor kappa b), TY3H (tyrosine 3-monooxygenase), CAC1C (Voltage-dependent L-type calcium channel subunit alpha-1C), and M-CSF (Macrophage colony-stimulating factor 1 receptor)^{95,265-270}. Subsequently, an upstream kinase analysis (UKA) was performed to predict which kinases were most likely responsible for the differential phosphorylation of the phosphosites. Identified kinases are presented in a CORAL kinome tree which shows that most kinases with a higher activity are from the AGC (protein kinase A, G, and C) kinase family²⁷¹. A total of 54 STKs belonging to different STK families were identified to be activated by SEMA3A (**Figure 15d**, Supplementary Table 1, Supplementary Table 2), whereas PTKs were largely unaffected. Of those STKs, several could be identified which can indirectly exert an effect on the actin cytoskeleton; PKC α (Protein kinase C alpha⁹⁵), PAK1 (p21 (RAC1) activated kinase 1²²¹), ROCK2 (rho-associated, coiled-coil-containing protein kinase 2²⁷²), Akt1 (RAC(Rho family)-alpha serine/threonine-protein kinase²⁷³), vasodilator-stimulated phosphoprotein (VASP)²⁷⁴, AMPK (5'-AMP-activated protein kinase catalytic subunit alpha-1²⁷⁵), IKK α/β (Inhibitor of nuclear factor kappa-B kinase subunit alpha/beta^{265,266}), and p70S6K β (Ribosomal protein S6 kinase beta-1²⁷⁶). ROCK2 and PAK1 are both known activators of LIMK1 (LIM domain kinase 1) which can affect the polymerization of actin through phosphorylation of cofilin-1^{277,278}.

In summary, SEMA3A-Fc results in the activation of multiple kinases of which several are known modulators of the actin-cytoskeleton.

alpha kinase group; Brd, bromodomain proteins; PDHK, pyruvate dehydrogenase kinase group; PIKK, phosphatidylinositol 3' kinase-related kinase group; RIO, RIO kinase group; TIF1, transcriptional intermediary factor 1. (a-c) were provided by PamGene, (d) was made using the CORAL web application².

5.2.4. Cofilin-1 phosphorylation is increased upon SEMA3A treatment

The kinase activity profiling revealed that two direct activators of LIMK1, a kinase which catalyses the phosphorylation of cofilin-1 at the serine3 residue, were activated by SEMA3A-Fc (**Figure 16a**). Cofilin-1 has been reported to depolymerise F-actin and to contribute to a dynamic actin-cytoskeleton, however, upon phosphorylation cofilin-1 is inactivated²²¹. Here, we investigated whether SEMA3A-Fc results in an increase of phosphorylated cofilin-1 (p-S3-cofilin-1) in relation to total cofilin-1 and whether this event can be repressed by LIMK1 inhibition.

To this end, isolated mouse LSECs were starved and pre-treated with either DMSO or LIMKi 3, a potent LIMK1 inhibitor²⁷⁹. Next, cells were treated with 1 µg/ml of SEMA3A-Fc or IgG2a-Fc for 1 hour before harvesting protein and performing western blot analysis. The results show that upon SEMA3A-Fc treatment, the p-S3-cofilin-1 to cofilin-1 ratio was tendentially increased (*av. 1.023 vs 1.237, $p = 0.073$, **Figure 16b***). If, however, the cells were pre-treated with LIMKi 3, the p-S3-cofilin-1 to cofilin-1 ratio returned below the base level and was significantly lower compared to both the SEMA3A-Fc and control conditions (*av. 1.237 vs 0.643, $p = 0.0354$; 1.023 vs 0.643, $p = 0.0387$, **Figure 16b***).

To conclude, SEMA3A-Fc appears to increase the phosphorylation of cofilin-1 through activation of LIMK1.

² <http://phanstiel-lab.med.unc.edu/CORAL/>

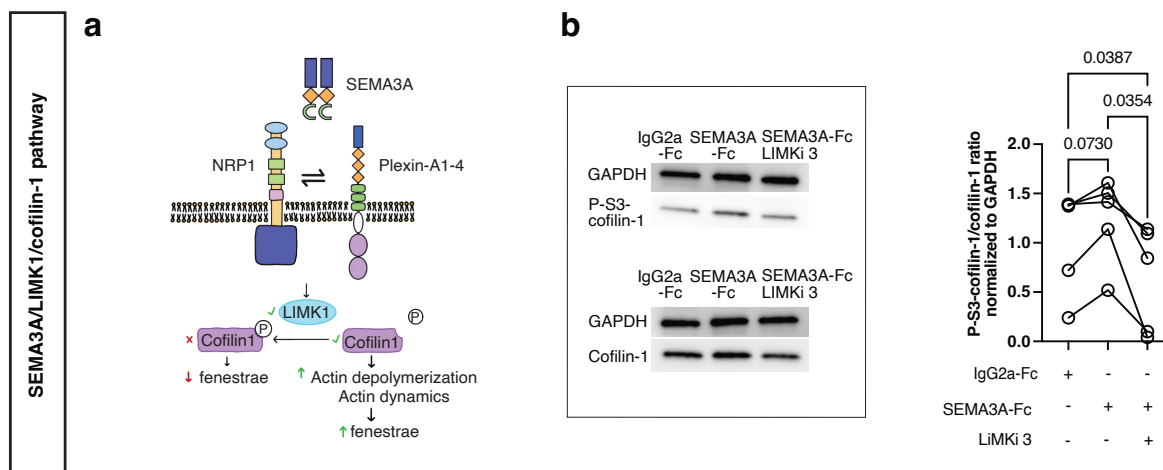


Figure 16. SEMA3A/LIMK1/cofilin-1 pathway.

a Schematic illustration of SEMA3A signaling through NRP1 and plexins. Upon SEMA3A binding to NRP1, NRP1 forms a holoreceptor complex with a plexin which acts as the signal transducing unit. Through a signaling cascade, LIMK1 is activated which catalyzes the phosphorylation of cofilin-1. Cofilin-1 is an actin depolymerization factor which is deactivated upon phosphorylation at its serine3 (S3). Thus, less actin is depolymerized, resulting in a less dynamic actin-network, and subsequently, fewer fenestrae. Illustrated by Sydney Balkenhol. **b** Western blots of mouse LSEC protein lysates (n = 5 independent LSEC isolations). LSECs were pretreated with either DMSO or LIMKi 3, a LIMK1 inhibitor, and then treated with either SEMA3A-Fc or IgG2a-Fc. For the analysis, cofilin-1 and p-S3-cofilin-1 were normalized to GAPDH and then put into relation of each other (p-S3-cofilin-1 to cofilin-1). For statistical analysis a one-way ANOVA with multiple comparisons (Tukey's *post hoc* test) was performed. In the graph data points and p-values are presented.

5.2.5. LIMK1 inhibition impedes SEMA3A-induced defenestration in mouse LSECs

After showing that SEMA3A-Fc promotes phosphorylation of cofilin-1 through activation of LIMK1 (**Figure 16**), we were now interested whether inhibition of LIMK1 and therefore amelioration of SEMA3A-induced cofilin-1 phosphorylation would protect LSECs from SEMA3A-induced defenestration. For this purpose, MACS-isolated mouse LSECs were cultured for 4 hours and starved and pre-treated with either DMSO or LIMKi 3, a potent LIMK1 inhibitor for 1 hour. Next, cells were treated with 1 $\mu\text{g}/\text{ml}$ of SEMA3A-Fc or IgG2a-Fc for 1 hour before cells were prepared for SEM imaging and analysed using the previously described DLW.

As to be seen in **Figure 17a** treatment with SEMA3A-Fc resulted in the appearance of less fenestrations, while pre-treatment with LIMKi 3 abrogated that effect. Analysis of SEM images revealed a significant decrease of both fenestrae frequency (*av.* $1.937 \mu\text{m}^{-2}$ vs $0.795 \mu\text{m}^{-2}$, $p = 0.0017$, **Figure 17b**) and LSEC porosity (*av.* 6.22% vs 2.607% , $p = 0.0352$, **Figure 17c**) upon SEMA3A-Fc treatment, which could be prevented by LIMKi 3 pre-treatment. While fenestrae frequency was significantly increased in SEMA3A-Fc and LIMKi 3-treated cells (*av.* $0.795 \mu\text{m}^{-2}$ vs $1.677 \mu\text{m}^{-2}$, $p = 0.0104$, **Figure 17b**), LSEC porosity was only

numerically higher compared to the SEMA3A-treated cells (*av.* 2.607% vs 4.859%, $p = 0.2163$, **Figure 17c**). The fenestrae diameter remained unchanged throughout all conditions (**Figure 17d**).

In conclusion, inhibition of LIMK1 can, to a certain extent, protect mouse LSECs from SEMA3A-induced defenestration.

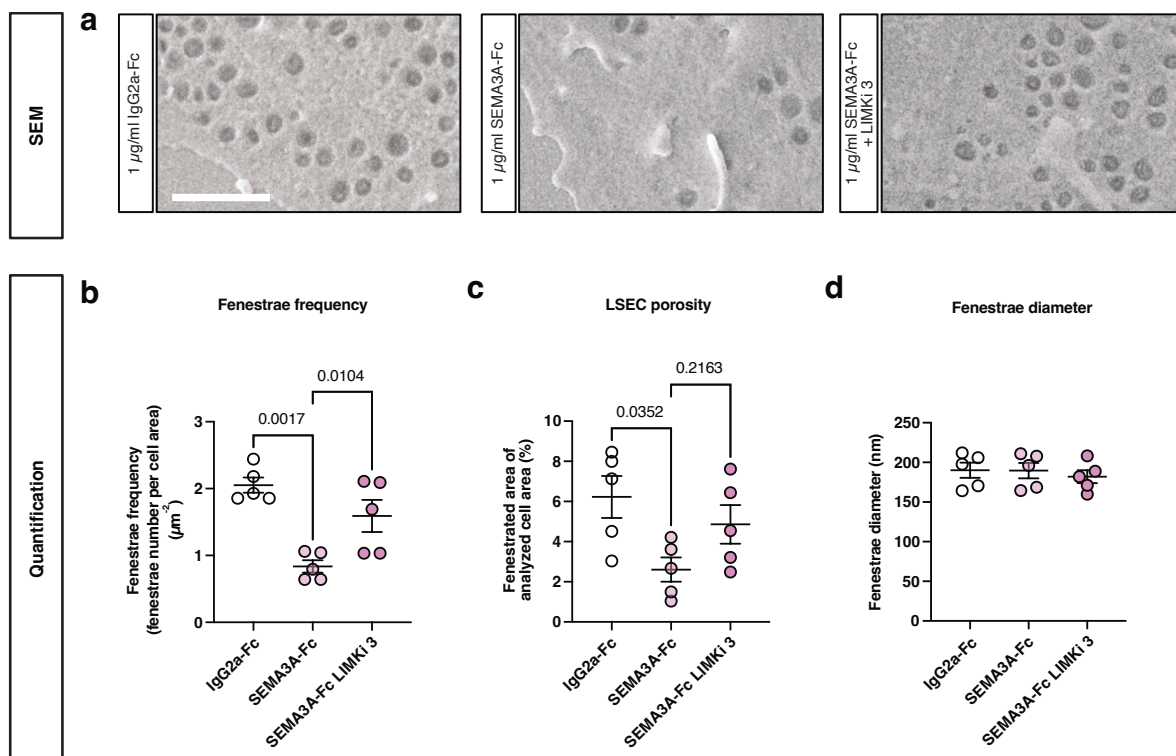


Figure 17. LIMK1 activity is required for SEMA3A-induced defenestration of mouse LSECs.

a SEM images of mouse LSECs pretreated with either DMSO or LIMKi 3 and then treated with either SEMA3A-Fc or IgG2a-Fc. The fenestrae were colorized with a digital charcoal pencil for better visualization. Scale bar, 1 = μm . Brightness and contrast have been adjusted to enhance visibility. **b-d** Analyses of fenestrae frequency (**b**), LSEC porosity (**c**), and fenestrae diameter (**d**) of mouse LSECs pretreated with LIMKi 3 or DMSO and subsequently treated with SEMA3A-Fc or IgG2a-Fc. For each condition, 10 images (taken from different LSECs) were analyzed ($n = 5$ LSEC isolations). For statistical analysis, a one-way ANOVA with multiple comparisons (Tukey's *post hoc* test) was performed. In all graphs data points, mean \pm s.e.m., and the p-values are presented.

5.2.6. Palmitic acid and SEMA3A affect the actin-cytoskeleton in LSECs

Circulating levels of palmitic acid, a saturated fatty acid, have been found to correlate with a lower fenestrae frequency and porosity in mouse LSECs¹⁰². Since fenestrae are highly dependent on the cytoskeleton and specifically the actin-cytoskeleton, we were interested in whether palmitic acid would result in an altered appearance of the actin-cytoskeleton in human LSECs. Further, we wanted to investigate the effect of palmitic acid treatment on SEMA3A expression, and the effect of SEMA3A itself on the F-actin network in mouse LSECs.

Hence, human LSECs were treated with 0.75 mM palmitic acid and BSA (control) for 24 hours and subsequently, their F-actin fibres were analysed using laser scanning microscopy (LSM) and the F-/G-actin ratio was measured. This ratio reflects to a certain extent how dynamic the actin-network is, whereas more F-actin points to more actin-polymerisation. For this, the G-actin / F-actin *In Vivo* Assay Kit from Cytoskeleton Inc. was utilized. Further, human LSECs were treated with 0.5 mM palmitic acid for 2, 6, 18, and 24 hours after which RT-qPCR was performed. Lastly, MACS-isolated mouse LSECs were cultured for 4 hours, starved for 1 hour, and treated with 2 µg/ml of either SEMA3A-Fc or IgG2a-Fc (control). Subsequently, the F-/G-actin ratio was measured as aforementioned.

Results show that upon palmitic acid treatment there was a visible increase of F-actin stress fibres in human LSECs which resulted in a significantly higher fluorescence of phalloidin-stained F-actin compared to the BSA-treated control (*av.* 1.548×10^6 vs 2.830×10^6 , $p = 0.0101$, **Figure 18a, b**). This was also reflected in the F-/G-actin ratio, which was tendentially higher after palmitic acid treatment compared to the control, and on average increased by 69% (*av.* 0.169 vs 0.286 , $p = 0.059$, **Figure 18c**,). Upon palmitic acid treatment, the relative *SEMA3A* transcript abundance was significantly increased after both 18 and 24 hours compared to the control (*av.* 0.974 vs 1.994 , $p = 0.0006$; 0.974 vs 3.748 , $p = 0.0001$, **Figure 18d**). Lastly, in mouse LSECs, treatment with SEMA3A-Fc resulted on average in a significant 46% increase of the F-/G-actin ratio ($p = 0.0407$, **Figure 18e**). It should be noted that upon the control treatment (IgG2a-Fc) each sample presented with a double band which could not be explained (Supplementary Figure 1). For the analysis, only the band at the same height as the standard was used for the analysis. Additionally, the lysates from one mouse presented with protein concentrations that were outside of the standard curve and were therefore excluded for further analysis (Supplementary Figure 1), while the rest of the lysates had sufficient protein quantities.

To conclude, treatment of human LSECs with palmitic acid results in increased stress fibre formation and increased *SEMA3A* expression while treatment of mouse LSECs with SEMA3A-Fc results in a significant increase of the F-/G-actin ratio.

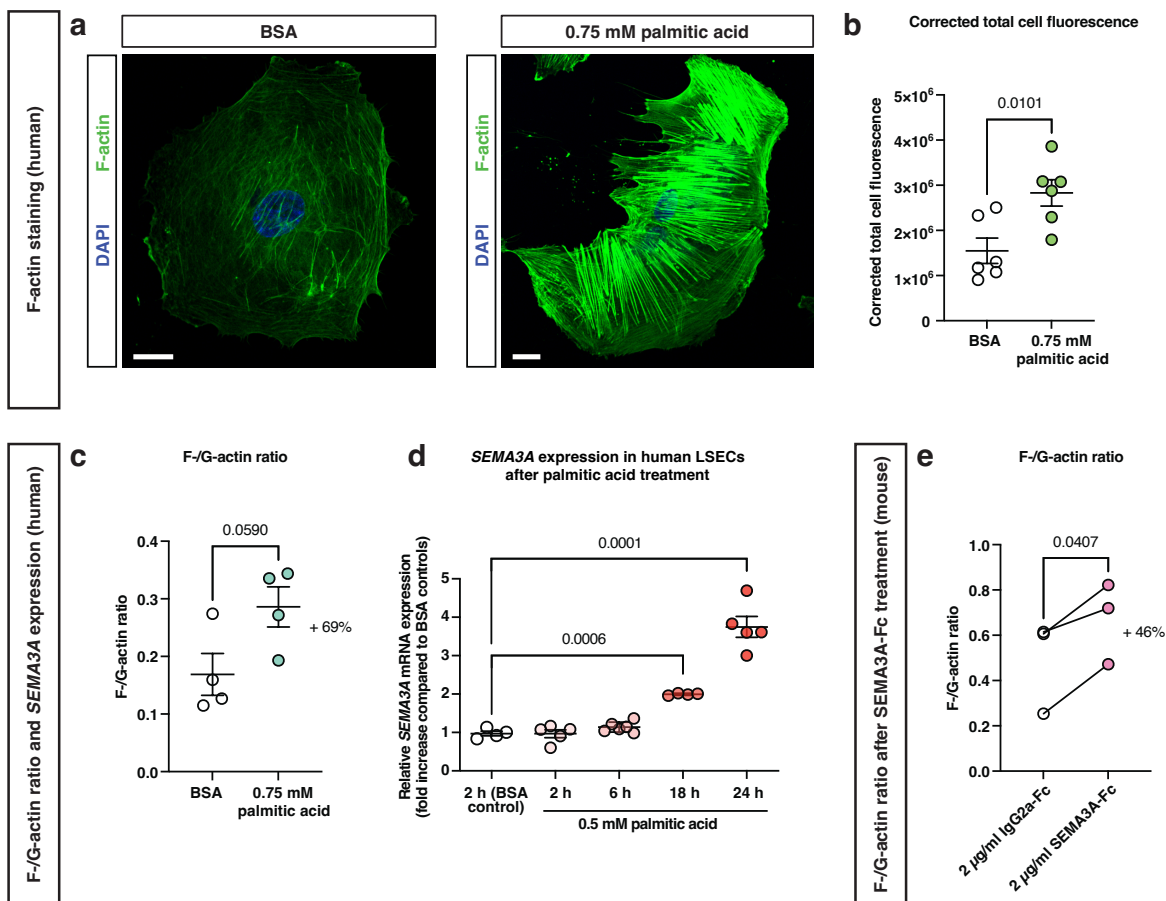


Figure 18. Effects of palmitic acid and SEMA3A-Fc on the actin-cytoskeleton in human and mouse LSECs.

a Phalloidin staining of human LSECs (52 years old, male donor: QC-12B15F11) treated with BSA or 0.75 mM palmitic acid for 24 h, scale bars = 20 µm. Cell nuclei were stained with DAPI. Brightness and contrast have been adjusted to enhance visibility. Images were taken with a Zeiss LSM 780. **b** Densitometric quantification of actin fluorescence. A two-tailed unequal variances *t*-test was used to test for statistical significance, *n* = 6 images of 1 cell culture experiment. **c** F-/G-actin ratio of human LSECs treated with either BSA or 0.75 mM palmitic acid for 24 hours as assessed by the G-actin / F-actin *In Vivo* Assay Kit from Cytoskeleton Inc. For statistical analysis, a two-tailed unequal variances *t*-test was performed. *n* = 4 wells of 1 cell culture experiment. **d** Relative SEMA3A expression in primary human LSECs after 2 (*n* = 5 wells), 6 (*n* = 6 wells), 18 (*n* = 4 wells), and 24 hours (*n* = 5 wells) after 0.5 mM palmitic acid treatment *versus* a 2-hour BSA treatment (*n* = 4 wells). A one-way ANOVA with Dunnett's *post hoc* test was used to test for statistical significance. **e** F-/G-actin ratio of mouse LSECs treated with 2 µg/ml of either IgG2a-Fc or SEMA3A-Fc for 1 hour as assessed by the G-actin / F-actin *In Vivo* Assay Kit. For statistical analysis, a paired Student's *t*-test was performed, *n* = 3 mice in 1 independent experiment were analyzed. The treatment of human LSECs in (a) was performed by Dr. Daniel Eberhard. The data and the underlying experiments in (d) were obtained from and performed by Daniel Eberhard and Andrea Köster. In all graphs, data points, mean ± s.e.m. (except for e) and the *p*-values are presented.

5.3. The role of *Sema3a* in the development of MASLD

5.3.1. Male *db/db* mice present with reduced LSEC fenestrations and porosity

Db/db mice are a frequently used mouse model for hepatic steatosis, despite being more commonly used for/associated with T2D²⁸⁰. *Db/db* mice develop steatosis, with a NAS (non-alcoholic fatty liver disease activity score) of 3-4, at an age of 12 weeks²⁸⁰. To the best of our knowledge, no one has yet investigated fenestrae in *db/db* mice, and we were therefore interested whether male and/or female *db/db* mice have less fenestrae compared to *db/+* mice and might thus be a suitable mouse model for MASLD-induced LSEC defenestration. Additionally, foregoing experiments have revealed that in LSECs from 12-week-old *db/db* mice *Sema3a* expression is significantly increased (Supplementary Figure 6).

To this end, the livers of 10-week-old male *db/db* and *db/+* mice, and 9 to 11-week-old female *db/db* and *db/+* mice, were perfused and analysed with SEM and a WEKA classifier/Fiji regarding their fenestrae number and size. The analysis revealed a numerically lower fenestrae frequency (av. $9.712 \mu\text{m}^{-2}$ vs $8.248 \mu\text{m}^{-2}$, $p = 0.4609$, **Figure 19b**), LSEC porosity (av. 6.435% vs 5.099% , $p = 0.3025$, **Figure 19c**) and fenestrae diameter (av. 118.1 nm vs 112.8 nm , $p = 0.3601$, **Figure 19d**) in female *db/db* mice compared to *db/+* mice. We also noticed the appearance of several small globular specimens in the sinusoids of female *db/db* mice, which may represent chylomicrons (**Figure 19a**). Male *db/db* mice on the other hand had a tendentially decreased fenestrae frequency compared to *db/+* mice (av. $23.87 \mu\text{m}^{-2}$ vs $19.46 \mu\text{m}^{-2}$, $p = 0.0739$, **Figure 20b**) and a significantly, 36% decreased LSEC porosity (av. 8.198% vs 5.269% , $p = 0.0066$, **Figure 20c**). Interestingly, their fenestrae diameter was also slightly decreased (av. 88.27 nm vs 78.19 nm , $p = 0.0756$, **Figure 20d**). Similar to the female *db/db* mice several small globular specimens were visible in the sinusoids of male *db/db* mice (**Figure 20a**). Furthermore, as expected, male *db/db* mice had significantly increased body weight (av. 25.78 g vs 45.34 g , $p = 0.0002$, **Figure 20e**) and blood glucose (av. 120.4 mg/dl vs 323.2 mg/dl , $p = 0.0002$, **Figure 20f**) compared to *db/+* mice. A correlation analysis showed that both weight and blood glucose strongly correlated with fenestrae frequency ($r = -0.62$, $p = 0.053$; $r = -0.48$, $p = 0.163$, **Figure 20g**) and diameter ($r = -0.60$, $p = 0.068$; $r = -0.76$, $p = 0.011$, **Figure 20g**), as well as LSEC porosity ($r = -0.85$, $p = 0.002$; $r = -0.83$, $p = 0.003$ **Figure 20g**). A PCA (principal component analysis) illustrates those effects as *db/db* and *db/+* mice form two distinct clusters (**Figure 20h**).

To conclude, male, but not female, *db/db* mice have significantly less and smaller fenestrae compared to *db/+* mice, which negatively correlates with their weight and blood glucose. Therefore, male *db/db* mice are an appropriate *in vivo* model for steatosis/MASLD-induced LSEC defenestration.

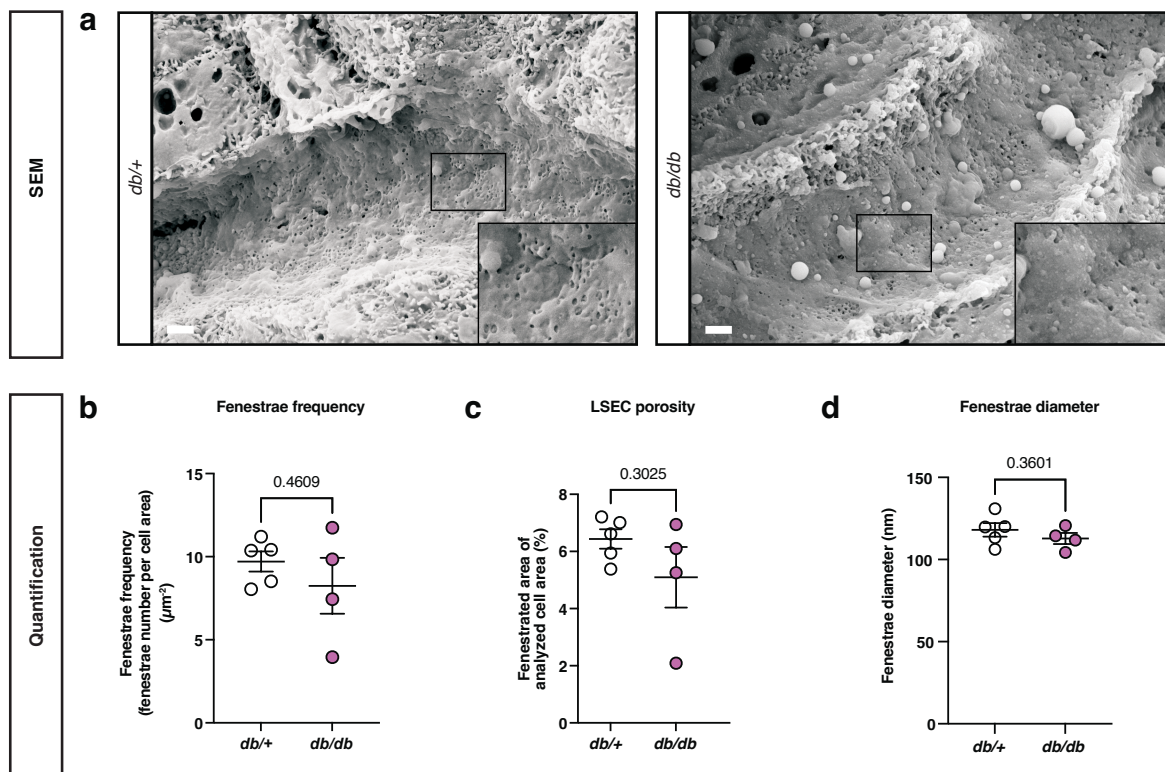


Figure 19. Female *db/db* mice present with numerically reduced fenestrations and porosity.

a SEM images from sinusoids of 9 to 11-week-old female *db/+* and *db/db* mice. Scale bars = 1 μm . **b-d** Analysis of liver sinusoids from female *db/+* and *db/db* mice, regarding their fenestrae frequency (**b**), LSEC porosity (**c**), and fenestrae diameter (**d**), $n = 5$ (*db/+*) and 4 (*db/db*). For statistical analysis a two-tailed unequal variances *t*-test was performed. In all graphs data points, mean \pm s.e.m., and the *p*-values are presented.

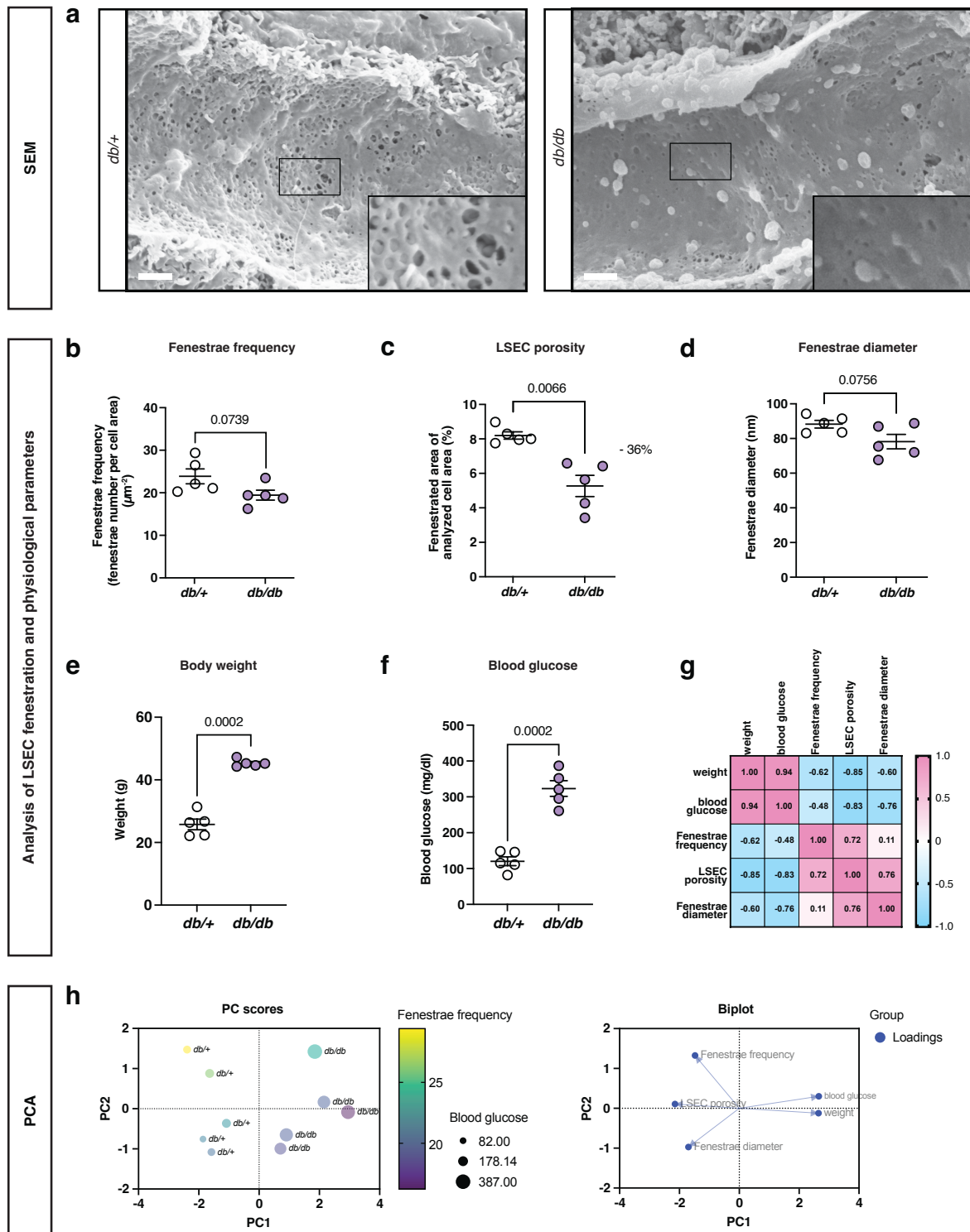


Figure 20. Male *db/db* mice present with reduced fenestrations and porosity.

a SEM images from sinusoids of 10-week-old male *db/+* and *db/db* mice. Scale bars = 1 μ m. **b-d** Analysis of liver sinusoids from *db/+* and *db/db* mice, regarding their fenestrae frequency (**b**), LSEC porosity (**c**), and fenestrae diameter (**d**). **e** Body weight and **f** blood glucose of *db/+* versus *db/db* mice ($n = 5$ mice/genotype). **g** Correlation matrix showing Pearson correlation coefficients for pairwise comparisons between the variables weight, blood glucose, fenestrae frequency and diameter, and LSEC porosity in the combined cohort of *db/db* and *db/+* mice. For statistical analyses in (**b-f**) a two-tailed unequal variances *t*-test was performed. In all graphs data points, mean \pm s.e.m., and the *p*-values are presented. **h** Principal component analysis of fenestrae frequency, fenestrae diameter, LSEC porosity, blood glucose, and body weight from *db/+* and *db/db* mice. PC scores and biplot are presented.

5.3.2. Blocking SEMA3A binding to NRP1 in *db/db* mice slightly affects hepatic steatosis

Since male *db/db* mice presented with decreased LSEC porosity (**Figure 20**) as well as increased *Sema3a* expression (Supplementary Figure 6), they are a suitable *in vivo* model for steatosis-induced LSEC defenestration. Here, we wanted to test the therapeutic value of SEMA3A inhibition regarding the reversal of defenestration and reduction of hepatic steatosis.

For that purpose, 10-week-old male *db/db* mice were treated with an antibody which is designed to specifically abrogate the binding of SEMA3A to NRP1 but not impede VEGF-A binding²²³. Mice received intravenous injections of the antibody or an IgG2a isotype control every third day for 16 days. Results show that at the end of week two, the NRP1^{SEMA3A}-treated mice weighed significantly less than the IgG2a-treated (control) mice (av. 48.03 g vs 42.93 g, 0.0271, **Figure 21a**), however, at day 16, there was only a tendential difference between the two groups (av. 46.67 g vs 43.14 g, $p = 0.0769$, **Figure 21a**). Despite the blood glucose of the NRP1^{SEMA3A}-treated mice always being numerically higher, there was no significant difference (**Figure 21b**). The liver-to-body weight ratio was numerically increased in the NRP1^{SEMA3A}-treated mice (av. 5.633% vs 5.851%, $p = 0.3187$, **Figure 21d**), while the kidney to body weight ratio was tendentially increased ($p = 0.0505$, Supplementary Figure 8) and the spleen to body weight ratio was tendentially decreased ($p = 0.0868$, Supplementary Figure 8). Upon investigating blood lipid parameters, NRP1^{SEMA3A}-treated mice had significantly more TGs (av. 0.878 mmol/l vs 1.380 mmol/l, $p = 0.0242$, **Figure 21e**) and numerically more non-esterized fatty acids (NEFA) (av. 1.16 mmol/l vs 1.37 mmol/l, $p = 0.2257$, **Figure 21j**) in their blood compared to the control mice, while cholesterol, high-density lipoprotein (HDL), AST, and ALT remained unchanged (**Figure 21f-i**). Analysis of TGs in the livers revealed slightly, yet not significantly less TGs in the livers of NRP1^{SEMA3A}-treated mice (av. 84.89 $\mu\text{M}/\text{mg}$ vs 65.40 $\mu\text{M}/\text{mg}$, $p = 0.2096$, **Figure 21k**). Lastly, densitometric quantification of ORO stainings of the liver showed numerically less lipids in the livers of NRP1^{SEMA3A}-treated mice (av. 0.224 vs 0.197, $p = 0.3167$, **Figure 21l**).

In total, short-term inhibition of SEMA3A binding to NRP1 in male *db/db* mice mildly, but not definitively, improved hepatic steatosis.

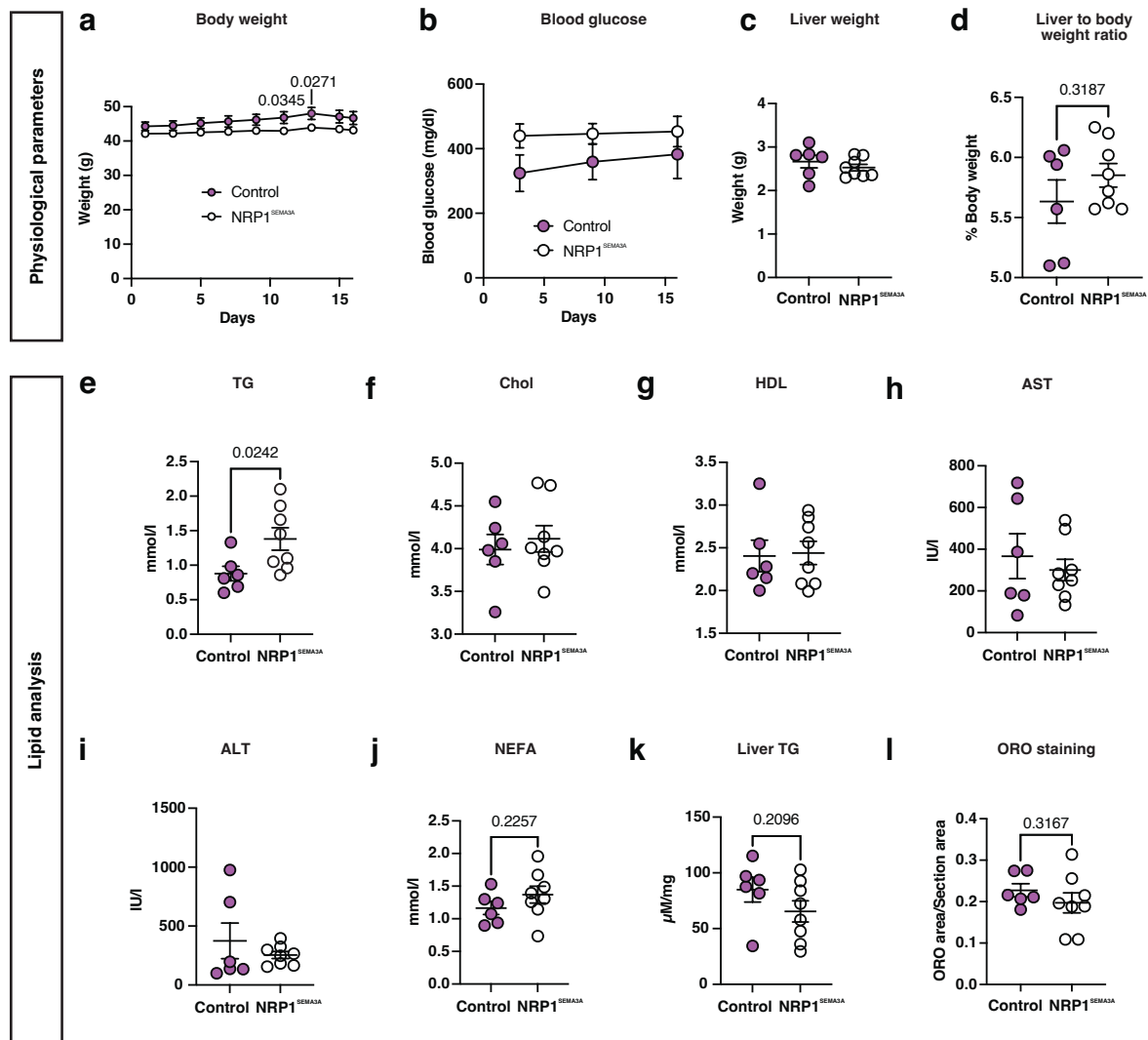


Figure 21. Blocking SEMA3A binding to NRP1 in *db/db* mildly affects hepatic steatosis.

a-d Body weight, blood glucose, liver weight, and liver to body weight ratio of male *db/db* mice ($n = 6-8$). **e-i** Serum transaminases and lipid profile of NRP1^{SEMA3A} or IgG2a (control) treated *db/db* mice, $n = 6$ (control) and $n = 8$ (NRP1^{SEMA3A}). **j** NEFA measurement ($n = 6-8$). **k** Biochemical liver triglyceride (TG) measurement ($n = 6$ (control) and 8 (NRP1^{SEMA3A})). **l** Densitometric quantification of liver ORO staining. In (a, b) multiple unpaired *t*-tests with a two-stage step-up method according to Benjamini, Krieger and Yekutieli was used to correct for multiple comparisons and to detect significant discoveries, in (c-l) an unequal variances *t*-test was performed for statistical analyses. The data and the underlying assays in j-l) were obtained from and performed by Daniel Eberhard. In all graphs data points, mean \pm s.e.m., and p-values are presented.

5.3.3. Endothelial cell-specific deletion of *Sema3a* reduces hepatic steatosis and affects LSEC fenestrae

Since short-term inhibition of SEMA3A downstream signalling via NRP1 did not have a meaningful therapeutic effect on steatosis, we resorted to the use of long-term, genetic intervention, by utilizing a tamoxifen-inducible, endothelial cell-specific, *Sema3a* knockout mouse model (hitherto referred to as *iEC^{Sema3a}*)²⁵⁷. For comparison, wildtype mice which also received tamoxifen (hitherto referred to as *iEC^{wt}*), were used. To induce hepatic

steatosis and DIO, both groups were given a high-fat diet (HFD) over the course of 20 weeks in total. Specifically, after 10 weeks of HFD, tamoxifen was administered for 5 days successively. Recombination efficiency was confirmed by PCR and gel electrophoresis²⁴⁷. Meanwhile, the body weight was assessed regularly, and after 8 weeks, a VLDL secretion assay was performed. Hence, we injected mice the lipoprotein lipase (LPL) inhibitor Triton WR1339 and measured TGs (as a proxy for VLDL) in the blood over time²⁸¹. Furthermore, a liver perfusion was performed to evaluate sinusoidal fenestration and a blood serum analysis to measure insulin, glucose, and free fatty acids (FFAs).

The weight data confirms DIO and, excluding the days where tamoxifen was administered, shows a steady increase in weight in both groups (**Figure 22a**). The *iEC^{Sema3a}* mice, however, gained weight considerably slower after tamoxifen was given throughout weeks 15 to 20 (**Figure 22a**). Further, after 20 weeks, *iEC^{Sema3a}* mice had a tendentially reduced liver weight (av. 2.187 g vs 1.530 g, $p = 0.0747$, **Figure 22b**) and liver-to-body weight ratio (av. 4.418% vs 3.610%, $p = 0.0826$, **Figure 22c**). The VLDL secretion assay at week 18 revealed a significantly slower release of VLDL from the liver into the bloodstream after 6 hours in *iEC^{wt}* compared to *iEC^{Sema3a}* mice (av. 364.1 mg/dl vs 593.9 mg/dl, $p = 0.0015$, **Figure 22d**). SEM analysis of liver sinusoids shows that *iEC^{Sema3a}* mice had tendentially 80% more (av. $6.96 \mu\text{m}^2$ vs $12.55 \mu\text{m}^2$, $p = 0.0808$, **Figure 22f**), yet smaller fenestrations than *iEC^{wt}* mice (av. 140.1 nm vs 109.2 nm, $p = 0.0564$, **Figure 22h**). Further, *iEC^{Sema3a}* mice had significantly decreased insulin levels (av. 6.058 ng/ml vs 3.318 ng/ml, $p = 0.0480$, **Figure 22i**) as well as a reduced HOMA-IR (av. 100 vs 57.64, $p = 0.1303$, **Figure 22j**) and Adipo-IR (av. 100 vs 40.15, $p = 0.0300$, **Figure 22k**). Correlation analysis reveals, similarly to *db/db* mice, a strong, negative correlation between weight and both fenestrae frequency ($r = -0.79$, $p = 0.007$, **Figure 22l**) and LSEC porosity ($r = -0.7$, $p = 0.023$, **Figure 22l**), while the fenestrae diameter correlated positively with weight ($r = +0.84$, $p = 0.002$, **Figure 22l**). Strikingly, weight and blood glucose did not correlate to each other ($r = +0.01$, **Figure 22l**), while the VLDL secretion after six hours correlated negatively with weight ($r = -0.48$, $p = 0.025$, **Figure 22l**) and positively with LSEC porosity ($r = +0.53$, $p = 0.115$, **Figure 22l**).

In summary, long-term genetic deletion of *Sema3a* in the setting of DIO shows a positive effect on weight and sinusoidal fenestrations, ultimately resulting in improved VLDL secretion.

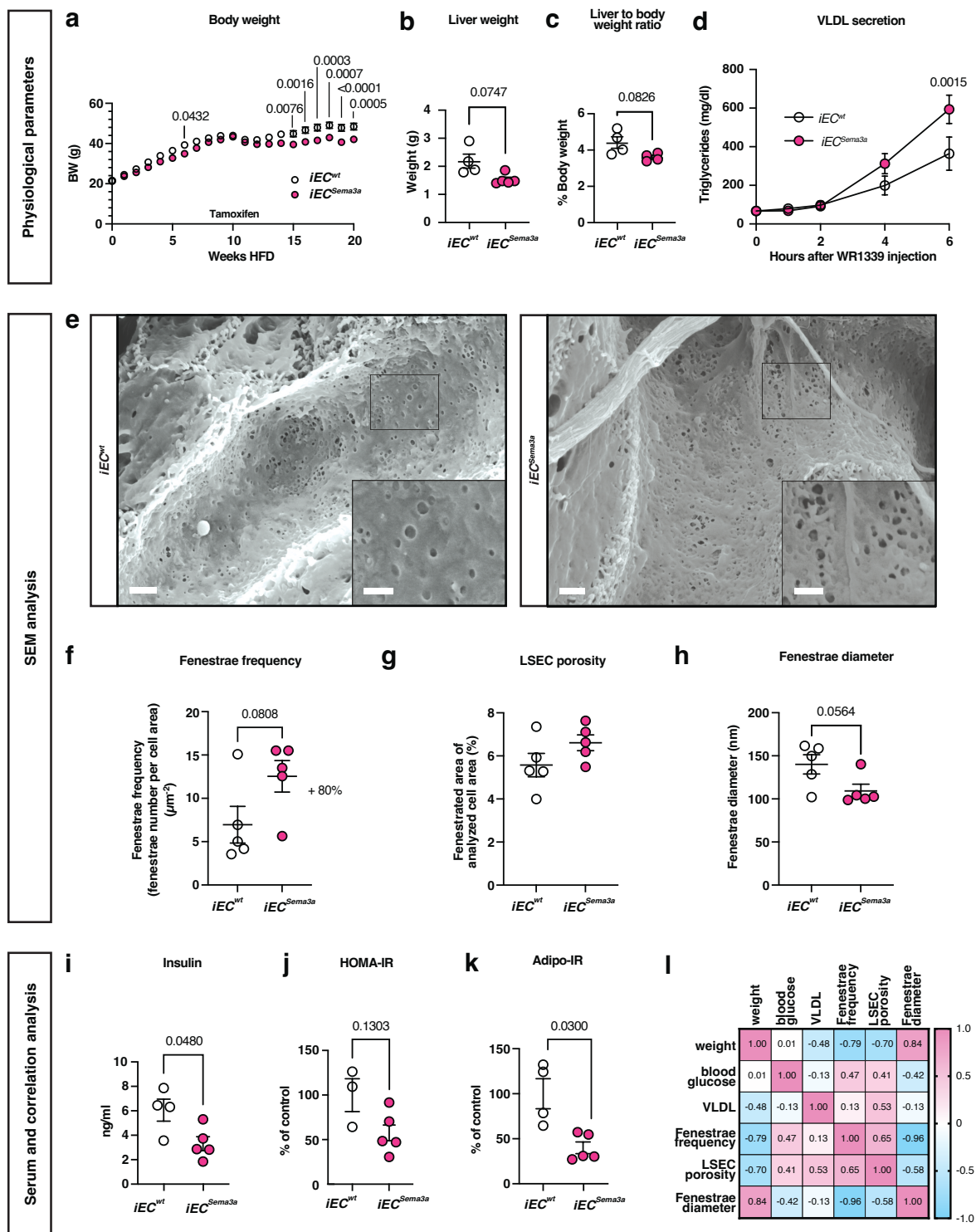


Figure 22. Lower hepatic fat content and increased fenestrations in DIO *iEC^{Sema3a}* mice compared to DIO *iEC^{wt}* mice. Analysis of *Cdh5-Cre^{ERT2} × Sema3a^{fl/fl}* (*iEC^{Sema3a}*) and *Cdh5-Cre^{ERT2}* (*iEC^{wt}*) mice kept on HFD for 20 weeks (with tamoxifen injections on 5 consecutive days after 10 weeks of HFD). **a** Body weight, $n = 12$ (*iEC^{wt}*) and 11 (*iEC^{Sema3a}*) mice, a repeated measures two-way ANOVA with a Sidak's *post hoc* test was used to test for statistical significance. **b** Liver weight, and **c** relative liver weight (% of BW), $n = 4$ (*iEC^{wt}*) and 5 (*iEC^{Sema3a}*) mice. For statistical analysis in (b-c) two-tailed unequal variances *t*-tests were performed. **d** Measurement of VLDL (TG) secretion after injection of WR1339 ($n = 12$ (*iEC^{wt}*) and 11 (*iEC^{Sema3a}*) mice), after 18 weeks HFD (8 weeks after *Sema3a* deletion by tamoxifen). For statistical analysis a two-way repeated measurements ANOVA with Sidak's *post hoc* test was performed. **e-h** SEM analysis of liver sinusoids from *iEC^{wt}* and *iEC^{Sema3a}* mice, regarding their fenestrae frequency (f), LSEC porosity (g), and fenestrae diameter (h). Scale bars = 1 µm (large images) and 500 nm (inlays). For statistical analysis an unequal variances *t*-test was performed. **i** Serum insulin,

n = 4 (*iEC^{wt}*) and 5 (*iEC^{Sema3a}*). j HOMA-IR, n = 3 (*iEC^{wt}*) and 5 (*iEC^{Sema3a}*). k Adipo-IR, n = 4 (*iEC^{wt}*) and 5 (*iEC^{Sema3a}*). For statistical analysis in (i-k) a two-tailed unequal variances *t*-test was performed. l Correlation matrix showing Pearson correlation coefficients for pairwise comparisons between the variables body weight, blood glucose, VLDL secretion at hour 6, fenestrae frequency and diameter, and LSEC porosity. In all graphs data points, mean \pm s.e.m., and the p-values are presented. The data and the underlying experiments in a-d, i-k were obtained from and performed by Daniel Eberhard.

6. Discussion

The aim of this thesis was to investigate the role of SEMA3A in LSEC defenestration and the potential impact on the progression and manifestation of hepatic steatosis. *In vitro*, we were able to show that MACS is a reliable method to isolate fenestrated LSECs without magnetic beads interfering with subsequent quantification of fenestrae (**Figure 10**). In order to simplify the quantification of fenestrae, we developed a deep learning workflow which allows us to count and measure fenestrae in an unbiased and quick manner (**Figure 11**), and were able to show that culture dependent loss of fenestration occurs after 24 hours (**Figure 12**). While short-term SEMA3A-treatment did not alter cell size or ATP-levels (**Figure 12**), we were able to demonstrate that it decreases fenestrae in a concentration- and time-dependent manner (**Figure 13**). Regarding the mechanism of action, we identified NRP1 as the main receptor of SEMA3A in LSECs (**Figure 14**), and, by using kinase activity profiling, found several differentially active kinases which can affect the actin cytoskeleton (**Figure 15**), specifically, PAK1 and ROCK2. Both can activate LIMK1, a kinase which phosphorylates and thus inactivates cofilin-1, an actin depolymerisation factor. To confirm involvement of cofilin-1, we performed western blot analysis and found that SEMA3A induces cofilin-1 phosphorylation (**Figure 16**), a process which could be ameliorated by LIMK1 inhibition. Additionally, LIMK1 inhibition abrogated SEMA3A-induced defenestration in mouse LSECs (**Figure 17**). Treatment of human LSECs with palmitic acid showed visible effects on the F-actin cytoskeleton, i.e. an increase of the F-/G-actin ratio (**Figure 18**). Moreover, palmitic acid induced *SEMA3A* transcription in human LSECs, and SEMA3A itself was able to increase the F-/G-actin ratio in mouse LSECs (**Figure 18**).

In vivo, we demonstrated the suitability of male *db/db* mice as a viable model for defenestration in the setting of early hepatic steatosis as those mice presented with a reduced fenestrae frequency and LSEC porosity (**Figure 19, Figure 20**). Lastly, short-term inhibition of SEMA3A binding to NRP1 in *db/db* mice affected hepatic steatosis mildly, but not significantly (**Figure 21**), while long-term genetic intervention via inducible, endothelial cell-specific deletion of *Sema3a* in DIO mice resulted in reduced macrovesicular steatosis and body weight, as well as an increase of VLDL secretion and LSEC fenestration (**Figure 22**). Thus, this study reveals how SEMA3A, saturated fatty acids, and DIO induce changes in the LSEC phenotype by manipulation of the F-actin cytoskeleton, i.e. loss of fenestrae, and

highlights the positive effect of SEMA3A inhibition/*Sema3a* ablation on LSEC fenestration in the setting of early MASLD (**Figure 23**).

6.1. LSEC and fenestrae: establishment of quality and analysis

6.1.1. MACS isolation yields viable LSECs with satisfactory purity

Magnetic-activated cell sorting (MACS) is an established method to isolate a specific cell type using antibodies coupled to magnetic beads. Here, we show that it yields viable, and thus fenestrated, LSECs without resulting in an excessive number of magnetic beads on the LSEC surface which might interfere with subsequent fenestrae quantification (**Figure 10**). It should be mentioned that we can only speculate about which structures specifically are magnetic beads, since we were unable to do any tests which would undeniably confirm or deny their presence. We merely searched for specimen which fit the size (as given by the manufacturer) of magnetic beads and were not part of the cells and/or cellular debris. Further, despite a combination of antibodies for separation and depletion having been shown to yield a purer LSEC population, the method we used, only employing CD146, still yielded viable and fenestrated LSECs, and is a commonly used method resulting in both a high yield and purity²⁸². In comparison to *in vivo* measurements, MACS has been shown to result in a larger fenestrae diameter in *in vitro* cultured LSECs, however, since we only employed MACS to isolate LSECs, this would be a constant in our experiments^{87,283}.

In summary, the MACS method yields fenestrated LSECs with little contamination of magnetic beads and is therefore the appropriate method for our experiments.

6.1.2. The deep learning workflow identifies and analyses fenestrae with a high accuracy

In order to simplify the quantification of fenestrae and also increase the speed of the analysis, we developed a deep learning workflow (DLW) which is able to identify and measure fenestrae (**Figure 11**). The analysis with the DLW is significantly quicker than manual analysis, e.g. one image with 1,000 fenestrae would approximately take 15 minutes manually, whereas the DLW can analyse up to 45 images in the same time period. Thus, this tool allows us to execute more experiments/conditions since the time of analysis is not a limiting factor anymore. Further, the analysis is unbiased, while manual analysis is

performed differently from person to person and can therefore generate inconsistent results. It is noteworthy, however, that in order to do an analysis with this tool in the aforementioned period of time, access to a supercomputer, i.e. a computer with a high-level of performance, is advantageous. While normal laptops and PC usually have the computing power of $1 \cdot 10^{11}$ FLOPS (floating-point operations per second), supercomputers can perform up to $1 \cdot 10^{18}$ FLOPS²⁸⁴. Furthermore, despite the relatively high accuracy, this tool can certainly be improved via new training data, possibly allowing for a more precise identification of fenestrations. Research has shown that next to the number of data sets, the quality in terms of representativeness of the samples is also important, meaning in this case that increasing the number of sample images of LSECs with different numbers, shapes, and sizes of fenestrae will most likely improve the accuracy of the DLW²⁸⁵. Furthermore, recent advantages regarding artificial intelligence, together with the rapid increase of deep neural networks, might help to develop improved, automated analysis-methods in the near future²⁸⁶. It also should be noted that in order to analyse fenestrae with this tool, the images should be taken with a similar resolution and quality, since this tool was trained with images of a certain resolution. Using images with a lower quality/resolution, even though made with the same SEM, can result in faulty identification of fenestrae.

Besides, we were not the first to use machine learning for fenestrae identification as in 2021 Szafranska et al. already compared the Ilastik software, a machine learning tool, against the manual analysis of fenestrae²⁸³. They found that despite a good correlation between both types of analysis ($R^2 = 0.89$ for LSEC porosity, and $R^2 = 0.63$ for fenestrae frequency), the tool was unable to distinguish between some non-transmembrane protrusions in the cell membrane and smaller fenestrae²⁸³.

This fast and unbiased tool, which can be of great use for researchers in the field of fenestrations, represents an important development as it allows to perform high-throughput experiments which are not limited by the time required for the analysis. It also shows that neural networks are a promising tool for a more efficient image analysis.

6.1.3. MACS-isolated LSECs retain their size and do not lose fenestrae during short-termed experiments

For transferability, human LSECs are the preferred option for cell culture experiments, however, primary human LSECs lose their fenestrations rapidly after isolation, making cell culture-based fenestrae research in human LSECs not very accessible (personal communication with Daniel Eberhard). Further, access to primary human LSECs from cadaveric livers is limited by the availability of human ischemic sensitivity and organ accessibility²⁸⁷. Despite the availability of several human liver endothelial cell lines, only one, i.e. SK Hep1, presents with fenestrae and sieve plates upon VEGF-A treatment according to Cogger et al.²⁸⁸. However, the passages analysed in our lab did not respond to VEGF-A treatment and showed a low number of fenestrae (data not shown). We therefore decided to use primary mouse LSECs for our *in vitro* experiments.

Culture dependent loss of fenestration is a known phenomenon in primary LSECs which we were able to show not yet having taken place during the time frame (1-2 hours) of our experiments (**Figure 12**)⁹⁵. The result that LSECs lose their fenestrae after 24 hours falls in line with previous research which found a more than 60% decrease of LSEC porosity after 24 hours and a more than 90% decrease after 48 hours²⁶².

Since in primary mouse LSECs the cell porosity and fenestrae frequency correlate with the cell area, cell contraction might influence and falsify the results of experiments. As SEMA3A has been shown to increase vascular permeability through the destabilisation of VE-cadherin, which in turn can result in endothelial cell shrinkage, it was important to investigate whether cells would contract during a 1-hour treatment^{200,240}. The analysis reveals no significant changes in cell size, regardless of whether cells were treated with the lower or the higher concentration of SEMA3A-Fc (**Figure 12**). Consequently, it is unlikely that the treatment with SEMA3A-Fc will affect downstream analysis of fenestrae frequency and LSEC porosity or its interpretation. In comparison to COS-7 cells and human umbilical vein-derived endothelial cells (HUVECs), LSECs appear to be less susceptible to SEMA3A-induced cell contraction, as previous studies have found both HUVECs and COS-7 cells to shrink after a 1-hour treatment, however, in one case a slightly higher quantity of SEMA3A was used^{289,290}.

Lastly, we evaluated the effect of SEMA3A on LSEC viability by performing the CellTiter-Glo Assay which is based on the premise that the amount of ATP present in cells is an indicator of metabolically active and therefore viable cells²⁹¹. ATP is crucial for LSECs to uphold their fenestrae, so we wanted to explore the possibility whether SEMA3A can alter fenestrations via changing ATP levels^{91,292}. Results show that treatment with SEMA3A-Fc does not have any visible impact on intracellular ATP levels (**Figure 12**), however, since the amount of ATP in a cell naturally fluctuates, the CellTiter-Glo Assay may not be a very sensitive method as it only quantifies the amount of ATP present in the cells at the moment the assay was performed. Nevertheless, it might give a first indication whether cell viability or mitochondrial activity is severely diminished. For a more in-depth evaluation of the effect of SEMA3A on cell viability a cell death assay, e.g. measuring caspase-3 activity or a terminal deoxynucleotidyl transferase dUTP nick end labelling (TUNEL) assay should be performed. Due to the easy availability of primary mouse LSECs and their fenestrated phenotype, they currently present the best option for the development of LSEC-based therapies. As our experiments are short-termed, culture dependent loss of fenestrations, cell shrinkage or reduced intracellular ATP-levels are not likely to interfere with analysis of fenestrae.

6.2. SEMA3A and fenestrae: mechanism of action

6.2.1. LSEC porosity and fenestrae frequency negatively correlate with SEMA3A concentrations

In the hepatic sinusoids fenestrae are thought to be important for the bi-directional exchange of molecules and lipids between the hepatocytes and the bloodstream²⁶³. Their loss is an early event in liver diseases such as MASLD which may disrupt the lipid metabolism^{67,102,264}. SEMA3A is known to have several physiological functions, however, recent experiments by Daniel Eberhard indicate that SEMA3A may also play a role in the development of MASLD by affecting LSEC fenestrae²¹². Here, we show that LSEC porosity and fenestrae frequency negatively correlate with SEMA3A concentrations, while the fenestrae diameter is barely affected (**Figure 13**).

As the downstream effects of SEMA3A require between 30 and 60 minutes to trigger the closing of fenestrae, it is plausible to assume that SEMA3A does not directly trigger

defenestration, but rather activates downstream pathways, which may even alter gene expression. Furthermore, the fenestrae diameter was unchanged, which might be surprising, as when fenestrae are closing, their diameter will decrease, however, fenestrae are extremely dynamic structures and the closing of one fenestra can take as little as two minutes^{76,97}. STED microscopy might help to understand how SEMA3A impacts fenestrae dynamics as it allows for high resolution live cell imaging⁹⁸. Another possibility would be atomic force microscopy which would also allow for a real-time assessment of the process of defenestration initiated by SEMA3A^{76,97}. The latter was first discovered in the context of collapsing growth cones of neurons, where it results in actin-depolymerization¹⁹⁶. Since fenestrae are surrounded by a ring of actin and myosin, it seems plausible to assume that SEMA3A might reduce fenestrae via actin-depolymerisation²⁰. However, experiments by Steffan et al., using actin-depolymerisation agents such as cytochalasin B, have shown that depolymerisation or disruption of actin fibres lead to an increase of fenestrations, not a decrease²⁹³.

Our experiments show, that SEMA3A is able to regulate fenestrations of LSECs, and thus, indirectly, might affect the bi-directional exchange of lipids between hepatocytes and the bloodstream. Since defenestration has been suggested to be an early event in several liver diseases, including MASLD, further research regarding the process of defenestration might be beneficial regarding novel therapeutical approaches^{67,264,294}.

6.2.2. NRP1 is required for SEMA3A-induced defenestration in mouse LSECs

Semaphorins can bind to several receptors such as NRP1/2, integrins, and plexins, whereas SEMA3A is known to bind to NRP1, which forms a holo-receptor complex with a plexin, the latter acting as the signal-transducing unit²⁰⁹. Our results show that binding of SEMA3A to the SEMA3A binding domain but not the VEGF binding domain of NRP1 is crucial for the defenestrating effect of SEMA3A-Fc (**Figure 14**).

VEGF-A and SEMA3A are known competitors, and apparently have an antagonistic effect on fenestrae via NRP1. *In vitro* VEGF-A has been shown to increase fenestrae number and size, while we were able to show that SEMA3A reduces fenestrations⁹⁵. Further, disruption of VEGF-A signalling in mice was found to reduce fenestration, while in heterozygous *Sema3a* knock-out mice fenestrations were found to be increased^{247,295}. Due to the architecture of

the receptor-complex and the necessary interaction between NRP1 and plexin-A1-4 it is unlikely that NRP1 can simultaneously transfer a VEGF signal as binding to VEGFR2 is required²⁹⁶. Nonetheless, VEGF might still exert an effect solely through binding to VEGFR2, yet, as this is technically possible in all the tested conditions, it should not impair the results²⁹⁷.

Despite the possibility of SEMA3A acting independently of NRP1, the level of protection via inhibition of the SEMA3A binding domain suggests that NRP1 is most likely responsible for the majority of the phenotype. This is supported by previous research, which shows that SEMA3A mediates its effects through NRP1 in several other physiological systems^{231,244,298}. Despite NRP2 also being expressed in endothelial cells, the specificity of the antibodies used have been confirmed by Pan et al., making it highly unlikely that the observed effects are due to blocking NRP2^{223,299}. Further, several publications state that SEMA3A does not bind to NRP2^{300,301}.

These findings highlight NRP1 as a possible target for inhibiting SEMA3A-induced defenestration, as it might have an ameliorating effect towards early stages of MASLD.

6.2.3. Several kinases involved in actin-dynamics are activated by SEMA3A in mouse LSECs

In order to get insights into the intracellular actions of SEMA3A downstream of NRP1 we performed kinase activity profiling (KAP). Here, lysates from LSECs which were treated with either SEMA3A-Fc or IgG2a-Fc for 10 minutes were analysed using the PamChip technology from PamGene. We chose this incubation period since another KAP, where the incubation period was 60 minutes, did not yield any definite results. We speculated that this time point might represent the phenotypical changes in LSEC fenestrations, however, since we were more interested in the initial changes in kinase activity triggered by SEMA3A, we decided on this shorter incubation period.

Results show the differential phosphorylation of 31 phosphosites and 54 kinases (**Figure 15**). Here, we identify several kinase substrates, as represented by the phosphosites, whose phosphorylation can be associated with contraction of the actin-network and indirectly smaller/less fenestrae. One is TY3H, an enzyme that catalyzes the rate-limiting step of L-tyrosine to L-DOPA, the precursor for dopamine and epinephrine³⁰². Both dopamine and epinephrine have been shown to result in a contraction of sinusoids and possibly

fenestrations³⁰³⁻³⁰⁵. CAC1C on the other hand is a subunit of the voltage dependent calcium channel Cav1.2 which results in Ca²⁺ influx, and as a consequence a contractile force, decreasing fenestrae size⁹⁵. Interestingly, during acute hyperglycaemia and diabetes, phosphorylation of Cav1.2 by protein kinase A (PKA) has been found to be increased in the arteries of diabetic patients and stimulate vasoconstriction in mice²⁶⁸. Lastly, the p50 subunit of NFκB was also phosphorylated, which is required for efficient DNA-binding³⁰⁶. NFκB plays an important role in fibrosis promotion, subtly linking SEMA3A-induced defenestration and progression of MASH to fibrosis, highlighting the known connection between LSEC capillarization and its promotion of liver disease/fibrosis^{95,265,266,307}.

Looking at the results of the upstream kinase analysis, two kinases were of particular interest, i.e. ROCK2 and PAK1, since those are direct activators of LIMK1^{221,272,277,278}. LIMK1 has already been shown to be activated by SEMA3A in neurons and human endothelial cells, and catalyses the phosphorylation of cofilin-1, which is an actin depolymerization molecule^{221,278,308}. Upon phosphorylation cofilin-1 is inactivated, which can lead to an increased F-/G-actin ratio, a state that has been connected with a decrease in fenestration^{97,309}. Further, several kinases could be identified which can indirectly affect the actin-network; PKCα⁹⁵ and PKG^{310,311} which can induce a contractile force via activation of MLCK^{95,312} and VASP²⁷⁴, respectively, Akt1^{266,313}, which via IKKα/β^{265,266} can induce NFκB signaling and presumably loss of fenestrae^{266,314}, AMPK²⁷⁵ which can induce caveolin degradation, promoting defenestration²⁷⁵, and lastly p70S6Kβ²⁷⁶ which can inhibit cofilin-1-induced actin depolymerization. For a better visualization, we created a hypothesized pathway (**Figure 23**). Interestingly, Creeden et al. showed that several of the mentioned kinases, such as Akt, PKCα, PKG, and p70S6Kβ, were also significantly upregulated in fibrosis in both mice and humans³¹⁵. This suggests a certain congruency of activated pathways between SEMA3A downstream signaling and signaling in the setting of liver injury.

As expected, SEMA3A triggers a measurable change in kinase activity downstream of NRP1, however, although we analysed three independent experiments, individual pathways should be validated in autonomous experiments. Nevertheless, the results give a first glance of which pathways may be involved. In our case, i.e. SEMA3A signalling downstream of NRP1, our most promising target appears to be LIMK1, as two kinases which can activate LIMK1 were significantly more active upon SEMA3A treatment.

To conclude, results from the KAP point to LIMK1 and cofilin-1 as promising downstream targets for our subsequent experiments, where we focused on the role of LIMK1 in SEMA3A-induced defenestration of LSECs.

6.2.4. LIMK1 and cofilin-1 phosphorylation are required for SEMA3A-induced defenestration

Due to the results of the KAP, we were interested whether SEMA3A increases cofilin-1 phosphorylation in LSECs via LIMK1. Analysis reveals a tendentially increased ratio of p-S3-cofilin-1 to cofilin-1 upon SEMA3A treatment, an effect which is completely abrogated upon LIMK1 inhibition (**Figure 16**). Additionally, SEM analysis reveals that inhibition of LIMK1 prevents SEMA3A-induced defenestration (**Figure 17**). This strongly suggests that part of the effect of SEMA3A on fenestrae is due to cofilin-1 phosphorylation via NRP1 and LIMK1, presenting two novel therapeutic targets for improving fenestrations in a pathological setting. Recently, astaxanthin, a xanthophyll carotenoid, has been shown to improve oxidative stress and inflammation in the setting of MASLD which was, among many factors, due to cofilin-1 downregulation^{316,317}. Increased cofilin-1 phosphorylation might however not explain the effect of SEMA3A to its full extent since the increase was not very prominent, yet this increase was measured 60 minutes after SEMA3A treatment. A shorter treatment period as used in the setting of the KAP might show a stronger increase. Aizawa et al. found that cofilin-1 phosphorylation was highest after a 5-minute SEMA3A treatment in mouse dorsal root ganglia (DRG) which also express *Nrp1* and *Plexin*²²¹.

It is also noteworthy that LIMK1 does not only exert an effect on the cytoskeleton via cofilin-1 but has also been found to induce microtubule destabilization in HUVECs, a process which is associated with actin stress fibre formation and cell contraction^{308,318}. Nevertheless, recalling the KAP results, LIMK1 is not the only differentially activate kinase upon SEMA3A treatment, leaving room for a number of alternative pathways working in congruency. Further exploration those possibilities may pave the way towards a better understanding of the mechanism of defenestration and conversely fenestrae formation.

6.2.5. Palmitic acid and SEMA3A affect actin-dynamics by increasing the F-/G-actin ratio

In the setting of high levels of palmitic acid, the number and size of fenestrae, structures which are highly dependable on the cytoskeleton, have previously been found to be decreased¹⁰². We were therefore interested as to whether palmitic acid would result in an altered appearance of the actin-network and *SEMA3A* mRNA expression in human LSECs. Results show that palmitic acid causes in a significant visual and statistical increase of F-actin fibres and the F-/G-actin ratio with a concomitant increase of *SEMA3A* expression after 24 hours (**Figure 18**). This suggests that palmitic acid can stimulate *SEMA3A* expression, pointing towards the activation of a lipid-regulated transcription factor that can bind to the *SEMA3A* transcription promoter. Further, it shows a clear modulation of the actin cytoskeleton, which might have been caused by the increased *SEMA3A* mRNA levels or another protein whose transcription was stimulated/increased by palmitic acid (**Figure 18**). In intestinal cells e.g. both 25 and 100 μ M of palmitic acid resulted in a significant increase of actin after a 24-hour incubation³¹⁹. Here, they found the F-actin-uncapping protein LRRC16A to be downregulated upon palmitic acid treatment which would result in decreased actin polymerization³¹⁹. *SEMA3A* on the other hand has been known to exert an effect on the cytoskeleton since its original discovery as collapsin²¹⁸. During growth cone collapse in neurons *SEMA3A* specifically acts through modulation of actin^{201,218}. Additionally, in 2001, Aizawa et al. found that *SEMA3A* can act through LIMK1 and cofilin-1, whereas cofilin-1 can directly influence the actin-cytoskeletal dynamics²²¹. In order to test the particular effect of *SEMA3A*-Fc on F-actin in mouse LSECs, the F-/G-actin ratio was measured, showing a significant increase after 1 hour (**Figure 18**). Comparing the average percental increase of the F-/G-actin ratio, it is of no surprise that after 24 hours there was a 50% higher increase than after 1 hour, however, if we presume a gradual increase, *SEMA3A* resulted in a much quicker response than palmitic acid. Conversely, if the effect of palmitic acid is due to increased *SEMA3A* expression, which is only significantly upregulated after 18 hours, it seems sensible that the amount of F-actin is not increased significantly more. Increased levels of F-actin versus G-actin, i.e. the presence of actin stress fibres, have been shown to influence fenestrae diameter and LSEC porosity, pointing to modulation of the cytoskeleton being a major part of the mechanism behind *SEMA3A*-induced defenestration^{97,309}. In the pathological setting of obesity, T2D, and MASLD, *SEMA3A* might

therefore link hyperlipidaemia, i.e. high levels of saturated fatty acids, with capillarization of hepatic sinusoids.

In summary, palmitic acid can induce *SEMA3A* transcription and increase stress fibres, while *SEMA3A* on its own can increase the F-/G-actin ratio, pointing towards the re-organization of the cytoskeleton playing an important role in *SEMA3A*-induced defenestration.

6.3. The role of *Sema3a* in the development of MASLD

6.3.1. Male *db/db* mice are a suitable model for capillarization in early stages of MASLD

Db/db mice are homozygous for a mutation in the leptin receptor and a widely used mouse model for T2D, obesity, and MASLD³²⁰. Here, we show that *Sema3a* expression is significantly increased in LSECs of *db/db* mice compared to their respective controls (Supplementary Figure 6). This puts *Sema3a* expression into the context of high glucose, high insulin, and steatosis and further supports the hypothesis that *SEMA3A* presents a link between hyperlipidemia and LSEC capillarization. Previous studies have already found *Sema3a* expression to be upregulated in cirrhotic rat LSECs, whereas a human cohort study found an increased *SEMA3A* expression in MASLD patients, which decreased with the stage of fibrosis^{242,321}. Further, in healthy individuals, *SEMA3A* was reduced in the blood serum for 24 hours after induction of hypoglycemia while T2D patients failed to regulate *SEMA3A* levels, suggesting a constantly high concentration³²².

Additionally, SEM analysis shows a significantly decreased LSEC porosity in male *db/db* mice, while female mice only have a numerically lower LSEC porosity (**Figure 19, Figure 20**). Dietary models such as the HFD and choline-deficient, L-amino acid-defined (CDAA)-diet have also been found to significantly decrease fenestrations, however, these studies did not evaluate *Sema3a* expression²⁶⁴. This presents male *db/db* mice as the first suitable genetic model for defenestration in the setting of early MASLD and also links increased *Sema3a* expression with reduced LSEC fenestrations. *SEMA3A* inhibition/*Sema3a* deletion in LSECs might therefore present a viable therapeutic option to ameliorate the severity of hepatic steatosis. It also suggests that *SEMA3A* most likely acts in an autocrine manner, since healthy hepatocytes lack the obligatory *SEMA3A* receptors, i.e. NRP1 and plexins, and are therefore not directly influenced by LSEC-derived *SEMA3A*³²³.

Despite female *db/db* mice at a relatively young age not presenting with significant phenotypical changes in their sinusoids, they might be of interest in combination with a chemically induced menopause, since studies have shown that estrogen protects women from MASLD, however, that severity increases post menopause^{324,325}. It is also possible that older female *db/db* mice would have been a more appropriate choice, as estrogen slows disease progression and thus changes in the sinusoid may only become evident at a later timepoint^{326,327}. The importance of gender-specific treatment options has become more evident in the past decade with many publications pointing to significant differences in the progression and susceptibility of several diseases such as cancer, cardiovascular diseases and metabolic diseases, and specifically MASLD regarding prevalence and mortality risk³²⁸⁻³³². Interestingly, female mice presented with a lower fenestrae frequency than male mice, however, they also had larger fenestrae. The finding of sex-specific differences in the morphology of hepatic sinusoids should be confirmed by repetition of both experiments where the perfusion is done successively.

To conclude, *Sema3a* is increased in LSECs of *db/db* mice, which, together with human studies, points towards a de-regulation of SEMA3A in the setting of T2D. Further, we present male *db/db* mice as a suitable model for capillarization in early stages of MASLD, while female *db/db* mice might be of interest at an older age or in combination with a chemically induced menopause.

6.3.2. Blocking SEMA3A binding to NRP1 in *db/db* mice might have a therapeutical value in the context of MASLD

One important question we wanted to answer is whether inhibition of SEMA3A, or SEMA3A signalling, holds a therapeutical value towards hepatic steatosis. In order to test this, we employed the same SEMA3A binding domain specific NRP1 antibody (NRP1^{SEMA3A}) as used in our *in vitro* experiments (**Figure 14**). Short-term NRP1^{SEMA3A} treatment had no major effects on cholesterol, ALT, AST, HDL, and NEFA, and resulted in a mild reduction of liver TGs and significantly increased blood TGs (**Figure 21**). This suggests that short-term inhibition of SEMA3A signalling has a mildly, yet non-significantly, ameliorating effect on hepatic steatosis. Ideally, this experiment would have been performed for at least 4 weeks, which might have shown more clear differences in the measured parameters, however, this was

not possible due to a limited amount of antibody available. Unfortunately, we were unable to examine the hepatic sinusoids of NRP1^{SEMA3A}-treated mice and can therefore only speculate whether inhibiting SEMA3A signalling resulted in more and/or larger fenestrae. The heightened TG levels in the blood and the numerically decreased amount of TGs in the liver, however, suggest that the secretion of VLDL particles into the bloodstream might have been enhanced.

Furthermore, regarding the liver TGs, a high standard deviation in both groups contributed to a non-significant outcome, as one control mouse had noticeably fewer hepatic TGs compared to the rest of the group, while in the NRP1^{SEMA3A}-treated group, some mice were more affected than others. Still, five out of the eight NRP1-treated mice had lower hepatic TGs than the majority of the control mice. Besides, the blood TGs were significantly increased, suggesting that inhibition of NRP1-facilitated SEMA3A-signalling resulted in the metabolization of lipids in other organs than the liver. It should also be kept in mind that we used *db/db* mice, thus a mouse model with a multifactorial phenotype. Therefore, the progression of T2D and other comorbidities experienced by this mouse model might have had an opposing influence on the effect of NRP1 inhibition in the liver.

Even though the effect was not significant, it is noteworthy that the livers of the NRP1^{SEMA3A}-treated group slightly grew in size (**Figure 21**). One explanation might be that VEGF-A could still bind to NRP1 while SEMA3A could not, virtually changing the ratio of available VEGF-A to SEMA3A. Increased VEGF-A binding may therefore result in growth of the liver, which is supported by the fact that treatment with VEGF-A can result in an increased liver to body weight ratio³³³. Furthermore, Bachelder et al. have shown that the ratio rather than the concentrations of VEGF-A and SEMA3A are important for the subsequent cellular reaction²²⁷. Since the antibody we employed did not only inhibit SEMA3A binding in the liver, adverse effects would have been possible in tissues which also express NRP1. In the bone marrow, for example, SEMA3A is an important factor which, presumably via NRP1, promotes bone regeneration, while in the kidneys it promotes diabetic nephropathy and renal fibrosis, both long-term complications/comorbidities of T2D^{228,230,334,335}. Due to potentially harmful effects of global SEMA3A inhibition via NRP1, other options such as liver specific SEMA3A inhibition should be explored. Recently, Zhang et al. used a novel drug delivery system in mice whose spinal cord was severed, to specifically inhibit SEMA3A-binding in the region of interest²³⁸. Furthermore, a small osmotic pump has also been

shown to be a valid method to deliver a certain drug to an organ/area of interest²³⁰. Both methods could be employed to deliver an NRP1-antibody/SEMA3A inhibitor specifically to the liver, to test the effect on steatosis-induced defenestration. To further optimize this experiment, other molecules which inhibit SEMA3A-NRP1 interaction could be explored. Vinaxanthone and xanthofulvin e.g., both fungal peptides from a penicillin strain, have gained increasing attention in the past decades for their highly specific inhibition of SEMA3A³³⁶⁻³³⁸. Both have already been shown to have significant therapeutic effects *in vivo* in the setting of diabetic nephropathy and spinal cord injury without reported side effects^{228,230,232,238}. Due to SEMA3A also being able to exert an effect in the brain, it is important to know whether the aforementioned peptides/antibodies would be able to cross the blood-brain barrier²¹⁵. Alternatively, instead of inhibiting SEMA3A binding to NRP1, NRP1 could be targeted directly. In 2023, Zhou et al. used hydrodynamically injected short hairpin RNA (shRNA) to silence *Nrp1* in the livers of DIO mice and found that decreased levels of NRP1 were accompanied by less hepatic steatosis while overexpression led to increased hepatic steatosis³³⁹. Since they did not evaluate the hepatic sinusoids or VLDL secretion of those mice, one can only speculate about the effect of reduced *Nrp1* levels on fenestrations³³⁹.

Future research should focus on developing LSEC/liver-specific inhibitors of SEMA3A or SEMA3A-downstream components to improve sinusoidal fenestrations, possibly aiding recovery in early stages of MASLD by improving the bi-directional exchange between bloodstream and hepatocytes. This is of particular importance as in recent years the role and significance of fenestrated LSECs during liver disease and injury have become more prominent. Also, as of today, there is no liver-specific treatment on the market which ameliorates hepatic steatosis via reversal of capillarization.

6.3.3. Long-term genetic interference of SEMA3A signalling improves VLDL secretion and hepatic steatosis

As short-term inhibition of SEMA3A signalling in *db/db* mice only mildly affected hepatic steatosis (**Figure 21**), we aimed to explore the long-term inhibition via a conditional, endothelial cell-specific knockout of *Sema3a* in male C57BL/6J mice in the context of DIO. First and foremost, *iEC^{Sema3a}* mice have an improved VLDL secretion ability and reduced

hepatic steatosis compared to *iEC^{wt}* mice (**Figure 22**). Further, *iEC^{Sema3a}* mice presented with significantly lower body weight from week 15 onwards compared to *iEC^{wt}* mice (**Figure 22**). Since heightened energy expenditure and physical activity were found to be significantly increased in heterozygous global DIO *Sema3a^{+/-}* mice, this might also be the case in *iEC^{Sema3a}* mice, possibly resulting in peripheral tissues metabolizing lipids that would otherwise accumulate in the liver²⁴⁷. Most interestingly, *iEC^{Sema3a}* mice also have a tendentially higher fenestrae frequency and a numerically, however, on av. 80% increased LSEC porosity, which had a visible physiological impact as those mice have a significantly increased VLDL secretion from the liver (**Figure 22**). It should be noted that in the *iEC^{wt}* group, the mouse that weighed the least specifically had the highest fenestrae frequency, while the heaviest mouse of the *iEC^{Sema3a}* group had the lowest fenestrae frequency. Putting the results in relation to each other, the fenestrae frequency, LSEC porosity, and VLDL secretion of *iEC^{Sema3a}* and *iEC^{wt}* mice negatively correlated with their body weight, suggesting that weight can be a determinant for fenestrations as well as VLDL secretion.

Further, a numeric reduction in HOMA-IR and significant reduction in Adipo-IR along with reduced insulin concentrations at normal blood glucose concentrations indicate that whole-body and adipose tissue insulin sensitivity is improved in *iEC^{Sema3a}* versus *iEC^{wt}* mice. This falls in line with several publications, which found that fenestrae enable the transfer of insulin and that loss of fenestration coincides with increased insulin resistance, while reversal of capillarization increased insulin sensitivity³⁴⁰⁻³⁴².

Prospectively, it would be interesting to generate an inducible, endothelial cell-specific *Sema3a* knock-out line on a *db/db* background. This would allow to evaluate the therapeutic potential of *Sema3a* ablation in the setting of T2D instead of diet-induced obesity. Further, in order to investigate whether *Sema3a* ablation/SEMA3A inhibition would be beneficial in the setting of MASH, wildtype mice could be given a non-*trans* fats Western diet (WD-NTF) or a choline-deficient high-fat diet (CDHFD) prior to inducing *Sema3a* ablation/SEMA3A inhibition³⁴³. Both diets induce obesity and the metabolic syndrome while also inducing MASH after 12-16 weeks³⁴³. Importantly, these diets do not induce weight loss like other typical MASH diets such as the methionine-choline-deficient (MCD) diet³⁴³. While it seems plausible that there might be a benefit of SEMA3A inhibition in MASH, it seems improbable that there is one in cirrhosis as Samadan et al. found SEMA3A levels to be significantly increased in the blood serum of humans with MASLD, but decreased in

humans with cirrhosis compared to healthy individuals²⁴². This suggests that increased SEMA3A/*Sema3a* levels are particularly pertinent in early stages of MASLD. Furthermore, as cirrhosis progresses, hypoxia caused by vessel obstruction and capillarization increases angiogenic growth factors, such as VEGF-A, which might therefore reinduce fenestrations¹³⁵. However, angiogenesis and fibrogenesis as well as HCC development and progression are closely linked and an increase of angiogenesis can also result in an increase of fibrogenesis¹³⁵. Thus, the question arises whether in advanced stages of MASLD, i.e. fibrosis and HCC, increasing SEMA3A-signalling might be beneficial as it might reduce VEGF-induced angiogenesis and thus fibrogenesis and HCC progression. Maione et al. for instance have found that re-expressing SEMA3A in cancer cells reduces hypoxia, acting as an antiangiogenic factor which was able to convert metastatic lesions into benign lesions³⁴⁴. One limitation of this study was that we did not use an LSEC-specific knock-out model, but an endothelial cell-specific model, i.e. *Cdh5-Cre^{ERT2} × Sema3a^{fl/fl}*, as, to the best of our knowledge, no LSEC-specific *Cre* mouse line exists. Thus, other types of endothelial cells expressing *Cdh5*, such as pancreatic endothelial cells and endothelial cells in the brain, might have contributed to our phenotype³⁴⁵⁻³⁴⁷. However, as previously mentioned, liver-specific inhibition of NRP1, thus abrogating SEMA3A signalling, has been shown to significantly reduce hepatic steatosis, suggesting that loss of *Sema3a* in the liver was the major contributor for the observed phenotype³³⁹.

The results show clear indications for the beneficial effect of long-term inhibition of SEMA3A, specifically in endothelial cells, regarding hepatic steatosis. So far, this has not been evaluated in this context, and the combined positive effects make endothelial SEMA3A inhibition an attractive therapeutic target for several diseases including MASLD. Since there are currently no treatment options for MASLD approved in Europe, the reversal or halting of capillarization, as well as understanding the underlying mechanism, is a promising research objective and could pave the way to a new treatment approach.

7. Conclusion and Outlook

Taking all of our results together, we generated a hypothesized pathway which covers the downstream signalling of SEMA3A. Furthermore, we created a model which shows the possible impact of SEMA3A towards MASLD development via LSEC defenestration.

Using KAP, we were able to find increased activity of several kinases, including PKC α , PKG, PAK1, ROCK2, AMPK, Akt1, and IKK α/β (**Figure 23a**). Those kinases are all known to promote actin polymerization via different mechanisms and may contribute to a reduction of fenestrae frequency and LSEC porosity. Using western blot analysis, we specifically investigated the role of LIMK1 and cofilin-1 and found a tendentially increased cofilin-1 phosphorylation upon SEMA3A-Fc treatment in LSECs which could be abrogated via LIMK1 inhibition. Moreover, measuring the amounts of F- and G-actin we found that palmitic acid and SEMA3A-Fc treatment of LSECs resulted in an increased F-/G-actin ratio.

Collectively, SEMA3A reduces fenestration via NRP1, LIMK1, and cofilin-1, among others, and ultimately increases F-actin (**Figure 23b**). In obese and diabetic male *db/db* mice, which present with a higher *Sema3a* transcript abundance and higher levels of circulating saturated fatty acids, LSECs have a lower fenestrae frequency and LSEC porosity, while inducible, endothelial cell-specific *Sema3a* knockout mice present with numerically increased fenestrae frequency and LSEC porosity despite DIO. Additionally, these mice have an improved VLDL secretion ability and reduced hepatic steatosis compared to the respective control mice. This points to SEMA3A inhibition/*Sema3a* ablation as a valuable therapeutic target for MASLD and prospectively the prevention of HSC activation via LSEC dedifferentiation, as it may prevent or slow the progression towards fibrosis and cirrhosis.

Since it is not yet possible to analyse fenestrae in isolated human LSECs *in vitro*, an alternative future option, instead of primary mouse LSECs, to evaluate the effect of SEMA3A on fenestrae, would be to use human organotypic liver slices as a model³⁴⁸. This would allow not only evaluation of fenestrae sizes in humans upon SEMA3A treatment, but also its evaluation in a physiological setting as hepatocytes, KCs, and HSCs could be present. Precision-cut liver slices would also take the contribution of cellular and non-cellular components in their native histoarchitectural organisation to disease progression into account³⁴⁸. Here, we could test the effect of direct SEMA3A inhibition or inhibition of downstream signalling of SEMA3A and further evaluate the therapeutic potential as well as

possible side effects. Further, fenestrations can be analysed in the setting of different liver diseases and the effect of defenestration on the exchange of lipids between the blood flow and the hepatocytes can be more closely investigated. Since primary human LSECs as well as liver endothelial cell lines do not present with fenestrations, and access to primary human LSECs from cadaveric livers is limited by the availability of human ischemic sensitivity and organ availability²⁸⁷, organotypic liver slices present the best option next to primary mouse LSECs to investigate fenestrae.

As good, reliable blood serum markers for MASLD are scarce, and SEMA3A has been found to be increased in the setting of MASLD, further research into this area might help to manifest SEMA3A blood serum concentrations as a novel, quick and easy determinant for MASLD²⁴². To this end, blood serum samples from MASLD patients of different stages should be analysed.

To further explore downstream signalling of SEMA3A, previously identified kinases could be further investigated in the context of SEMA3A-induced defenestration. By inhibiting potential candidates and subsequently evaluating fenestrae, their contribution to the phenotype can be explored to get a better understanding of the mechanism behind defenestration and conversely fenestrae formation. To further gain insights into the effect of *Sema3a* ablation, RNA sequencing with livers from male and female *iEC^{Sema3a}* and *iEC^{wt}* mice could be used to investigate how and if loss of *Sema3a* has an impact on the expression of certain genes in LSECs and indirectly other hepatic cells. This could help to identify and assess cellular events outside of LSECs which might be affected by the loss of *Sema3a* such as changes in the lipid metabolism in hepatocytes and/or the inflammatory response of HSC. It might also help to get a better comprehension of the sex-specific differences regarding MASLD progression. Further, the livers of male and female *db/db* mice should be analysed again after successive perfusion of the liver, in order to confirm the previously shown sex-specific differences in the hepatic sinusoids.

As a dynamic actin cytoskeleton is important for fenestrae maintenance, one could use STED microscopy or AFM in order to evaluate how SEMA3A impacts the actin-network in living cells. These methods could also be useful to test SEMA3A inhibitors in LSECs as the effect would be visible nearly immediately, while SEM analysis is more time-consuming. Also, one downside to SEM is that it does not capture time- and space-dependent dynamics, however, fenestrae are very dynamic structures.

Due to potentially harmful and unspecific effects of global SEMA3A inhibition via NRP1, options such as liver-specific SEMA3A or NRP1 inhibition should be explored. This could be done by using a drug delivery system or a small osmotic pump which only releases an inhibitor in proximity to the liver, or by using shRNA and hydrodynamic injections. Subsequently, the VLDL secretion rate and fenestrations should be analysed to evaluate the benefits regarding lipid exchange. Further, other specific inhibitors of SEMA3A- but not VEGF-binding to NRP1, such as vinaxanthone and/or xanthofulvin should be explored, since these have already been shown to be effective in *in vivo* applications^{238,239,349}.

For future experiments, an inducible, endothelial cell-specific *Sema3a* knock-out line on a *db/db* background might be of interest as it would allow to evaluate the therapeutic potential of *Sema3a* ablation in the setting of T2D instead of diet-induced obesity. Further, in order to investigate whether *Sema3a* ablation/SEMA3A inhibition would be beneficial in the setting of MASH, mice could be given a WD-NTF or CDHFD, which both induce obesity and the metabolic syndrome while also inducing MASH after 12-16 weeks³⁴³.

Another advantage of *Sema3a* ablation/SEMA3A inhibition and subsequent increase of fenestrations, might be a reduced risk of atherosclerosis, a coronary artery disease in which lipid accumulation in arteries triggers inflammation via endothelial cell activation³⁵⁰. This was first suggested by Fraser et al. who postulated that the loss of fenestrations is a major contributor to the development of atherosclerosis as the uptake of chylomicron remnants would be impaired^{74,88,104,351}. Further, Fu et al., who inhibited SEMA3A via hydrodynamic injections of siRNA inhibiting *Sema3a* transcription, found decreased endothelial cell activation upon lipopolysaccharide treatment, as well as reduced vascular inflammation and oxidative stress³⁵². The effect of *Sema3a* ablation/SEMA3A inhibition on the development on atherosclerosis could be evaluated by measuring inflammatory cytokine levels, adhesion molecule expression, and vascular injury.

In summary, SEMA3A and SEMA3A signalling present themselves as promising targets to ameliorate hepatic steatosis and prevent or slow MASLD progression. Our results also highlight the importance of fenestrations regarding hepatic steatosis and VLDL secretion and thus fenestrae as a novel target for prevention of lipid retention. Further studies are necessary to clarify the potential of SEMA3A inhibition/*Sema3a* deletion and reformation of fenestrae as a pharmaceutical intervention for MASLD.

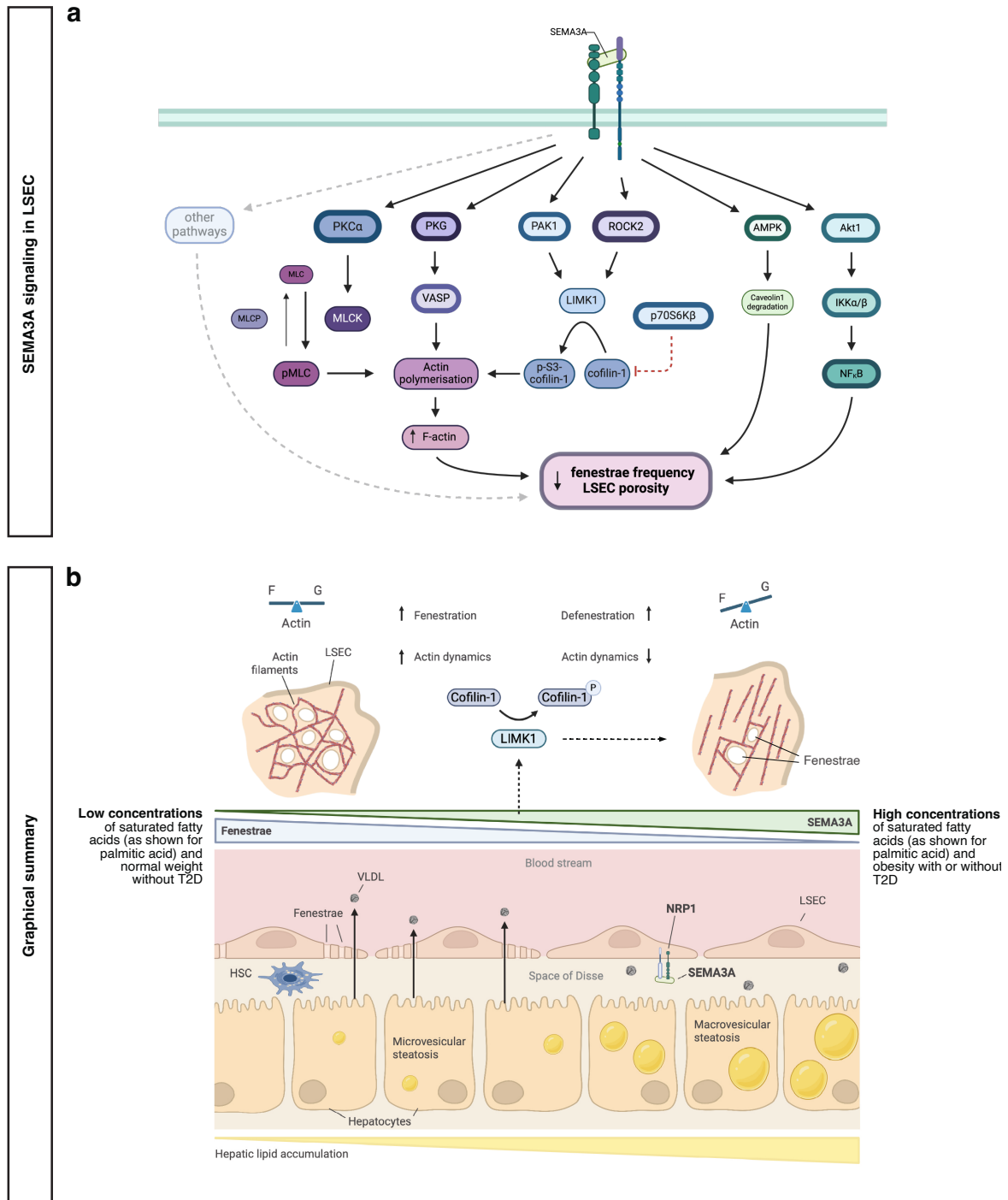


Figure 23. SEMA3A downstream signaling and graphical summary.

a Hypothesized pathways which result in loss of fenestration in LSECs with a focus on actin-manipulating components. Kinases with a thick outline were found to be activated upon SEMA3A treatment in LSECs, as determined by the kinase activity profiling. Created with BioRender.com. **b** Graphical summary. Left side: in the setting of low physiological SEMA3A levels (as is the case at low concentrations of saturated fatty acids and normal BW without T2D), active cofilin-1 and normal F-actin cytoskeleton dynamics contribute to maintain a high frequency of fenestrae in LSECs. LSEC porosity facilitates bidirectional exchange of lipids between bloodstream and hepatocytes, such as the release of VLDL particles from hepatocytes into the blood circulation. Right side: in the setting of high SEMA3A levels (as is the case at high concentrations of FFAs and in DIO with or without T2D), the angiocrine signal SEMA3A acts via NRP1 on LSECs to activate multiple STKs, including LIMK1, which phosphorylates cofilin-1 to reduce F-actin cytoskeleton dynamics and fenestrae frequency as well as LSEC porosity. The reduced LSEC porosity lowers VLDL export from the hepatocytes into the blood and might contribute to lipid retention and macrovesicular steatosis in the hepatocytes. The resulting hepatic steatosis is an early event in MASLD that can subsequently (in concert with hepatic stellate cells; HSCs) progress to severe hepatic and cardiometabolic diseases. Created with BioRender.com, from Eberhard, et al. ²⁴⁷.

8. List of Abbreviations

°	Degree
Σ	Sum
ABC1	ABC1 domain containing kinase
ACOX1	Peroxisomal acyl-coenzyme A oxidase 1
Adipo-IR	Adipose tissue insulin resistance
AFM	Atomic force microscopy
AGC	Protein kinase A, G, and C group
Akt1	AKT serine/threonine kinase 1
Alpha	Alpha kinase group
ALT	Alanine transaminase
AMPK	AMP-activated protein kinase
ANOVA	Analysis of variance
Apo B-100	Apolipoprotein B-100
ASK1	Apoptosis signal-regulating kinase 1
AST	Aspartate transaminase
ATP	Adenosine triphosphate
Av.	Average
BCA	Bicinchoninic acid assay
Brd	Bromodomain proteins
BSA	Bovine serum albumin
BW	Body weight
C	Celsius

CAC1C	Voltage-dependent L-type calcium channel subunit alpha-1C
CAMK	Calcium and calmodulin-regulated kinase group
CCL2	Chemokine (C-C motif) ligand 2
CCR2/5	C-C chemokine receptor type 2/5
CD146	Cluster of differentiation 146
CD36	Cluster of differentiation 36
CDA	Choline-deficient L-amino acid defined
Cdh5	Cadherin 5
CDHFD	Choline-deficient high fat diet
cDNA	Complementary DNA
ChREBP	Carbohydrate response element binding protein
CK1	Cell kinase 1
cm	Centimeter
CMGC	CDK, MAPK, GSK, and CK2 kinase group
CO₂	Carbondioxide
COS-7	African green monkey kidney fibroblast-like cell line
CPN	Contour proposal network
CPT1	Carnitine O-palmitoyltransferase 2, mitochondrial
Cre-ERT2	Cre recombinase fused to a triple mutant form of the human estrogen receptor
CREB1	CAMP responsive element binding protein 1
CT	Cycle threshold
CTCF	Corrected total cell fluorescence
d	Diameter
DAMP	Damage associated molecular pattern

db/db	Diabetic mouse model (<i>BKS.Cg-Dock^{7m} +/+ Lep^{dbJ}</i>)
DIO	Diet-induced obesity
DLW	Deep learning workflow
DMSO	Dimethyl sulfoxide
dNTP	Deoxynucleotide triphosphates
L-DOPA	3,4-dihydroxyphenylalanine
DPBS	Dulbecco's phosphate buffered saline
DRG	Dorsal root ganglia
dSTORM	<i>direct</i> stochastic optical reconstruction microscopy
ECM	Extracellular matrix
EDTA	Ethylenediaminetetraacetic acid
EGFR	Epidermal growth factor receptor
EMB-2	Endothelial basal medium
eNOS	Endothelial nitric oxide synthase
ET-1	Endothelin-1
EV	Extracellular vesicle
F-actin	Filamentous actin
FABP	Fatty acid binding protein
FAO	Fatty acid oxidation
FARP2	FERM, RhoGEF and pleckstrin domain-containing protein 2
FATP	Fatty acid transport protein
FDA	Food and drug administration
FFA	Free fatty acid
FFC	Fenestrae forming centre

FXR	Farnesoid X receptor
<i>g</i>	Gravitational force
g	Grams
G-actin	Globular actin
GGT	Gamma-glutamyltransferase
GIP-R	Glucose-dependent insulinotropic polypeptide receptor
GLP-1R	Glucagon-like peptide 1 receptor
GOI	Gene of interest
GPI	Glycosylphosphatidylinositol
H₂O	Water
HCC	Hepatocellular carcinoma
HDL	High-density lipoprotein
HFD	High-fat diet
HGF	Hepatocyte growth factor
HMGB1	High mobility group box 1
HOMA-IR	Homeostatic model assessment for insulin resistance
Hprt	Hypoxanthine-guanine phosphoribosyltransferase
HRP	Horseradish peroxidase
hs-CRP	High sensitivity C-reactive protein
HSC	Hepatic stellate cells
i.e.	Lat.:id est (that is)
ICAM-1	Intracellular adhesion molecule 1
<i>iEC^{wt}</i>	<i>Cdh5-Cre^{ERT2}</i> control mice
<i>iEC^{Sema3a}</i>	<i>Cdh5-Cre^{ERT2} × Sema3a^{fl/fl}</i> mice (inducible, endothelial cell-specific, knockout of <i>Sema3a</i>)

Ig	Immunoglobulin
IgG	Immunoglobulin G
IKKα/β	Inhibitor of nuclear factor kappa-B kinase subunit alpha/beta
IL-1	Interleukin 1
IL-6	Interleukin 6
KAP	Kinase activity profiling
KC	Kupffer cell
kg	Kilogram
kJ	Kilojoule
KLF2	Kruppel-like factor 2
LIMK1	LIM domain kinase 1
LPL	Lipoprotein lipase
LRRC16A	Capping protein regulator and myosin 1 linker 1
LSEC/LSECs	Liver sinusoidal endothelial cell/s
LYVE-1	Lymphatic vessel endothelial hyaluronan receptor 1
M	Mol
M-CSF	Macrophage colony-stimulating factor
MACS	Magnetic-activated cell sorting
MASH	Metabolic-dysfunction associated steatohepatitis
MASLD	Metabolic-dysfunction associated hepatic steatosis
MBOAT7	Membrane-bound O-acyltransferase domain-containing protein 7
MCD	Methionine-choline-deficient
MCP1	Monocyte chemoattractant protein 1
mg	Milligram

min	Minute/s
ml	Milliliter
mm	Millimeter
mM	Millimolar
MRI-PDFF	Magnetic resonance imaging proton density fat fraction
mRNA	Messenger RNA
mTOR	Mammalian target of rapamycin
MTTP	Microsomal triglyceride transfer protein
MTvC	Multiple treatments <i>versus</i> control
MYDGF	Myeloid-derived growth factor
NaF	Sodium fluoride
NAFLD	Non-alcoholic fatty liver disease
NEFA	Non-esterified fatty acid
NFκB	Nuclear factor kappa-light-chain-enhancer of activated B cells
nm	Nanometer
NO	Nitric oxide
NRP1/2	Neuropilin1/2
OsO₄	Osmium tetroxide
p-S3-cofilin-1	At serine 3 residue phosphorylated cofilin-1
p-value	Probability value
p70S6β	Ribosomal protein S6 kinase beta-1
PAK1	p21 (Rac1) activated kinase 1
PBS	Phosphate buffered saline
PBST	Phosphate buffered saline with 0.1% Tween® 20

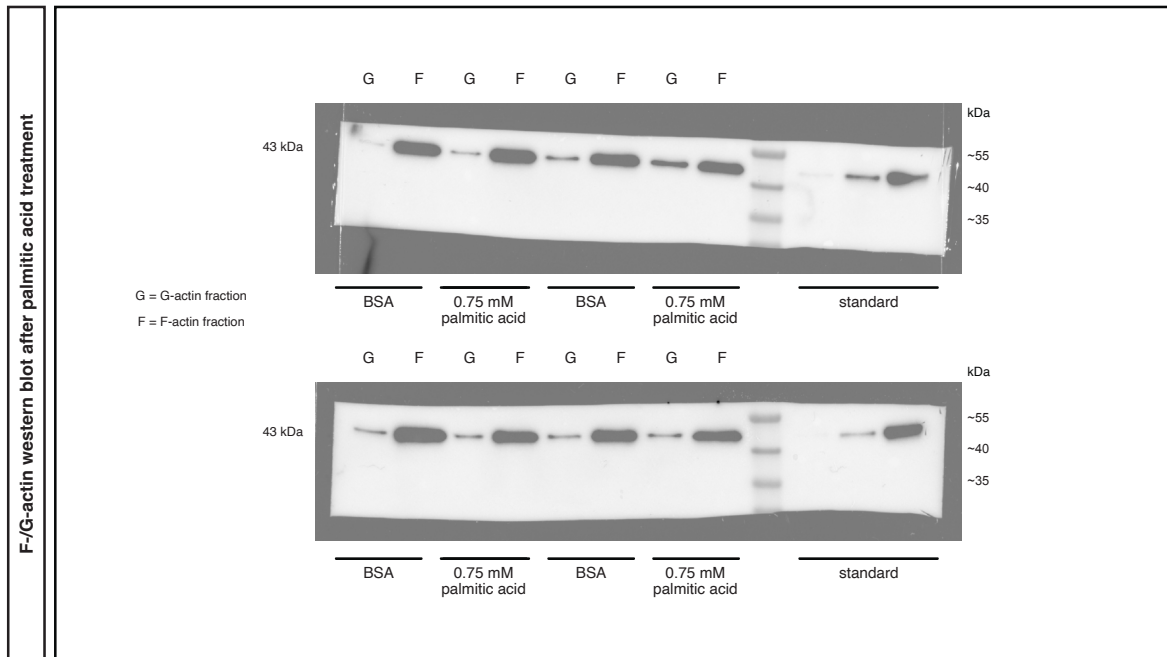
PCA	Principle component analysis
PDGF	Platelet-derived growth factor
PDHK	Pyruvate dehydrogenase kinase group
PDK4	Pyruvate dehydrogenase lipoamide kinase isozyme 4
PEB Buffer	PBS, EDTA, and BSA containing buffer
PFA	Paraformaldehyde
PIIINP	Type III procollagen peptide
PIKK	Phosphatidylinositol 3' kinase-related kinase group
PKCa	Protein kinase C alpha
PKG	cGMP-dependent protein kinase
PLVAP	Plasmalemma vesicle associated protein
pmol	picomol
PNPLA3	Patatin-like phospholipase domain-containing protein 3
PPARα/γ	Peroxisome proliferator-activated receptor alpha/gamma
PSI	Plexin, semaphorin, and integrin
PTK	Protein tyrosine kinases
r	Radius
R2	Coefficient of determination
Rac1	Ras-related C3 botulinum toxin substrate 1
RIO	RIO kinase group
RIPA	Radioimmunoprecipitation assay
RM	Repeated measures
RNA	Ribonucleic acid
ROCK2	Rho associated coiled-coil containing protein kinase 2

ROS	Reactive oxygen species
RPLP0	60S acidic ribosomal protein P0
RSECP	Residential sinusoidal endothelial cell progenitors
RT	Room temperature
RT-qPCR	Real-time quantitative polymerase chain reaction
s	Second/s
SEM	Scanning electron microscopy
SIM	Structured illumination microscopy
siRNA	Small interfering RNA
SREBP1c	Sterol regulatory element-binding protein 1
STE	STE group
STED	Stimulated emission depletion
STK	Serine-threonine kinases
T2D	Type 2 diabetes mellitus
TG	Triglycerides
TIF1	Transcriptional intermediary factor 1
TIMP-1	TIMP metalloproteinase inhibitor 1
TK	Tyrosine kinase group
TKL	Tyrosine kinase-Like (TKL) group
TM6SF2	Transmembrane 6 superfamily 2
TMS	Tetramethylsilane
TNF-α	Tumour necrosis factor alpha
TY3H	Tyrosine 3-monooxygenase
UKA	Upstream kinase analysis

USA	United States of America
VAP-1	Vascular adhesion protein 1
VASP	Vasodilator-stimulated phosphoprotein
VCAM-1	Vascular cell adhesion protein 1
VEGF	Vascular endothelial growth factor
VEGFR2	Vascular endothelial growth factor receptor 2
VLDL	Very low density lipoprotein
WD-NTF	Non-trans fats western diet
μl	Microliter
μm	Micrometer
μM	Micromolar

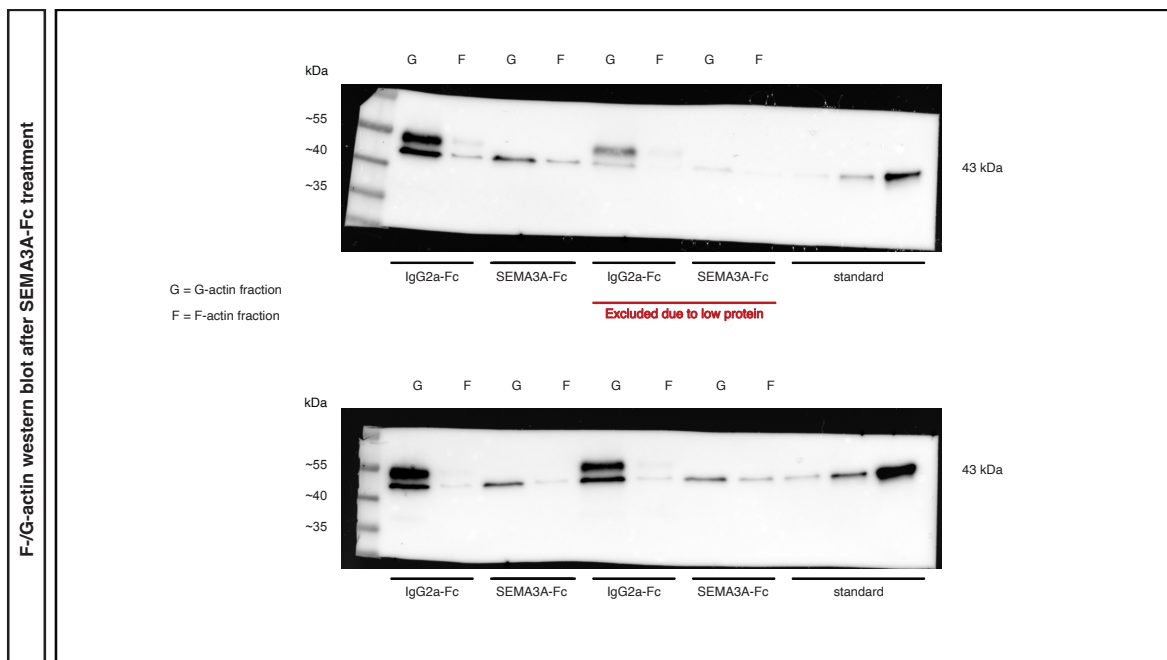
9. Supplementary Data

9.1. F-/G-actin western blot of human LSECs treated with palmitic acid



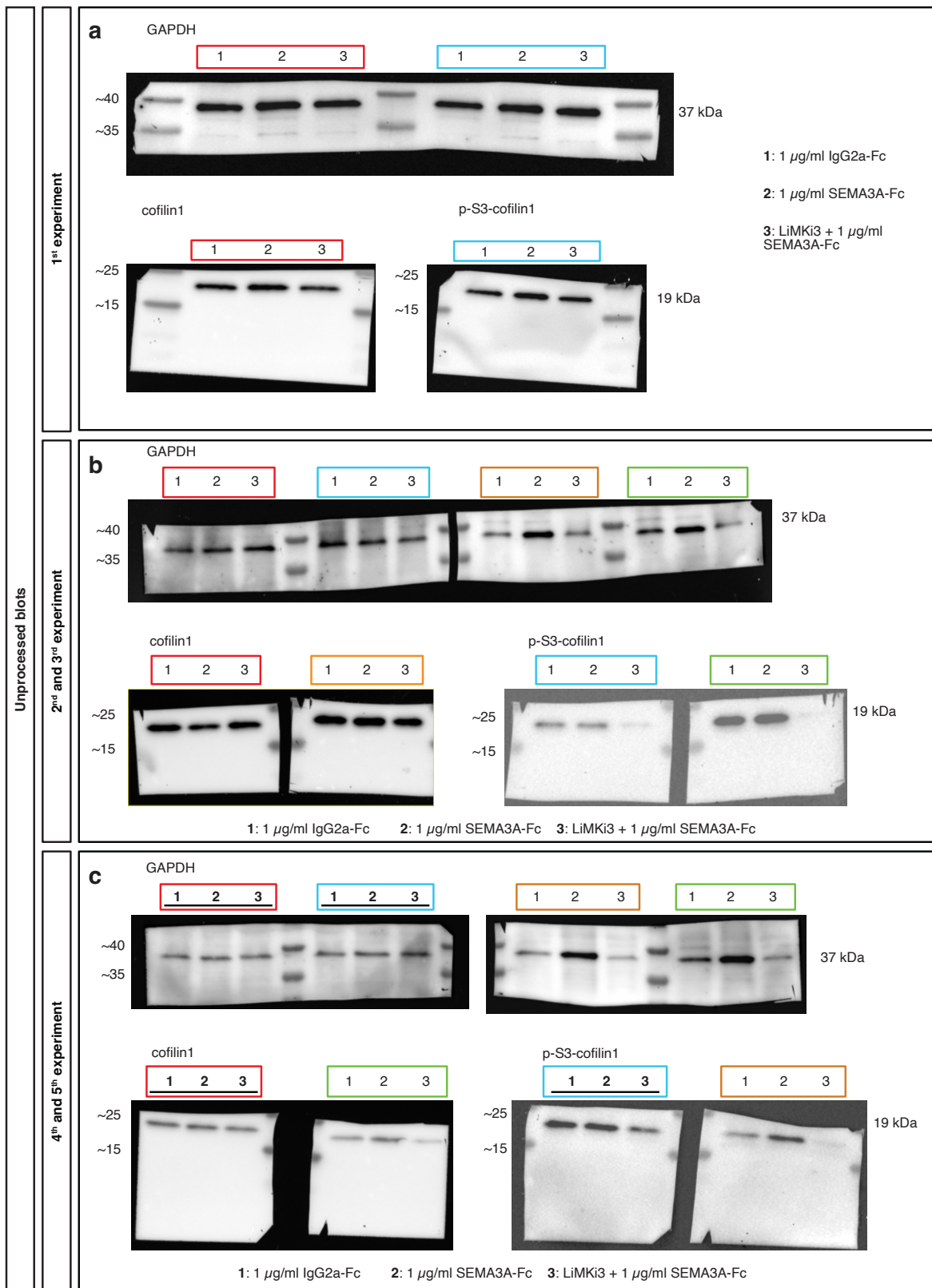
Supplementary Figure 1. F-/G-actin western blot of human LSECs treated with BSA or 0.75 mM palmitic acid.

9.2. F-/G-actin western blot of mouse LSECs treated with SEMA3A-Fc



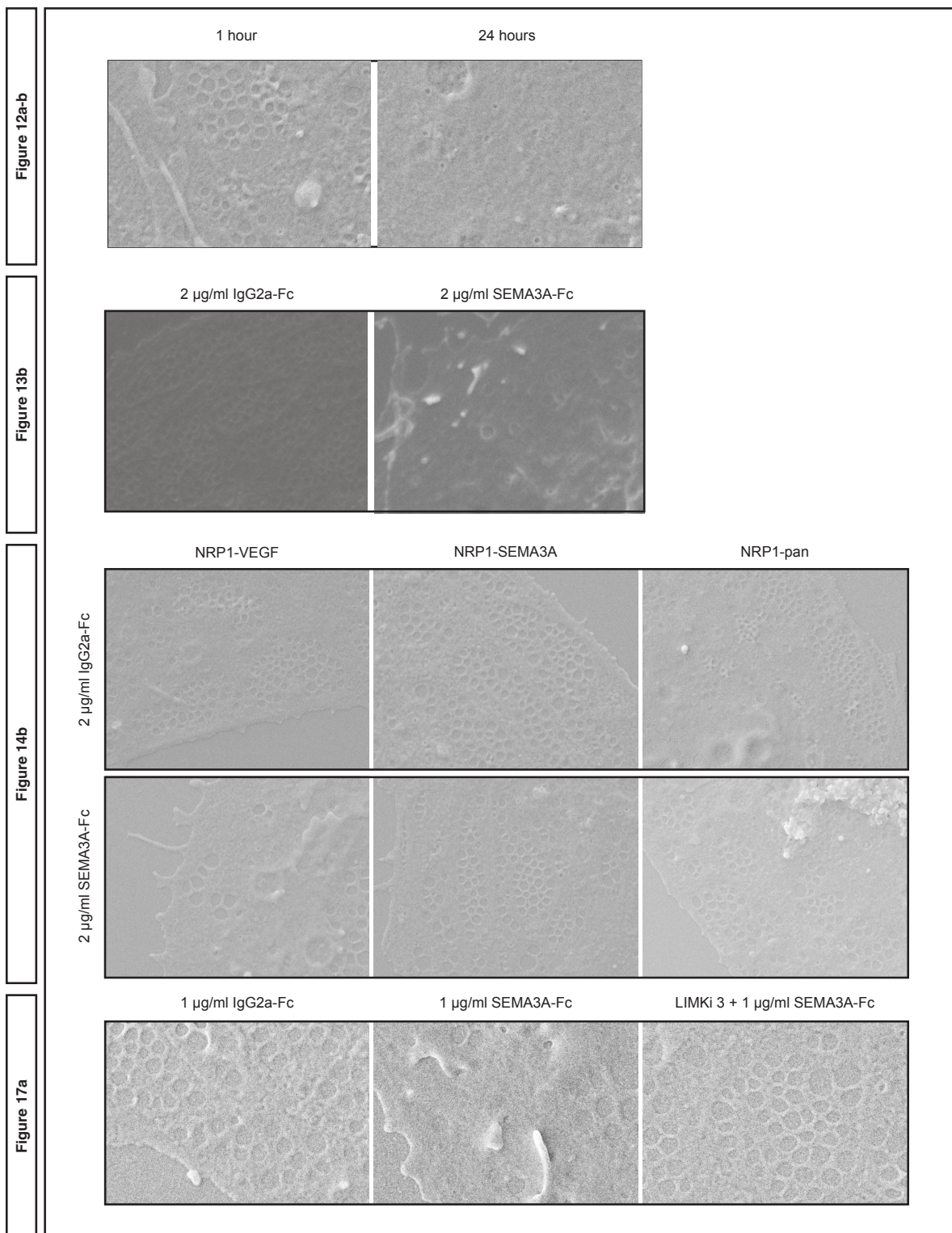
Supplementary Figure 2. F-/G-actin western blot of mouse LSECs treated with 2 µg/ml IgG2a-Fc or SEMA3A-Fc.

9.3. Western blots of mouse LSECs treated with IgG2a-Fc, SEMA3A-Fc, and LIMK i3



Supplementary Figure 3. Western blots of mouse LSEC treated with IgG2a-Fc, SEMA3A-Fc, and LIMK i3.
 Colored boxes indicate which GAPDH quantities were used for normalization of either cofilin-1 or p-S3-cofilin-1.

9.4. Raw SEM images



Supplementary Figure 4. Raw SEM images.
SEM images, unedited and without colored fenestrae.

9.5. Deep learning workflow – post-analysis script

```

import math
import os
from distutils.command.install_egg_info import to_filename
from encodings.utf_8 import encode
from tkinter.filedialog import SaveAs

import numpy as np
import openpyxl
import pandas as pd
import seaborn as sns

# define source folder
plugin_dir = "filepath"

# define output folder
res_dir = f'filepath'

# create dir for output figures + data
os.makedirs(res_dir, exist_ok=True)

# if certain fenestrae are supposed to be removed, add the names of the label after drop
samplePath = f'{plugin_dir}/{"sample name"}'
saml_name = os.path.basename(samplePath)
sample_name = saml_name.replace('.csv', '')
data = pd.read_csv(samplePath)
data.drop([number of fenestae])
data.to_csv(f'{plugin_dir}/{sample_name}_clean.csv')

def JulichAnalysis(sample):
    print(sample)
    os.listdir(plugin_dir) == sample
    # read the list
    samplePath = f'{plugin_dir}/{sample}'
    data = pd.read_csv(samplePath)

    # fenestrae number
    fen_num = len(data.index)

    # average fenestrae diameter in nm
    ffen_dia = data.iloc[0:,2].astype(float)
    fen_dia = ffen_dia.mean()/insert pixel/μm value*1000

    # enter here the conversion used for the pictures
    data.iloc[0:,2] = data.iloc[0:,2].astype(float)/insert pixel/μm value*1000

    # total fenestrae area in μm^2

```

```

data['Fen_Area'] = (data.iloc[0:,2]/2)*(data.iloc[0:,2]/2)*math.pi
fen_area = sum(data.iloc[0:,3])/1000000

# define file name
fil_name = os.path.basename(samplePath)
file_name = fil_name.replace('.csv', '')

# merge
analysis_list = pd.DataFrame([file_name, fen_area, fen_num, fen_dia])
fin_list = analysis_list.transpose()
print(fin_list)

#save to folder
fin_list.to_excel(f'{res_dir}/{file_name}_counts.xlsx')
return fin_list

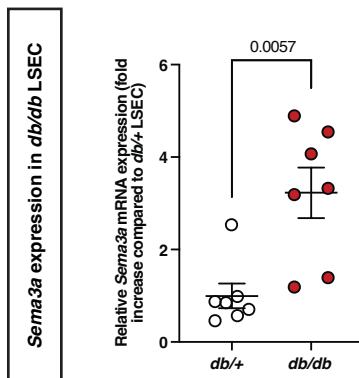
#make list with all the results
SampleList = os.listdir(plugin_dir)

#iterate through list and save table
res_list = [JulichAnalysis(file) for file in SampleList if file.endswith("csv")]
resDf = pd.concat(res_list)
resDf.columns = ['ID', 'total fenestrae area [µm]', 'fenestrae number', 'fenestrae
diameter [nm]']
resDf.to_excel(res_dir+"Total_Results.xlsx")

```

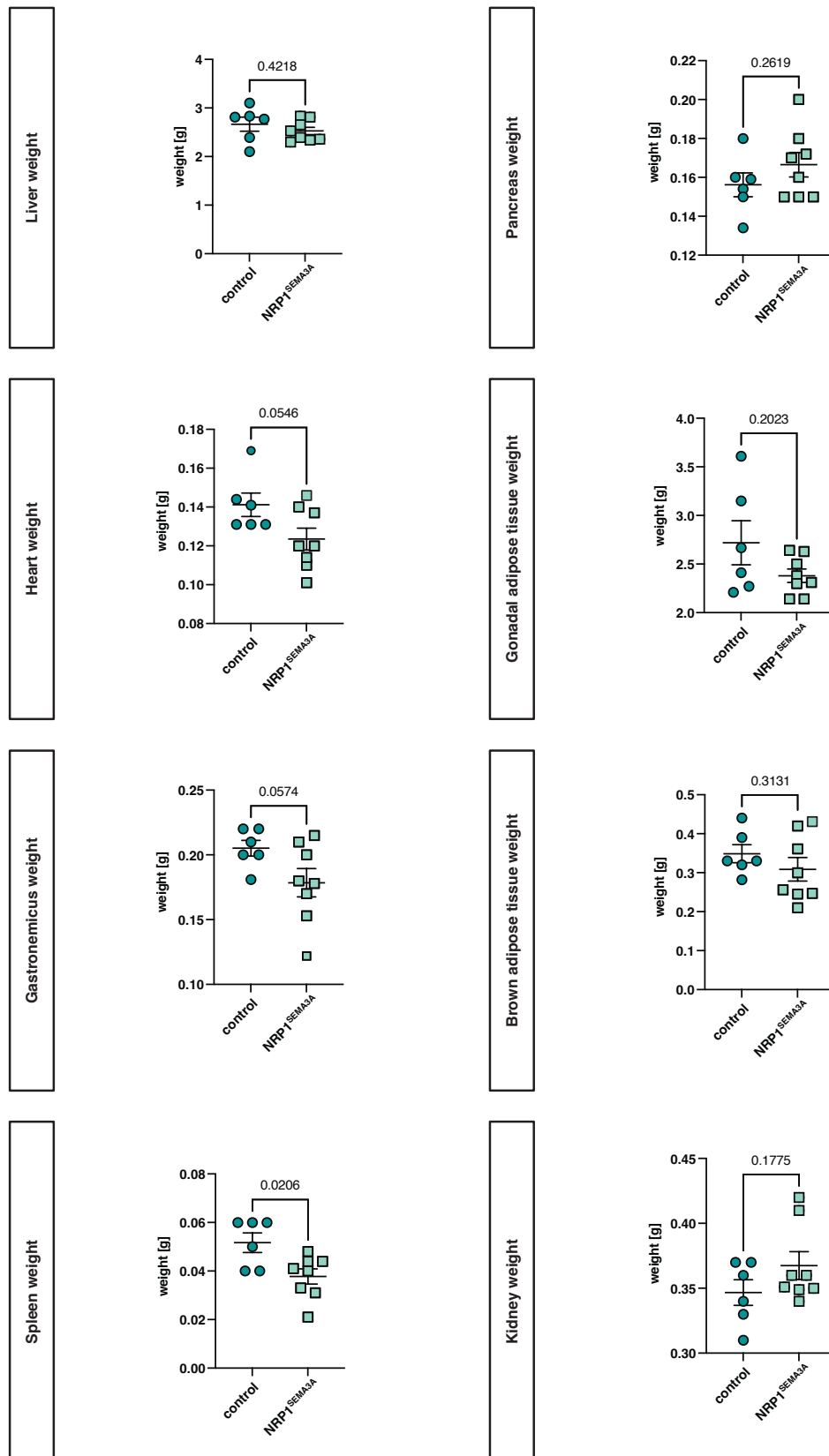
Supplementary Figure 5. Deep learning workflow post-analysis script (Python).

9.6. *Sema3a* expression in *db/db* mice

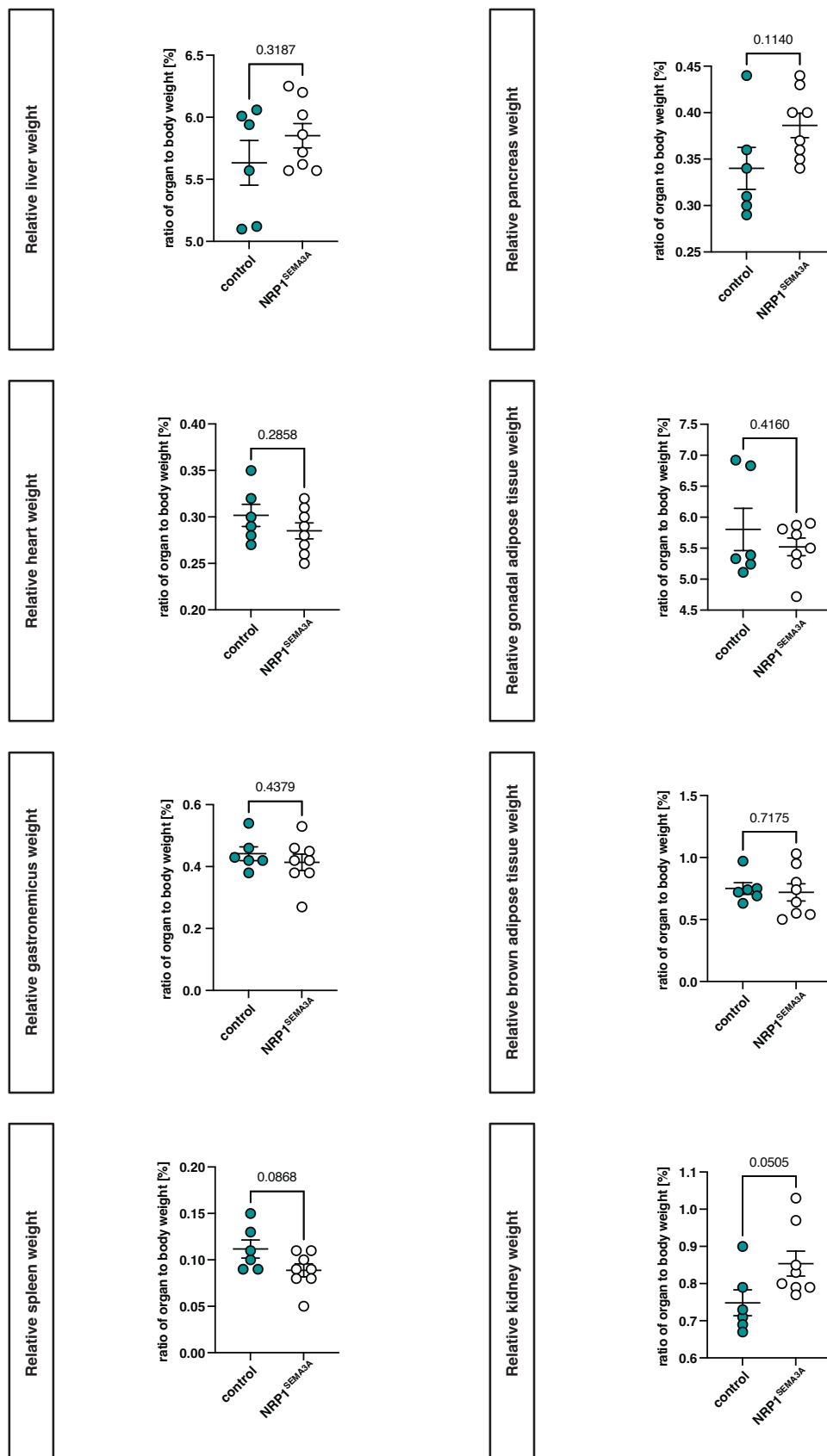


Supplementary Figure 6. *Sema3a* expression in *db/+* and *db/db* mice

Sema3a mRNA expression of LSECs from 12-week-old male *db/+* control versus *db/db* mice (n = 7 each). CD146⁺ LSECs were isolated by MACS. A two-tailed unequal variances *t*-test was used for statistical analysis. Data are presented as mean ± s.e.m. with the p-value.

9.7. Organ weights of male *db/db* mice treated with NRP1^{SEMA3A}**Supplementary Figure 7. Organ weights of *db/db* mice treated with NRP1^{SEMA3A}.**

Organ weights of *db/db* versus *db/+* mice including liver, pancreas, heart, gonadal white fat, gastrocnemius muscle, brown adipose tissue, spleen, and kidney. For statistical analysis a two-tailed unequal variances *t*-test was used for statistical analysis ($n = 6-8$). In all graphs data points, mean \pm s.e.m., and the p-values are presented.

9.8. Relative organ weights of male *db/db* mice treated with NRP1^{SEMA3A}**Supplementary Figure 8. Organ weight in relation to body weight of *db/db* mice treated with NRP1^{SEMA3A}.**

Organ weights in relation to the body weight (%) of *db/db* versus *db/+* mice including liver, pancreas, heart, gonadal white fat, gastrocnemius muscle, brown adipose tissue, spleen, and kidney. For statistical analysis a two-tailed unequal variances *t*-test was used for statistical analysis ($n = 6-8$). In all graphs data points, mean \pm s.e.m., and the p-values are presented.

9.9. BioRender publication licenses



49 Spadina Ave. Suite 200
Toronto ON M5V 2J1 Canada
www.biorender.com

Confirmation of Publication and Licensing Rights

August 17th, 2024
Science Suite Inc.

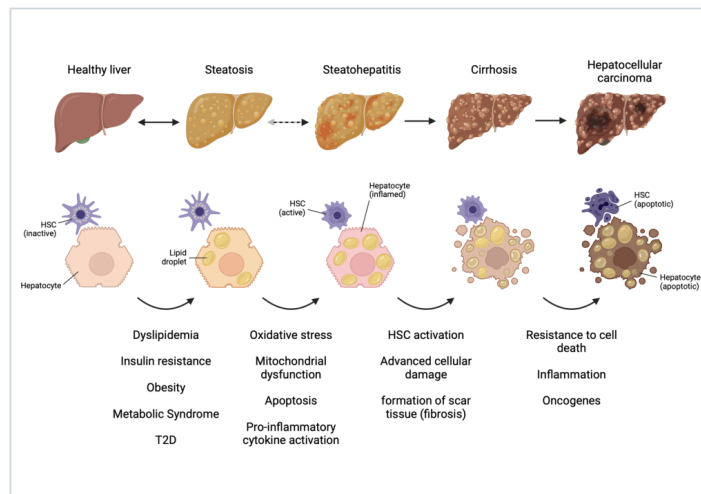
Subscription: Student Plan
Agreement number: JG27704RY6
Journal name: PhD Thesis from Sydney Balkenhol

To whom this may concern,

This document is to confirm that Sydney Balkenhol has been granted a license to use the BioRender content, including icons, templates, and other original artwork, appearing in the attached completed graphic pursuant to BioRender's [Academic License Terms](#). This license permits BioRender content to be sublicensed for use in journal publications.

All rights and ownership of BioRender content are reserved by BioRender. All completed graphics must be accompanied by the following citation: "Created with [BioRender.com](#)".

BioRender content included in the completed graphic is not licensed for any commercial uses beyond publication in a journal. For any commercial use of this figure, users may, if allowed, recreate it in BioRender under an Industry BioRender Plan.



For any questions regarding this document, or other questions about publishing with BioRender refer to our [BioRender Publication Guide](#), or contact BioRender Support at support@biorender.com.

Supplementary Figure 9. Publication license for Figure 4.



49 Spadina Ave. Suite 200
 Toronto ON M5V 2J1 Canada
 www.biorender.com

Confirmation of Publication and Licensing Rights

August 15th, 2024
 Science Suite Inc.

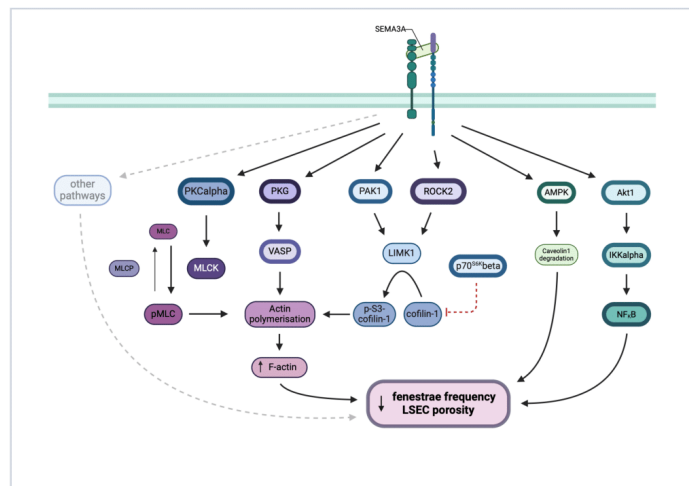
Subscription: Student Plan
Agreement number: AT276R2A40
Journal name: PhD Thesis from Sydney Balkenhol

To whom this may concern,

This document is to confirm that Sydney Balkenhol has been granted a license to use the BioRender content, including icons, templates, and other original artwork, appearing in the attached completed graphic pursuant to BioRender's [Academic License Terms](#). This license permits BioRender content to be sublicensed for use in journal publications.

All rights and ownership of BioRender content are reserved by BioRender. All completed graphics must be accompanied by the following citation: "Created with [BioRender.com](#)".

BioRender content included in the completed graphic is not licensed for any commercial uses beyond publication in a journal. For any commercial use of this figure, users may, if allowed, recreate it in BioRender under an Industry BioRender Plan.



For any questions regarding this document, or other questions about publishing with BioRender refer to our [BioRender Publication Guide](#), or contact BioRender Support at support@biorender.com.

Supplementary Figure 10. Publication license for Figure 23a.



49 Spadina Ave. Suite 200
Toronto ON M5V 2J1 Canada
www.biorender.com

Confirmation of Publication and Licensing Rights

July 31st, 2024
Science Suite Inc.

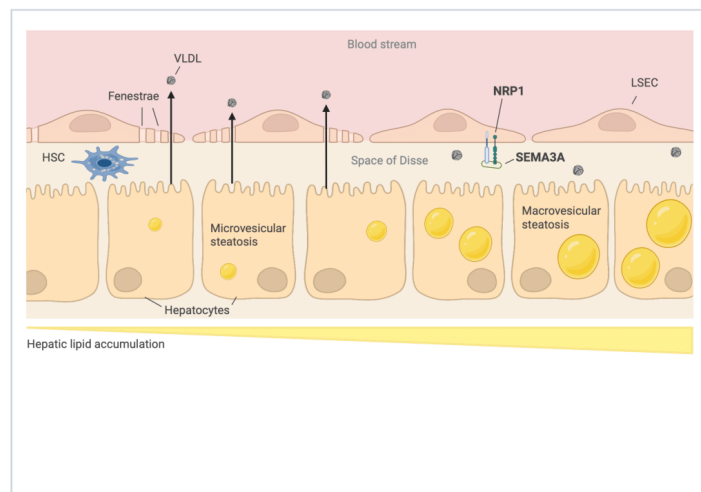
Subscription: Student Plan
Agreement number: OV274KOPNK
Journal name: PhD Thesis from Sydney Balkenhol

To whom this may concern,

This document is to confirm that Sydney Balkenhol has been granted a license to use the BioRender content, including icons, templates and other original artwork, appearing in the attached completed graphic pursuant to BioRender's [Academic License Terms](#). This license permits BioRender content to be sublicensed for use in journal publications.

All rights and ownership of BioRender content are reserved by BioRender. All completed graphics must be accompanied by the following citation: "Created with BioRender.com".

BioRender content included in the completed graphic is not licensed for any commercial uses beyond publication in a journal. For any commercial use of this figure, users may, if allowed, recreate it in BioRender under an Industry BioRender Plan.



For any questions regarding this document, or other questions about publishing with BioRender refer to our [BioRender Publication Guide](#), or contact BioRender Support at support@biorender.com.

Supplementary Figure 11. Publication license for Figure 23b.



49 Spadina Ave. Suite 200
Toronto ON M5V 2J1 Canada
www.biorender.com

Confirmation of Publication and Licensing Rights

May 6th, 2024
Science Suite Inc.

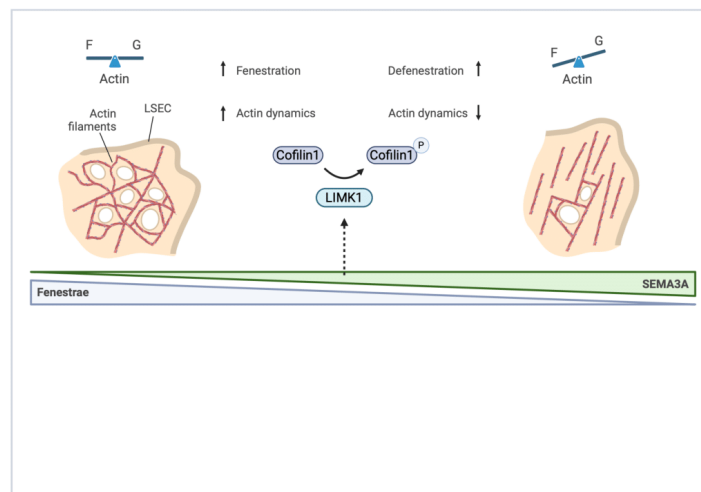
Subscription: Student Plan
Agreement number: EG26SAXCR7
Journal name: My PhD Thesis

To whom this may concern,

This document is to confirm that Sydney Balkenhol has been granted a license to use the BioRender content, including icons, templates and other original artwork, appearing in the attached completed graphic pursuant to BioRender's [Academic License Terms](#). This license permits BioRender content to be sublicensed for use in journal publications.

All rights and ownership of BioRender content are reserved by BioRender. All completed graphics must be accompanied by the following citation: "Created with BioRender.com".

BioRender content included in the completed graphic is not licensed for any commercial uses beyond publication in a journal. For any commercial use of this figure, users may, if allowed, recreate it in BioRender under an Industry BioRender Plan.



For any questions regarding this document, or other questions about publishing with BioRender refer to our [BioRender Publication Guide](#), or contact BioRender Support at support@biorender.com.

Supplementary Figure 12. Publication license for Figure 23b.

9.10. PamGene – Upstream kinase analysis

Supplementary Table 1. Raw PamGene data from the upstream kinase analysis.

Kinase UniProt ID	Kinase Name	Kinase Group	Kinase Family	Mean Specificity Score	Mean Significance Score	Mean Final Score	Median Final score	Mean Kinase Statistic	Median Kinase Statistic	SD Kinase Statistic	Mean peptide set size
P17252	PKC[alpha]	AGC	PKC	2.554411116	2.211895363	4.766306479	4.795880017	0.949545333	0.932912435	0.032879843	27.33333333
Q13237	PKG2	AGC	PKG	2.645956532	2.020289554	4.675246041	4.795880017	0.945552339	0.95242151	0.027854089	35.77777778
P17162	PKA[alpha]	AGC	PKA	2.698970004	1.88648554	4.585455444	4.443697499	0.865356289	0.871424622	0.02096102	52.22222222
Q13976	PKG1	AGC	PKG	2.579060977	1.829472328	4.408533005	4.443697499	0.934222825	0.933026004	0.053781785	39.33333333
P51817	PRXK	AGC	PKA	2.266071662	1.803858829	4.069930491	4.397940009	0.892547142	0.90001277	0.049612853	32
Q9P1W9	Pim2	CAMK	PIM	1.985199454	2.028205083	4.013404537	4.251811973	0.807305007	0.80900584	0.048422125	37.11111111
Q9UB50	p705K[beta]	AGC	RSK	2.095330972	2.089741515	4.185072487	4.05517328	0.975849283	0.965238406	0.07637519	24
P11309	Pim1	CAMK	PIM	1.826750164	1.853037763	3.679787927	3.665546249	0.737005959	0.732427471	0.011501612	59.55555556
Q86V86	Pim3	CAMK	PIM	1.636851882	1.80846608	3.445317461	3.540607512	0.731299982	0.729693443	0.010575007	56.88888889
Q05655	PKC[delta]	AGC	PKC	1.277574027	2.211895363	3.48946939	3.318758763	0.825760292	0.792242025	0.061976809	22.22222222
P31751	Akt2/PKB[beta]	AGC	AKT	1.438042353	1.74983232	3.187877585	3.251811973	0.823861763	0.830337781	0.030337781	25.77777778
P05129	PKC[gamma]	AGC	PKC	0.929481911	2.211895363	3.141377274	3.15739076	0.8242932	0.83750036	0.038894993	13.88888889
Q02156	PKC[epsilon]	AGC	PKC	0.806169881	2.125434113	2.931603994	2.929502678	0.737600885	0.76633781	0.009539703	18.66666667
Q75116	ROCK2	AGC	DMPK	0.740989402	2.253908148	2.99489755	2.929502678	0.906199966	0.873026458	0.109047201	4.4
Q15139	PKD1	CAMK	PKD	0.681359547	2.211895363	2.89326131	2.89629455	0.870418803	0.870418803	0	5
Q04759	PKC[theta]	AGC	PKC	0.670585331	2.211895363	2.882480693	2.846490011	0.712559207	0.727164518	0.04552574	20
Q15111	IKK[alpha]	Other	IKK	1.145256393	1.669570703	2.814827096	2.731422028	1.188629917	1.134331997	0.081446879	3.66666667
P31749	Akt1/PKB[alpha]	AGC	AKT	1.075983129	1.74983232	2.825818971	2.70333481	0.775382999	0.793820249	0.056664472	25.66666667
P24723	PKC[eta]	AGC	PKC	0.584603731	2.211895363	2.796490904	2.660747366	0.689785148	0.758347049	0.130041124	12.77777778
Q9HBV8	SGK2	AGC	SGK	0.647974472	2.043171592	2.614914604	2.630784143	0.734943273	0.737427449	0.059003173	16.22222222
Q16644	MAPKAPK3	CAMK	MAPKAPK	0.759497139	1.708293971	2.557766511	2.580374639	0.662117213	0.713048868	0.097607835	36.22222222
Q16566	CaMK4	CAMK	CAMK1	0.967168057	1.587861313	2.55502937	2.540607512	0.889471077	0.916601025	0.067041736	9.88888889
Q96D04	AurB/Aur1	Other	AUR	0.732054954	1.88648554	2.618540485	2.509199048	0.948215399	0.9511858	0.005894207	3.77777778
P48729	CK1[alpha]	CK1	CK1	0.384479828	1.938629534	2.321309359	2.501413791	0.622207941	0.672089457	0.134844205	9.77777778
Q14920	HK1[beta]	Other	HKK	0.585273166	1.709199111	2.294472776	2.422048872	0.816080604	0.939718846	0.177995573	3.66666667
Q15131	CKD10	CMGC	CDK	0.52272606	1.881925123	2.384651183	2.403622856	0.755243259	0.771162521	0.058261897	6.33333333
Q13131	AMPK[alpha]1	CAMK	CAMKL	0.675800333	1.669817532	2.45617865	2.402304814	0.801326584	0.796444201	0.014975291	11.44444444
P42345	mTOR/FRAP	Atypical	PIKK	0.444809069	1.993397922	2.438206991	2.394479477	0.715065264	0.710196095	0.034772163	5.88888889
Q13153	PAK1	STE	STE20	0.481946885	1.853037763	2.334984613	2.288361462	0.732701862	0.732701862	0	6
P23443	p705K	AGC	RSK	0.291064062	1.987913298	2.27897376	2.285335007	0.605088626	0.589060252	0.060990849	19.44444444
P48730	CK1[delta]	CK1	CK1	0.467785982	1.736830361	2.204616343	2.204616343	0.779624329	0.779624329	0	3
Q43930	PRYK	AGC	PKA	0.322841106	1.688794178	2.011635284	2.189229989	0.594220826	0.634288323	0.09839471	9.66666667
Q14965	AurA/Aur2	Other	AUR	0.401558416	1.853037763	2.254596179	2.142667504	0.687198605	0.727164518	0.030930451	5.66666667
P05771	PKC[beta]	AGC	PKC	0.384880985	1.853037763	2.27955868	2.142667504	0.66016695	0.66016695	0	10
Q00532	CK1[epsilon]	CMGC	CK1	0.419454077	1.72667746	2.146151537	2.111034656	0.701562133	0.693216604	0.183051972	4.8
P49674	CK1[epsilon]	CK1	CK1	0.446116973	1.919788758	2.069095732	2.06590732	0.779624329	0.779624329	NA	3
Q00537	PFTAIR2	CMGC	CDK	0.399667872	1.588948804	1.988516676	2.048468209	0.68932988	0.706134748	0.037576826	3.2
Q96538	RSKL1	AGC	RSKL	0.371928854	1.668232932	2.058161786	2.040411565	0.6862522	0.6862522	0	3
P49137	MAPKAPK2	CAMK	MAPKAPK	0.261709854	1.669817532	1.931527385	1.957030927	0.587321117	0.581365394	0.037718245	30.55555556
P41743	PKC[jota]	AGC	PKC	0.224235766	1.821434348	2.045670114	1.95093711	0.5662469	0.5662469	0.124132025	15.33333333
Q94921	PFTAIR1	CMGC	CDK	0.305218576	1.691494468	1.996713044	1.946775356	0.612498105	0.612498105	0	3
Q96017	CHK2	CAMK	RADS3	0.310116403	1.562515051	1.872631454	1.890084137	0.585350606	0.571341996	0.085919411	18.77777778
P16066	ANP[alpha]	RGC	RGC	0.125480804	1.526168022	1.651648826	1.720515571	0.510317367	0.513539499	0.030995856	21
Q05513	PKC[zeta]	AGC	PKC	0.202886374	1.484472244	1.768736395	1.644970144	0.531863242	0.54077182	0.017677334	9.22222222
Q15349	RSK1/p90RSK	AGC	RSK	0.275138246	1.347616926	1.622795173	1.642217564	0.584694537	0.584694537	0	5
Q15418	RSK3	AGC	RSK	0.227251399	1.387361756	1.614613155	1.613322716	0.552524556	0.552524556	0	9
Q14164	IKK[epsilon]	Other	IKK	0.267979539	1.329323276	1.598308215	1.5889671	0.589540889	0.589540889	0.055710793	7
Q96400	PFTAIR2	CMGC	CDK	0.169663666	1.335926485	1.505590152	1.535869334	0.463587793	0.481270414	0.027925131	6.11111111
P51812	RSK2	AGC	RSK	0.272550295	1.243002644	1.515550556	1.50177984	0.580694059	0.580694059	0	9
Q75582	MSK1	AGC	RSK	0.2134308	1.225643071	1.43907387	1.427639633	0.524812922	0.524812922	0	3
Q9U1K4	DAPK2	CAMK	DAPK	0.386026762	1.262344376	1.648371138	1.427221305	0.693710162	0.586221077	0.161233627	4.33333333
P68400	CK2[alpha]1	Other	CK2	0.139731679	1.145722313	1.284533992	1.28100362	0.415853987	0.407337985	0.025548006	4.88888889
P49841	GSK3[beta]	CMGC	GSK	0.251245986	0.998923273	1.251062959	1.271581282	0.556461119	0.555228407	0.036981316	6.88888889
P53355	DAPK1	CAMK	DAPK	0.124730375	1.106622891	1.231354664	1.231354664	0.348058328	0.348058328	0	3
P04049	RAF1	TKL	RAF	0.201985081	0.978187165	1.180172246	1.179509545	0.510098658	0.507525333	0.007719375	6.88888889
Q9H8H9	MMK2	CAMK	MAPKAPK	0.15971135	0.937153001	1.096864351	1.086050287	0.392519492	0.392519492	0	3
Q15075	DCAMKL1	CAMK	DCAMKL	0.230729556	0.852031366	1.082760923	1.063248911	0.499142901	0.499142901	0.147695756	3.5
H95819	H95K/ZC1	STE	STE20	0.222415371	1.144737357	1.364512938	1.048934608	0.353585806	0.452453284	0.124146736	5.428571429
Q13535	ATR	Atypical	PIKK	0.404042715	0.922926271	0.963068986	0.990877139	0.26762192	0.274491613	0.020450917	7.88888889
P10398	ARAF	TKL	RAF	0.128885476	0.560232026	0.689116741	0.689077329	0.328247025	0.328247025	0	3
P15056	BRAF	TKL	RAF	0.110198113	0.483808915	0.594007028	0.660230656	0.294325196	0.328247025	0.067311542	3.22222222
Q00534	CDK6	CMGC	CDK	0.088329288	0.541393974	0.629762303	0.657088027	0.352255695	0.368255287	0.047987776	6.88888889
P51955	NeK2	Other	NEK	0.187355725	0.4347001	0.622055825	0.625471606	0.429057912	0.429057912	0	3
Q76039	CDK5	CMGC	CDK1	0.072971545	0.404739811	0.477711355	0.538347641	0.29673915	0.317288191	0.047540018	6.125
Q60285	Nuak1	CAMK	CAMKL	0.061088855	0.450605928	0.511704763	0.532563575	0.214792901	0.224112888	0.020840123	4.6
Q43293	DAPK3	CAMK	DAPK	0.093881034	0.401947898	0.495828952	0.455802927	0.259533629	0.254866483	0.041001444	3.11111111
Q15264	p38[delta]	CMGC	MAPK	0.005477553	0.369712361	0.375189914	0.390704471	0.227967879	0.245198713	0.046797472	16.88888889
Q15759	p38[beta]	CMGC	MAPK	0.085203854	0.421072108	0.506273962	0.382277541	0.285779773	0.234732427	0.120877645	5.5
Q91659	RSK2	AGC	RSKL	0.112586916	0.247533956	0.360140872	0.358206707	0.297229955	0.297229955	0	3
Q00526	CDK3	CMGC	CDK	0.017421901	0.267495342	0.284917243	0.348369265	0.199309418	0.233518764	0.061203611	17.77777778
Q9U929	ICK	CMGC	RCK	0.086388472	0.902601049	0.29348862	0.340848527	0.225618887	0.225618887	0.07217911	3.33333333
P53778	p38[gamma]	CMGC	MAPK	0.034750406	0.287496745	0.322247151	0.336050439	0.251202568	0.262705833	0.061147251	10.11111111
Q13164	ERK5	CMGC	MAPK	0.020597878	0.312462579	0.33064057	0.308883129	0.239966277	0.243339634	0.043459936	12.11111111
Q14757	CHK1	CAMK	CAMKL	0.014317926	0.315036951	0.329354877	0.302265147	0.183032684	0.181027752	0.072254549	10
P49840	GSK3[alpha]	CMGC	GSK	0.066600324	0.241536836	0.30813716	0.289304306	0.254222857	0.244987914	0.026120362	4.75
P45984	JNK2	CMGC	MAPK	0.003360164	0.284813724	0.288119888	0.275947071	0.227448695	0.228171535	0.014722526	18.88

9.11. PamGene – Multiple Treatments *versus* control

Supplementary Table 2. Raw PamChip data with an MTvC analysis.

MTvC:;_clusID	UniprotAccession		MTvC:;_LogFC
1 ACM1_421_433	P11229	NA	2.41E-02
1 ACM1_444_456	P11229	NA	1.50E-02
1 ACM4_456_468	P08173	NA	-3.52E-02
1 ACM5_494_506	P08912	NA	-3.91E-02
1 ACM5_498_510	P08912	NA	8.89E-03
1 ADDB_696_708	P35612	NA	0.100581072
1 ADDB_706_718	P35612	NA	3.78E-02
1 ADRB2_338_350	P07550	NA	0.147653192
1 ANDR_785_797	P10275	NA	1.98E-02
1 ANXA1_209_221	P04083	NA	7.42E-02
1 ART_025_CXGLRRWSLGLRRRWSL	NA	NA	0.191061974
1 BAD_112_124	Q92934	NA	7.24E-02
1 BAD_69_81	Q92934	NA	2.06E-02
1 BAD_93_105	Q92934	NA	-1.12E-03
1 BCKD_45_57	Q14874	NA	-2.00E-02
1 CIR_201_213	P00736	NA	-7.38E-02
1 CA2D1_494_506	P54289	NA	1.06E-02
1 CAC1C_1974_1986	Q13936	NA	0.175549507
1 CD27_212_224	P26842	NA	7.90E-03
1 CDC2_154_169	P06493	NA	-7.18E-02
1 CDK7_163_175	P50613	NA	3.44E-02
1 CDN1A_139_151	P38936	NA	7.32E-02
1 CENPA_1_14	P49450	NA	7.09E-02
1 CFTR_730_742	P13569	NA	0.226199344
1 CFTR_761_773	P13569	NA	0.160702318
1 CGHB_109_121	P01233	NA	5.91E-02
1 CREB1_126_138	P16220	NA	0.201731116
1 CSF1R_701_713	P07333	NA	0.126329616
1 DCX_49_61	Q43602	NA	-7.03E-03
1 DESP_2842_2854	P15924	NA	0.230426982
1 E1A_ADE05_212_224	P03255	NA	0.141681284
1 EPB42_241_253	P16452	NA	0.261624515
1 ERBB2_679_691	P04626	NA	1.01E-02
1 ERF_519_531	P50548	NA	0.148583978
1 ESR1_160_172	P03372	NA	0.146335796
1 F263_454_466	Q16875	NA	0.216396719
1 FIBA_569_581	P02671	NA	9.45E-02
1 FOXO3_25_37	Q43524	NA	4.05E-02
1 FRAP_2443_2455	P42345	NA	9.05E-02
1 GBRB2_427_439	P47870	NA	0.203547284
1 GPR6_349_361	P46095	NA	1.53E-02
1 GPSM2_394_406	P81274	NA	0.251258194
1 GRIK2_708_720	Q13002	NA	0.180868909
1 GSUB_61_73	O96001	NA	-9.05E-03
1 GYS2_1_13	P54840	NA	-5.51E-03
1 H2B1B_27_40	P33778	NA	3.76E-02
1 H32_3_18	Q71D13	NA	4.25E-02
1 IF4E_203_215	P06730	NA	1.79E-02
1 KAP2_92_104	P13861	NA	0.139130786
1 KAP3_107_119	P31323	NA	0.214807898
1 KAPCG_192_206	P22612	NA	-6.28E-02
1 KCC2G_278_289	Q13555	NA	3.66E-02
1 KCNA1_438_450	Q09470	NA	0.107097909
1 KCNA2_442_454	P16389	NA	9.07E-02
1 KCNA3_461_473	P22001	NA	4.74E-02
1 KCNA6_504_516	P17658	NA	0.223352045
1 KCNB1_489_501	Q14721	NA	3.51E-02
1 KIF2C_105_118_S106G	Q99661	NA	0.221979141
1 KPB1_1011_1023	P46020	NA	0.245110035
1 KPCB_19_31_A255	P05771	NA	0.125618547
1 KPCB_626_639	P05771-2	NA	0.295580536
1 KS6A1_374_386	Q15418	NA	0.110961534
1 LIPS_944_956	Q05469	NA	0.149045378
1 LMNB1_16_28	P20700	NA	-7.58E-02
1 MARCS_152_164	P29966	NA	-4.30E-02
1 MARCS_160_172	P29966	NA	-5.53E-02
1 MBP_222_234	P02686	NA	6.25E-02
1 MP2K1_287_299	Q02750	NA	9.98E-02
1 MPIP1_172_184	P30304	NA	2.95E-02
1 MPIP3_208_220	P30307	NA	-8.26E-02
1 MYPC3_268_280	Q14896	NA	0.174093813
1 NCF1_296_308	P14598	NA	0.187909886
1 NCF1_321_333	P14598	NA	0.300800711
1 NEK2_172_184	P51955	NA	-2.44E-02
1 NEK3_158_170	P51956	NA	4.54E-03
1 NFKB1_330_342	P19838	NA	0.194599345
1 NMD21_890_902	Q05586	NA	0.142136008
1 NOS3_1171_1183	P29474	NA	-2.52E-02
1 NR4A1_344_356	P22736	NA	2.28E-02
1 PS3_12_24	P04637	NA	-0.138837144
1 PS3_308_323	P04637	NA	5.51E-02
1 PLEK_106_118	P08567	NA	3.76E-02
1 PLM_76_88	O00168	NA	5.89E-02
1 PP2AB_297_309	P62714	NA	-0.227775574
1 PPR1A_28_40	Q13522	NA	-6.14E-03
1 PRKDC_2618_2630	P78527	NA	1.82E-02
1 PTK6_436_448	Q13882	NA	0.185808748
1 PTN12_32_44	Q05209	NA	0.275445759
1 PYGL_8_20	P06737	NA	0.181282714
1 RAF1_253_265	P04049	NA	4.31E-02
1 RAP1B_172_184	P61224	NA	8.55E-02
1 RBL2_655_667	Q08999	NA	-1.79E-02
1 RB_242_254	P06400	NA	4.52E-02
1 RB_350_362	P06400	NA	3.55E-03
1 RB_803_815	P06400	NA	4.89E-03
1 REL_260_272	Q04864	NA	8.45E-02
1 RS6_228_240	P62753	NA	0.154441074
1 RYR1_4317_4329	P21817	NA	9.07E-02
1 SCN7A_898_910	Q01118	NA	0.13361302
1 STK6_283_295	O14965	NA	5.93E-02
1 STMN2_90_102	Q93045	NA	0.169755742
1 TAU_524_536	P10636	NA	-9.41E-02
1 TOP2A_1463_1475	P11388	NA	0.215184405
1 TY3H_65_77	P07101	NA	0.337294757
1 VASP_150_162	P50552	NA	0.300336927
1 VASP_232_244	P50552	NA	0.110239029
1 VASP_271_283	P50552	NA	6.45E-02
1 VTNC_390_402	P04004	NA	0.168493271

10. List of Tables and Figures

Figure 1. Liver architecture.	5
Figure 2. Liver cell types.	6
Figure 3. Fenestrae structure in LSECs.	12
Figure 4. MASLD Progression.	16
Figure 5. The semaphorin protein family and their structures.	20
Figure 6. The semaphorins and their receptors.	21
Figure 7. Formulas used for the analysis of images taken of mouse LSECs with the SEM.	33
Figure 8. Picture of Trans-Blot Turbo assembly.	37
Figure 9. CTFC calculation.	38
Figure 10. Quality assessment of MACS-isolated mouse LSECs.	45
Figure 11. Deep learning workflow development.	48
Figure 12. Cultured mouse LSECs lose fenestrae over time while SEMA3A-Fc does affect cell size or ATP content.	49
Figure 13. SEMA3A defenestrates LSECs in a concentration- and time-dependent manner.	51
Figure 14. Inhibiting the SEMA3A subdomain of NRP1 ameliorates SEMA3A-induced defenestration in mouse LSECs.	53
Figure 15. Kinase activity profiling.	55
Figure 16. SEMA3A/LIMK1/cofilin-1 pathway.	57
Figure 17. LIMK1 activity is required for SEMA3A-induced defenestration of mouse LSECs.	58
Figure 18. Effects of palmitic acid and SEMA3A-Fc on the actin-cytoskeleton in human and mouse LSECs.	60
Figure 19. Female <i>db/db</i> mice present with numerically reduced fenestrations and porosity.	62
Figure 20. Male <i>db/db</i> mice present with reduced fenestrations and porosity.	63
Figure 21. Blocking SEMA3A binding to NRP1 in <i>db/db</i> mildly affects hepatic steatosis.	65
Figure 22. Lower hepatic fat content and increased fenestrations in DIO <i>iEC^{Sema3a}</i> mice compared to DIO <i>iEC^{wt}</i> mice.	67
Figure 23. SEMA3A downstream signaling and graphical summary.	88
Table 1. Components of the liver dissociation mix. All enzymes were stored at -20°C. Volumes account for the dissociation of one liver.	27
Table 2. List of proteins used for LSEC treatment.	29
Table 3. Pipetting scheme for different concentrations of recombinant SEMA3A-Fc for a 24-well plate (500 μl).	29
Table 4. Used blocking antibodies and their concentrations.	29
Table 5. RT-qPCR primer sequences.	35

Supplementary Table 1. Raw PamGene data from the upstream kinase analysis.	109
Supplementary Table 2. Raw PamChip data with an MTvC analysis.	110
Supplementary Figure 1. F-/G-actin western blot of human LSECs treated with BSA or 0.75 mM palmitic acid.	98
Supplementary Figure 2. F-/G-actin western blot of mouse LSECs treated with 2 µg/ml IgG2a-Fc or SEMA3A- Fc.	98
Supplementary Figure 3. Western blots of mouse LSEC treated with IgG2a-Fc, SEMA3A-Fc, and LIMK i3.	99
Supplementary Figure 4. Raw SEM images.	100
Supplementary Figure 5. Deep learning workflow post-analysis script (Python).	102
Supplementary Figure 6. <i>Sema3a</i> expression in <i>db/+</i> and <i>db/db</i> mice	102
Supplementary Figure 7. Organ weights of <i>db/db</i> mice treated with NRP1 ^{SEMA3A}	103
Supplementary Figure 8. Organ weight in relation to body weight of <i>db/db</i> mice treated with NRP1 ^{SEMA3A}	104
Supplementary Figure 9. Publication license for Figure 4.	105
Supplementary Figure 10. Publication license for Figure 23a.	106
Supplementary Figure 11. Publication license for Figure 23b.	107
Supplementary Figure 12. Publication license for Figure 23b.	108

11. References

- 1 Ipsen, D. H., Lykkesfeldt, J. & Tveden-Nyborg, P. Molecular mechanisms of hepatic lipid accumulation in non-alcoholic fatty liver disease. *Cell Mol Life Sci* **75**, 3313-3327 (2018). <https://doi.org/10.1007/s00018-018-2860-6>
- 2 Michalopoulos, G. K. Liver regeneration. *J Cell Physiol* **213**, 286-300 (2007). <https://doi.org/10.1002/jcp.21172>
- 3 DeLeve, L. D. & Maretti-Mira, A. C. Liver Sinusoidal Endothelial Cell: An Update. *Semin Liver Dis* **37**, 377-387 (2017). <https://doi.org/10.1055/s-0037-1617455>
- 4 Davenport, M. Anatomy of the liver, bile ducts and pancreas. *Surgery of the Liver, Bile Ducts and Pancreas in Children*, 6 (2017).
- 5 Si-Tayeb, K., Lemaigre, F. P. & Duncan, S. A. Organogenesis and development of the liver. *Dev Cell* **18**, 175-189 (2010). <https://doi.org/10.1016/j.devcel.2010.01.011>
- 6 Watt, A. J., Battle, M. A., Li, J. X. & Duncan, S. A. GATA4 is essential for formation of the proepicardium and regulates cardiogenesis. *Proceedings of the National Academy of Sciences of the United States of America* **101**, 12573-12578 (2004). <https://doi.org/DOI.10.1073/pnas.0400752101>
- 7 Fausto, N. Liver regeneration. *J Hepatol* **32**, 19-31 (2000). [https://doi.org/10.1016/s0168-8278\(00\)80412-2](https://doi.org/10.1016/s0168-8278(00)80412-2)
- 8 Deheragoda, M. Normal Liver Anatomy and Introduction to Liver Histology. *Textbook of Pediatric Gastroenterology, Hepatology and Nutrition: A Comprehensive Guide to Practice*, 739-742 (2022).
- 9 Hijmans, B. S., Grefhorst, A., Oosterveer, M. H. & Groen, A. K. Zonation of glucose and fatty acid metabolism in the liver: mechanism and metabolic consequences. *Biochimie* **96**, 121-129 (2014). <https://doi.org/10.1016/j.biochi.2013.06.007>
- 10 Rappaport, A. & Wilson, W. The structural and functional unit in the human liver (liver acinus). *The Anatomical Record* **130**, 673-689 (1958).
- 11 Guzman, M. & Castro, J. Zonation of fatty acid metabolism in rat liver. *Biochem J* **264**, 107-113 (1989). <https://doi.org/10.1042/bj2640107>
- 12 Quistorff, B., Katz, N. & Witters, L. A. Hepatocyte heterogeneity in the metabolism of fatty acids: discrepancies on zonation of acetyl-CoA carboxylase. *Enzyme* **46**, 59-71 (1992).
- 13 Zhou, Z., Xu, M. J. & Gao, B. Hepatocytes: a key cell type for innate immunity. *Cell Mol Immunol* **13**, 301-315 (2016). <https://doi.org/10.1038/cmi.2015.97>
- 14 Soon, G. S. T. & Torbenson, M. The Liver and Glycogen: In Sickness and in Health. *Int J Mol Sci* **24** (2023). <https://doi.org/10.3390/ijms24076133>
- 15 Gupta, K. A modular analysis of bile canalicular function and its implications for cholestasis. *Am J Physiol Gastrointest Liver Physiol* **325**, G14-G22 (2023). <https://doi.org/10.1152/ajpgi.00165.2022>
- 16 Boyer, J. L. Bile formation and secretion. *Compr Physiol* **3**, 1035-1078 (2013). <https://doi.org/10.1002/cphy.c120027>
- 17 Mahadevan, V. Anatomy of the gallbladder and bile ducts. *Surgery (Oxford)* **38**, 432-436 (2020). <https://doi.org/10.1016/j.mpsur.2014.10.003>
- 18 Adin, C. A. Bilirubin as a Therapeutic Molecule: Challenges and Opportunities. *Antioxidants (Basel)* **10** (2021). <https://doi.org/10.3390/antiox10101536>
- 19 Ficht, X. & Iannaccone, M. Immune surveillance of the liver by T cells. *Sci Immunol* **5** (2020). <https://doi.org/10.1126/sciimmunol.aba2351>
- 20 Sorensen, K. K., Simon-Santamaria, J., McCuskey, R. S. & Smedsrod, B. Liver Sinusoidal Endothelial Cells. *Compr Physiol* **5**, 1751-1774 (2015). <https://doi.org/10.1002/cphy.c140078>
- 21 Basit, H., Tan, M. L. & Webster, D. R. Histology, Kupffer Cell. (2018).

- 22 Nguyen-Lefebvre, A. T. & Horuzsko, A. Kupffer Cell Metabolism and Function. *J Enzymol Metab* **1** (2015).
- 23 Dixon, L. J., Barnes, M., Tang, H., Pritchard, M. T. & Nagy, L. E. Kupffer cells in the liver. *Compr Physiol* **3**, 785-797 (2013). <https://doi.org:10.1002/cphy.c120026>
- 24 Scott, C. L. *et al.* Bone marrow-derived monocytes give rise to self-renewing and fully differentiated Kupffer cells. *Nat Commun* **7**, 10321 (2016). <https://doi.org:10.1038/ncomms10321>
- 25 Asahina, K., Zhou, B., Pu, W. T. & Tsukamoto, H. Septum transversum-derived mesothelium gives rise to hepatic stellate cells and perivascular mesenchymal cells in developing mouse liver. *Hepatology* **53**, 983-995 (2011). <https://doi.org:10.1002/hep.24119>
- 26 Puche, J. E., Saiman, Y. & Friedman, S. L. Hepatic stellate cells and liver fibrosis. *Compr Physiol* **3**, 1473-1492 (2013). <https://doi.org:10.1002/cphy.c120035>
- 27 Haubrich, W. S. Disse of the space of Disse. *Gastroenterology* **127**, 1684 (2004). <https://doi.org:10.1053/j.gastro.2004.10.021>
- 28 Winau, F. *et al.* Ito cells are liver-resident antigen-presenting cells for activating T cell responses. *Immunity* **26**, 117-129 (2007). <https://doi.org:10.1016/j.immuni.2006.11.011>
- 29 Jiang, J. X. & Torok, N. J. Liver Injury and the Activation of the Hepatic Myofibroblasts. *Curr Pathobiol Rep* **1**, 215-223 (2013). <https://doi.org:10.1007/s40139-013-0019-6>
- 30 Rockey, D. C. Hepatic blood flow regulation by stellate cells in normal and injured liver. *Semin Liver Dis* **21**, 337-349 (2001). <https://doi.org:10.1055/s-2001-17551>
- 31 Stine, J. G. & Chalasani, N. Chronic liver injury induced by drugs: a systematic review. *Liver Int* **35**, 2343-2353 (2015). <https://doi.org:10.1111/liv.12958>
- 32 Gines, P. *et al.* Liver cirrhosis. *Lancet* **398**, 1359-1376 (2021). [https://doi.org:10.1016/S0140-6736\(21\)01374-X](https://doi.org:10.1016/S0140-6736(21)01374-X)
- 33 Fausto, N. & Campbell, J. S. The role of hepatocytes and oval cells in liver regeneration and repopulation. *Mech Dev* **120**, 117-130 (2003). [https://doi.org:10.1016/s0925-4773\(02\)00338-6](https://doi.org:10.1016/s0925-4773(02)00338-6)
- 34 Knoefel, W. T. *et al.* In situ liver transection with portal vein ligation for rapid growth of the future liver remnant in two-stage liver resection. *Br J Surg* **100**, 388-394 (2013). <https://doi.org:10.1002/bjs.8955>
- 35 Grosse-Segerath, L. *et al.* Identification of myeloid-derived growth factor as a mechanically-induced, growth-promoting angiocrine signal for human hepatocytes. *Nat Commun* **15**, 1076 (2024). <https://doi.org:10.1038/s41467-024-44760-y>
- 36 Zhang, C., Sun, C., Zhao, Y., Ye, B. & Yu, G. Signaling pathways of liver regeneration: Biological mechanisms and implications. *iScience* **27**, 108683 (2024). <https://doi.org:10.1016/j.isci.2023.108683>
- 37 Stahl, W. R. Organ weights in primates and other mammals. *Science* **150**, 1039-1042 (1965).
- 38 Kruepunga, N., Hakvoort, T. B. M., Hikspoors, J., Kohler, S. E. & Lamers, W. H. Anatomy of rodent and human livers: What are the differences? *Biochim Biophys Acta Mol Basis Dis* **1865**, 869-878 (2019). <https://doi.org:10.1016/j.bbadis.2018.05.019>
- 39 Thiebaud, M. J. L., Cervantes-Alvarez, E. & Navarro-Alvarez, N. in *Liver Pathology* (IntechOpen, 2019).
- 40 Rogers, A. B. & Dintzis, R. Z. in *Comparative Anatomy and Histology* 229-239 (2018).
- 41 Cattley, R. C., Popp, J. A. & Vonderfecht, S. L. in *Toxicologic Pathology* 451-514 (CRC press, 2018).
- 42 Anstee, Q. M. & Goldin, R. D. Mouse models in non-alcoholic fatty liver disease and steatohepatitis research. *Int J Exp Pathol* **87**, 1-16 (2006). <https://doi.org:10.1111/j.0959-9673.2006.00465.x>
- 43 Perlman, R. L. Mouse models of human disease: An evolutionary perspective. *Evol Med Public Health* **2016**, 170-176 (2016). <https://doi.org:10.1093/emph/eow014>

- 44 Jiang, C. *et al.* Comparative Transcriptomics Analyses in Livers of Mice, Humans, and Humanized Mice Define Human-Specific Gene Networks. *Cells* **9** (2020). <https://doi.org:10.3390/cells9122566>
- 45 Dawson, A. The absorption of fat. *Journal of Clinical Pathology. Supplement (Royal College of Pathologists)*. **5**, 77 (1971).
- 46 Feingold, K. R. in *Endotext* (eds K. R. Feingold *et al.*) (2000).
- 47 Goldberg, I. J., Eckel, R. H. & Abumrad, N. A. Regulation of fatty acid uptake into tissues: lipoprotein lipase- and CD36-mediated pathways. *J Lipid Res* **50 Suppl**, S86-90 (2009). <https://doi.org:10.1194/jlr.R800085-JLR200>
- 48 Zilversmit, D. B. A proposal linking atherogenesis to the interaction of endothelial lipoprotein lipase with triglyceride-rich lipoproteins. *Circulation research* **33**, 633-638 (1973).
- 49 Ramos-Jimenez, A., Zavala-Lira, R. A., Moreno-Brito, V. & Gonzalez-Rodriguez, E. FAT/CD36 Participation in Human Skeletal Muscle Lipid Metabolism: A Systematic Review. *J Clin Med* **12** (2022). <https://doi.org:10.3390/jcm12010318>
- 50 Koonen, D. P., Glatz, J. F., Bonen, A. & Luiken, J. J. Long-chain fatty acid uptake and FAT/CD36 translocation in heart and skeletal muscle. *Biochim Biophys Acta* **1736**, 163-180 (2005). <https://doi.org:10.1016/j.bbaliip.2005.08.018>
- 51 Ibrahimi, A. & Abumrad, N. A. Role of CD36 in membrane transport of long-chain fatty acids. *Curr Opin Clin Nutr Metab Care* **5**, 139-145 (2002). <https://doi.org:10.1097/00075197-200203000-00004>
- 52 Zimmerman, A. W. & Veerkamp, J. H. New insights into the structure and function of fatty acid-binding proteins. *Cellular and Molecular Life Sciences* **59**, 1096-1116 (2002). <https://doi.org:DOI 10.1007/s00018-002-8490-y>
- 53 Lu, Y. C. *et al.* Circulating fatty acid-binding protein 1 (FABP1) and nonalcoholic fatty liver disease in patients with type 2 diabetes mellitus. *Int J Med Sci* **17**, 182-190 (2020). <https://doi.org:10.7150/ijms.40417>
- 54 Brocker, C. N. *et al.* Extrahepatic PPARalpha modulates fatty acid oxidation and attenuates fasting-induced hepatosteatosis in mice. *J Lipid Res* **59**, 2140-2152 (2018). <https://doi.org:10.1194/jlr.M088419>
- 55 Alves-Bezerra, M. & Cohen, D. E. Triglyceride Metabolism in the Liver. *Compr Physiol* **8**, 1-8 (2017). <https://doi.org:10.1002/cphy.c170012>
- 56 Sirwi, A. & Hussain, M. M. Lipid transfer proteins in the assembly of apoB-containing lipoproteins. *J Lipid Res* **59**, 1094-1102 (2018). <https://doi.org:10.1194/jlr.R083451>
- 57 Tiwari, S. & Siddiqi, S. A. Intracellular trafficking and secretion of VLDL. *Arterioscler Thromb Vasc Biol* **32**, 1079-1086 (2012). <https://doi.org:10.1161/ATVBAHA.111.241471>
- 58 Talley, J. T. & Mohiuddin, S. S. in *StatPearls [Internet]* (StatPearls Publishing, 2023).
- 59 Qiu, Y. Y., Zhang, J., Zeng, F. Y. & Zhu, Y. Z. Roles of the peroxisome proliferator-activated receptors (PPARs) in the pathogenesis of nonalcoholic fatty liver disease (NAFLD). *Pharmacol Res* **192**, 106786 (2023). <https://doi.org:10.1016/j.phrs.2023.106786>
- 60 Kersten, S. & Stienstra, R. The role and regulation of the peroxisome proliferator activated receptor alpha in human liver. *Biochimie* **136**, 75-84 (2017). <https://doi.org:10.1016/j.biochi.2016.12.019>
- 61 Ruppert, P. M. M. & Kersten, S. Mechanisms of hepatic fatty acid oxidation and ketogenesis during fasting. *Trends Endocrinol Metab* **35**, 107-124 (2024). <https://doi.org:10.1016/j.tem.2023.10.002>
- 62 Schwarz, J. M., Linfoot, P., Dare, D. & Aghajanian, K. Hepatic de novo lipogenesis in normoinsulinemic and hyperinsulinemic subjects consuming high-fat, low-carbohydrate and low-fat, high-carbohydrate isoenergetic diets. *Am J Clin Nutr* **77**, 43-50 (2003). <https://doi.org:10.1093/ajcn/77.1.43>

- 63 Strable, M. S. & Ntambi, J. M. Genetic control of de novo lipogenesis: role in diet-induced obesity. *Crit Rev Biochem Mol Biol* **45**, 199-214 (2010). <https://doi.org/10.3109/10409231003667500>
- 64 Dentin, R., Girard, J. & Postic, C. Carbohydrate responsive element binding protein (ChREBP) and sterol regulatory element binding protein-1c (SREBP-1c): two key regulators of glucose metabolism and lipid synthesis in liver. *Biochimie* **87**, 81-86 (2005). <https://doi.org/10.1016/j.biochi.2004.11.008>
- 65 Sanders, F. W. & Griffin, J. L. De novo lipogenesis in the liver in health and disease: more than just a shunting yard for glucose. *Biol Rev Camb Philos Soc* **91**, 452-468 (2016). <https://doi.org/10.1111/brv.12178>
- 66 Ameer, F., Scandiuizzi, L., Hasnain, S., Kalbacher, H. & Zaidi, N. De novo lipogenesis in health and disease. *Metabolism* **63**, 895-902 (2014). <https://doi.org/10.1016/j.metabol.2014.04.003>
- 67 Poisson, J. *et al.* Liver sinusoidal endothelial cells: Physiology and role in liver diseases. *J Hepatol* **66**, 212-227 (2017). <https://doi.org/10.1016/j.jhep.2016.07.009>
- 68 De Rudder, M., Dili, A., Starkel, P. & Leclercq, I. A. Critical Role of LSEC in Post-Hepatectomy Liver Regeneration and Failure. *Int J Mol Sci* **22** (2021). <https://doi.org/10.3390/ijms22158053>
- 69 DeLeve, L. D. Liver sinusoidal endothelial cells in hepatic fibrosis. *Hepatology* **61**, 1740-1746 (2015). <https://doi.org/10.1002/hep.27376>
- 70 Pandey, E., Nour, A. S. & Harris, E. N. Prominent Receptors of Liver Sinusoidal Endothelial Cells in Liver Homeostasis and Disease. *Front Physiol* **11**, 873 (2020). <https://doi.org/10.3389/fphys.2020.00873>
- 71 Bhandari, S., Larsen, A. K., McCourt, P., Smedsrod, B. & Sorensen, K. K. The Scavenger Function of Liver Sinusoidal Endothelial Cells in Health and Disease. *Front Physiol* **12**, 757469 (2021). <https://doi.org/10.3389/fphys.2021.757469>
- 72 Falkowska-Hansen, B., Falkowski, M., Metharom, P., Krunic, D. & Goerdts, S. Clathrin-coated vesicles form a unique net-like structure in liver sinusoidal endothelial cells by assembling along undisrupted microtubules. *Exp Cell Res* **313**, 1745-1757 (2007). <https://doi.org/10.1016/j.yexcr.2007.02.026>
- 73 Marrone, G., Shah, V. H. & Gracia-Sancho, J. Sinusoidal communication in liver fibrosis and regeneration. *J Hepatol* **65**, 608-617 (2016). <https://doi.org/10.1016/j.jhep.2016.04.018>
- 74 Fraser, R. *et al.* The liver sieve and atherosclerosis. *Pathology* **44**, 181-186 (2012). <https://doi.org/10.1097/PAT.0b013e328351bcc8>
- 75 Monkemoller, V. *et al.* Imaging fenestrations in liver sinusoidal endothelial cells by optical localization microscopy. *Phys Chem Chem Phys* **16**, 12576-12581 (2014). <https://doi.org/10.1039/c4cp01574f>
- 76 Zapotoczny, B. *et al.* Atomic Force Microscopy Reveals the Dynamic Morphology of Fenestrations in Live Liver Sinusoidal Endothelial Cells. *Sci Rep* **7**, 7994 (2017). <https://doi.org/10.1038/s41598-017-08555-0>
- 77 Svistounov, D. *et al.* The Relationship between fenestrations, sieve plates and rafts in liver sinusoidal endothelial cells. *PLoS One* **7**, e46134 (2012). <https://doi.org/10.1371/journal.pone.0046134>
- 78 DeLeve, L. D. Liver sinusoidal endothelial cells and liver regeneration. *J Clin Invest* **123**, 1861-1866 (2013). <https://doi.org/10.1172/JCI66025>
- 79 Wang, L. *et al.* Liver sinusoidal endothelial cell progenitor cells promote liver regeneration in rats. *J Clin Invest* **122**, 1567-1573 (2012). <https://doi.org/10.1172/JCI58789>
- 80 Furuta, K., Guo, Q., Hirsova, P. & Ibrahim, S. H. Emerging Roles of Liver Sinusoidal Endothelial Cells in Nonalcoholic Steatohepatitis. *Biology (Basel)* **9** (2020). <https://doi.org/10.3390/biology9110395>

- 81 Herrnberger, L. *et al.* Formation of fenestrae in murine liver sinusoids depends on plasmalemma vesicle-associated protein and is required for lipoprotein passage. *PLoS One* **9**, e115005 (2014). <https://doi.org:10.1371/journal.pone.0115005>
- 82 Hammoutene, A. & Rautou, P. E. Role of liver sinusoidal endothelial cells in non-alcoholic fatty liver disease. *J Hepatol* **70**, 1278-1291 (2019). <https://doi.org:10.1016/j.jhep.2019.02.012>
- 83 Fraser, R., Dobbs, B. R. & Rogers, G. W. Lipoproteins and the liver sieve: the role of the fenestrated sinusoidal endothelium in lipoprotein metabolism, atherosclerosis, and cirrhosis. *Hepatology* **21**, 863-874 (1995).
- 84 Gifre-Renom, L., Daems, M., Lutun, A. & Jones, E. A. V. Organ-Specific Endothelial Cell Differentiation and Impact of Microenvironmental Cues on Endothelial Heterogeneity. *Int J Mol Sci* **23** (2022). <https://doi.org:10.3390/ijms23031477>
- 85 Fraser, R., Heslop, V., Murray, F. & Day, W. Ultrastructural studies of the portal transport of fat in chickens. *British journal of experimental pathology* **67**, 783 (1986).
- 86 McCuskey, P., McCuskey, R. & Hinton, D. Electron microscopy of cells of the hepatic sinusoids in rainbow trout (*Salmo gairdneri*). *Cells of the Hepatic Sinusoid* **1**, 489-494 (1986).
- 87 Braet, F. & Wisse, E. Structural and functional aspects of liver sinusoidal endothelial cell fenestrae: a review. *Comp Hepatol* **1**, 1 (2002). <https://doi.org:10.1186/1476-5926-1-1>
- 88 Fraser, R., Day, W. A. & Fernando, N. S. Atherosclerosis and the Liver Sieve. *Cells of the Hepatic Sinusoid* (1986).
- 89 Furrer, K. *et al.* Serotonin reverts age-related capillarization and failure of regeneration in the liver through a VEGF-dependent pathway. *Proc Natl Acad Sci U S A* **108**, 2945-2950 (2011). <https://doi.org:10.1073/pnas.1012531108>
- 90 O'Reilly, J. N., Cogger, V. C., Fraser, R. & Le Couteur, D. G. The effect of feeding and fasting on fenestrations in the liver sinusoidal endothelial cell. *Pathology* **42**, 255-258 (2010).
- 91 Braet, F., Muller, M., Vekemans, K., Wisse, E. & Le Couteur, D. G. Antimycin A-induced defenestration in rat hepatic sinusoidal endothelial cells. *Hepatology* **38**, 394-402 (2003). <https://doi.org:10.1053/jhep.2003.50347>
- 92 Braet, F., Spector, I., De Zanger, R. & Wisse, E. A novel structure involved in the formation of liver endothelial cell fenestrae revealed by using the actin inhibitor misakinolide. *Proceedings of the National Academy of Sciences of the United States of America* **95**, 13635-13640 (1998). <https://doi.org:DOI 10.1073/pnas.95.23.13635>
- 93 Bingen, A., Gendrault, J. & Kirn, A. Cryofracture study of fenestrae formation in mouse liver endothelial cells treated with cytochalasin B. *Cells of the Hepatic Sinusoid* **2**, 466-470 (1989).
- 94 Zapotoczny, B. *et al.* Actin-spectrin scaffold supports open fenestrae in liver sinusoidal endothelial cells. *Traffic* **20**, 932-942 (2019). <https://doi.org:10.1111/tra.12700>
- 95 Szafranska, K., Kruse, L. D., Holte, C. F., McCourt, P. & Zapotoczny, B. The wHole Story About Fenestrations in LSEC. *Front Physiol* **12**, 735573 (2021). <https://doi.org:10.3389/fphys.2021.735573>
- 96 Auvinen, K. *et al.* Fenestral diaphragms and PLVAP associations in liver sinusoidal endothelial cells are developmentally regulated. *Sci Rep* **9**, 15698 (2019). <https://doi.org:10.1038/s41598-019-52068-x>
- 97 Zapotoczny, B. *et al.* Tracking Fenestrae Dynamics in Live Murine Liver Sinusoidal Endothelial Cells. *Hepatology* **69**, 876-888 (2019). <https://doi.org:10.1002/hep.30232>
- 98 Di Martino, J. *et al.* STED microscopy: A simplified method for liver sinusoidal endothelial fenestrae analysis. *Biol Cell* **110**, 159-168 (2018). <https://doi.org:10.1111/boc.201800016>
- 99 Cogger, V. C. *et al.* Three-dimensional structured illumination microscopy of liver sinusoidal endothelial cell fenestrations. *J Struct Biol* **171**, 382-388 (2010). <https://doi.org:10.1016/j.jsb.2010.06.001>
- 100 Deleve, L. D., Wang, X. & Guo, Y. Sinusoidal endothelial cells prevent rat stellate cell activation and promote reversion to quiescence. *Hepatology* **48**, 920-930 (2008). <https://doi.org:10.1002/hep.22351>

- 101 Hilmer, S. N. *et al.* Age-related changes in the hepatic sinusoidal endothelium impede lipoprotein transfer in the rat. *Hepatology* **42**, 1349-1354 (2005). <https://doi.org/10.1002/hep.20937>
- 102 Cogger, V. C. *et al.* Dietary macronutrients and the aging liver sinusoidal endothelial cell. *Am J Physiol Heart Circ Physiol* **310**, H1064-1070 (2016). <https://doi.org/10.1152/ajpheart.00949.2015>
- 103 Le Couteur, D. G., Fraser, R., Hilmer, S., Rivory, L. P. & McLean, A. J. The hepatic sinusoid in aging and cirrhosis: effects on hepatic substrate disposition and drug clearance. *Clin Pharmacokinet* **44**, 187-200 (2005). <https://doi.org/10.2165/00003088-200544020-00004>
- 104 Le Couteur, D. G., Fraser, R., Cogger, V. C. & McLean, A. J. Hepatic pseudocapillarisation and atherosclerosis in ageing. *The Lancet* **359**, 1612-1615 (2002). [https://doi.org/10.1016/s0140-6736\(02\)08524-0](https://doi.org/10.1016/s0140-6736(02)08524-0)
- 105 McLean, A. J. *et al.* Age-related pseudocapillarization of the human liver. *The Journal of Pathology: A Journal of the Pathological Society of Great Britain and Ireland* **200**, 112-117 (2003).
- 106 Huang, Q., Zou, X., Wen, X., Zhou, X. & Ji, L. NAFLD or MAFLD: Which Has Closer Association With All-Cause and Cause-Specific Mortality?-Results From NHANES III. *Front Med (Lausanne)* **8**, 693507 (2021). <https://doi.org/10.3389/fmed.2021.693507>
- 107 Rinella, M. E. *et al.* A multisociety Delphi consensus statement on new fatty liver disease nomenclature. *J Hepatol* **79**, 1542-1556 (2023). <https://doi.org/10.1016/j.jhep.2023.06.003>
- 108 Hagstrom, H. *et al.* The future of International Classification of Diseases coding in steatotic liver disease: An expert panel Delphi consensus statement. *Hepatol Commun* **8** (2024). <https://doi.org/10.1097/HC9.0000000000000386>
- 109 Jeeyavudeen, M. S., Khan, S. K. A., Fouda, S. & Pappachan, J. M. Management of metabolic-associated fatty liver disease: The diabetology perspective. *World J Gastroenterol* **29**, 126-143 (2023). <https://doi.org/10.3748/wjg.v29.i1.126>
- 110 Pouwels, S. *et al.* Non-alcoholic fatty liver disease (NAFLD): a review of pathophysiology, clinical management and effects of weight loss. *BMC Endocr Disord* **22**, 63 (2022). <https://doi.org/10.1186/s12902-022-00980-1>
- 111 Fang, T. *et al.* Mouse models of nonalcoholic fatty liver disease (NAFLD): pathomechanisms and pharmacotherapies. *Int J Biol Sci* **18**, 5681-5697 (2022). <https://doi.org/10.7150/ijbs.65044>
- 112 Younossi, Z. M. *et al.* Global epidemiology of nonalcoholic fatty liver disease-Meta-analytic assessment of prevalence, incidence, and outcomes. *Hepatology* **64**, 73-84 (2016). <https://doi.org/10.1002/hep.28431>
- 113 Teng, M. L. *et al.* Global incidence and prevalence of nonalcoholic fatty liver disease. *Clin Mol Hepatol* **29**, S32-S42 (2023). <https://doi.org/10.3350/cmh.2022.0365>
- 114 Estes, C. *et al.* Modeling NAFLD disease burden in China, France, Germany, Italy, Japan, Spain, United Kingdom, and United States for the period 2016-2030. *J Hepatol* **69**, 896-904 (2018). <https://doi.org/10.1016/j.jhep.2018.05.036>
- 115 Le, M. H. *et al.* Forecasted 2040 global prevalence of nonalcoholic fatty liver disease using hierarchical bayesian approach. *Clin Mol Hepatol* **28**, 841-850 (2022). <https://doi.org/10.3350/cmh.2022.0239>
- 116 Rich, N. E. *et al.* Racial and Ethnic Disparities in Nonalcoholic Fatty Liver Disease Prevalence, Severity, and Outcomes in the United States: A Systematic Review and Meta-analysis. *Clin Gastroenterol Hepatol* **16**, 198-210 e192 (2018). <https://doi.org/10.1016/j.cgh.2017.09.041>
- 117 Riaz, K., Swain, M. G., Congly, S. E., Kaplan, G. G. & Shaheen, A. A. Race and Ethnicity in Non-Alcoholic Fatty Liver Disease (NAFLD): A Narrative Review. *Nutrients* **14** (2022). <https://doi.org/10.3390/nu14214556>
- 118 Lonardo, A. *et al.* Sex Differences in Nonalcoholic Fatty Liver Disease: State of the Art and Identification of Research Gaps. *Hepatology* **70**, 1457-1469 (2019). <https://doi.org/10.1002/hep.30626>

- 119 Lonardo, A. & Suzuki, A. Nonalcoholic fatty liver disease: does sex matter? *Hepatobiliary Surg Nutr* **8**, 164-166 (2019). <https://doi.org/10.21037/hbsn.2018.12.04>
- 120 Salvoza, N. C., Giraudi, P. J., Tiribelli, C. & Rosso, N. Sex differences in non-alcoholic fatty liver disease: hints for future management of the disease. *Exploration of Medicine* **1**, 51-74 (2020). <https://doi.org/10.37349/emed.2020.00005>
- 121 Cherubini, A., Della Torre, S., Pelusi, S. & Valenti, L. Sexual dimorphism of metabolic dysfunction-associated steatotic liver disease. *Trends Mol Med* (2024). <https://doi.org/10.1016/j.molmed.2024.05.013>
- 122 Risi, R. *et al.* Liver disease in obesity and underweight: the two sides of the coin. A narrative review. *Eat Weight Disord* **26**, 2097-2107 (2021). <https://doi.org/10.1007/s40519-020-01060-w>
- 123 DiStefano, J. K. & Gerhard, G. S. NAFLD in normal weight individuals. *Diabetol Metab Syndr* **14**, 45 (2022). <https://doi.org/10.1186/s13098-022-00814-z>
- 124 Eslam, M., Valenti, L. & Romeo, S. Genetics and epigenetics of NAFLD and NASH: Clinical impact. *J Hepatol* **68**, 268-279 (2018). <https://doi.org/10.1016/j.jhep.2017.09.003>
- 125 Shi, F., Zhao, M., Zheng, S., Zheng, L. & Wang, H. Advances in genetic variation in metabolism-related fatty liver disease. *Front Genet* **14**, 1213916 (2023). <https://doi.org/10.3389/fgene.2023.1213916>
- 126 Sunami, Y., Rebelo, A. & Kleeff, J. Lipid Droplet-Associated Factors, PNPLA3, TM6SF2, and HSD17B Proteins in Hepatopancreatobiliary Cancer. *Cancers (Basel)* **13** (2021). <https://doi.org/10.3390/cancers13174391>
- 127 Falck-Ytter, Y., Younossi, Z. M., Marchesini, G. & McCullough, A. J. Clinical features and natural history of nonalcoholic steatosis syndromes. *Semin Liver Dis* **21**, 17-26 (2001). <https://doi.org/10.1055/s-2001-12926>
- 128 Milic, S. & Stimac, D. Nonalcoholic fatty liver disease/steatohepatitis: epidemiology, pathogenesis, clinical presentation and treatment. *Dig Dis* **30**, 158-162 (2012). <https://doi.org/10.1159/000336669>
- 129 Bacon, B. R., Farahvash, M. J., Janney, C. G. & Neuschwander-Tetri, B. A. Nonalcoholic steatohepatitis: an expanded clinical entity. *Gastroenterology* **107**, 1103-1109 (1994). [https://doi.org/10.1016/0016-5085\(94\)90235-6](https://doi.org/10.1016/0016-5085(94)90235-6)
- 130 Nalbantoglu, I. L. & Brunt, E. M. Role of liver biopsy in nonalcoholic fatty liver disease. *World J Gastroenterol* **20**, 9026-9037 (2014). <https://doi.org/10.3748/wjg.v20.i27.9026>
- 131 Tamaki, N., Ajmera, V. & Loomba, R. Non-invasive methods for imaging hepatic steatosis and their clinical importance in NAFLD. *Nat Rev Endocrinol* **18**, 55-66 (2022). <https://doi.org/10.1038/s41574-021-00584-0>
- 132 Imajo, K. *et al.* Magnetic Resonance Imaging More Accurately Classifies Steatosis and Fibrosis in Patients With Nonalcoholic Fatty Liver Disease Than Transient Elastography. *Gastroenterology* **150**, 626-637 e627 (2016). <https://doi.org/10.1053/j.gastro.2015.11.048>
- 133 Zou, Y., Zhong, L., Hu, C. & Sheng, G. Association between the alanine aminotransferase/aspartate aminotransferase ratio and new-onset non-alcoholic fatty liver disease in a nonobese Chinese population: a population-based longitudinal study. *Lipids Health Dis* **19**, 245 (2020). <https://doi.org/10.1186/s12944-020-01419-z>
- 134 Festi, D. *et al.* Hepatic steatosis in obese patients: clinical aspects and prognostic significance. *Obes Rev* **5**, 27-42 (2004). <https://doi.org/10.1111/j.1467-789x.2004.00126.x>
- 135 Wan, Y. *et al.* Endothelial dysfunction in pathological processes of chronic liver disease during aging. *FASEB J* **36**, e22125 (2022). <https://doi.org/10.1096/fj.202101426R>
- 136 Gracia-Sancho, J., Caparros, E., Fernandez-Iglesias, A. & Frances, R. Role of liver sinusoidal endothelial cells in liver diseases. *Nat Rev Gastroenterol Hepatol* **18**, 411-431 (2021). <https://doi.org/10.1038/s41575-020-00411-3>
- 137 Musso, G., Cassader, M. & Gambino, R. Non-alcoholic steatohepatitis: emerging molecular targets and therapeutic strategies. *Nat Rev Drug Discov* **15**, 249-274 (2016). <https://doi.org/10.1038/nrd.2015.3>

- 138 Begrich, K., Igoudjil, A., Pessayre, D. & Fromenty, B. Mitochondrial dysfunction in NASH: causes, consequences and possible means to prevent it. *Mitochondrion* **6**, 1-28 (2006). <https://doi.org:10.1016/j.mito.2005.10.004>
- 139 Mathurin, P. *et al.* Prospective study of the long-term effects of bariatric surgery on liver injury in patients without advanced disease. *Gastroenterology* **137**, 532-540 (2009). <https://doi.org:10.1053/j.gastro.2009.04.052>
- 140 Mao, Y., Yu, F., Wang, J., Guo, C. & Fan, X. Autophagy: a new target for nonalcoholic fatty liver disease therapy. *Hepat Med* **8**, 27-37 (2016). <https://doi.org:10.2147/HMER.S98120>
- 141 Burt, A. D., Lackner, C. & Tiniakos, D. G. Diagnosis and Assessment of NAFLD: Definitions and Histopathological Classification. *Semin Liver Dis* **35**, 207-220 (2015). <https://doi.org:10.1055/s-0035-1562942>
- 142 Li, H. *et al.* Crosstalk Between Liver Macrophages and Surrounding Cells in Nonalcoholic Steatohepatitis. *Front Immunol* **11**, 1169 (2020). <https://doi.org:10.3389/fimmu.2020.01169>
- 143 Thibaut, R. *et al.* Liver macrophages and inflammation in physiology and physiopathology of non-alcoholic fatty liver disease. *FEBS J* **289**, 3024-3057 (2022). <https://doi.org:10.1111/febs.15877>
- 144 Neuman, M. G., Cohen, L. B. & Nanau, R. M. Biomarkers in nonalcoholic fatty liver disease. *Can J Gastroenterol Hepatol* **28**, 607-618 (2014). <https://doi.org:10.1155/2014/757929>
- 145 Fernando, D. H., Forbes, J. M., Angus, P. W. & Herath, C. B. Development and Progression of Non-Alcoholic Fatty Liver Disease: The Role of Advanced Glycation End Products. *Int J Mol Sci* **20** (2019). <https://doi.org:10.3390/ijms20205037>
- 146 Buzzetti, E., Pinzani, M. & Tsochatzis, E. A. The multiple-hit pathogenesis of non-alcoholic fatty liver disease (NAFLD). *Metabolism* **65**, 1038-1048 (2016). <https://doi.org:10.1016/j.metabol.2015.12.012>
- 147 Daher, S. *et al.* Portal lymphadenopathy predicts non-alcoholic steatohepatitis and advanced fibrosis in non-alcoholic fatty liver disease. *PLoS One* **13**, e0207479 (2018). <https://doi.org:10.1371/journal.pone.0207479>
- 148 Tarantino, G. & Finelli, C. Pathogenesis of hepatic steatosis: the link between hypercortisolism and non-alcoholic fatty liver disease. *World J Gastroenterol* **19**, 6735-6743 (2013). <https://doi.org:10.3748/wjg.v19.i40.6735>
- 149 Bruha, R., Vitek, L. & Smid, V. Osteopontin - A potential biomarker of advanced liver disease. *Ann Hepatol* **19**, 344-352 (2020). <https://doi.org:10.1016/j.aohep.2020.01.001>
- 150 Wen, Y., Jeong, S., Xia, Q. & Kong, X. Role of Osteopontin in Liver Diseases. *Int J Biol Sci* **12**, 1121-1128 (2016). <https://doi.org:10.7150/ijbs.16445>
- 151 Arriazu, E. *et al.* Signalling via the osteopontin and high mobility group box-1 axis drives the fibrogenic response to liver injury. *Gut* **66**, 1123-1137 (2017). <https://doi.org:10.1136/gutjnl-2015-310752>
- 152 Brown, L. F. *et al.* Expression and distribution of osteopontin in human tissues: widespread association with luminal epithelial surfaces. *Mol Biol Cell* **3**, 1169-1180 (1992). <https://doi.org:10.1091/mbc.3.10.1169>
- 153 Friedman, S. L., Neuschwander-Tetri, B. A., Rinella, M. & Sanyal, A. J. Mechanisms of NAFLD development and therapeutic strategies. *Nat Med* **24**, 908-922 (2018). <https://doi.org:10.1038/s41591-018-0104-9>
- 154 Schattenberg, J. M., Schuchmann, M. & Galle, P. R. Cell death and hepatocarcinogenesis: Dysregulation of apoptosis signaling pathways. *J Gastroenterol Hepatol* **26 Suppl 1**, 213-219 (2011). <https://doi.org:10.1111/j.1440-1746.2010.06582.x>
- 155 Shipley, L. C., Axley, P. D. & Singal, A. K. Liver Fibrosis: A Clinical Update. *European Medical Journal* (2019).
- 156 Sun, M. & Kisseleva, T. Reversibility of liver fibrosis. *Clin Res Hepatol Gastroenterol* **39 Suppl 1**, S60-63 (2015). <https://doi.org:10.1016/j.clinre.2015.06.015>

- 157 Dezso, K., Paku, S., Kobori, L., Thorgeirsson, S. S. & Nagy, P. What Makes Cirrhosis Irreversible?-Consideration on Structural Changes. *Front Med (Lausanne)* **9**, 876293 (2022). <https://doi.org/10.3389/fmed.2022.876293>
- 158 Fallowfield, J. & Hayes, P. Pathogenesis and treatment of hepatic fibrosis: is cirrhosis reversible? *Clinical Medicine* **11** (2011).
- 159 Premkumar, M. & Anand, A. C. Overview of Complications in Cirrhosis. *J Clin Exp Hepatol* **12**, 1150-1174 (2022). <https://doi.org/10.1016/j.jceh.2022.04.021>
- 160 Goldberg, D. *et al.* Accurate long-term prediction of death for patients with cirrhosis. *Hepatology* **76**, 700-711 (2022). <https://doi.org/10.1002/hep.32457>
- 161 Wedd, J. *et al.* Stage of cirrhosis predicts the risk of liver-related death in patients with low Model for End-Stage Liver Disease scores and cirrhosis awaiting liver transplantation. *Liver Transpl* **20**, 1193-1201 (2014). <https://doi.org/10.1002/lt.23929>
- 162 Chang, Y. & Li, H. Hepatic Antifibrotic Pharmacotherapy: Are We Approaching Success? *J Clin Transl Hepatol* **8**, 222-229 (2020). <https://doi.org/10.14218/JCTH.2020.00026>
- 163 Shan, L. *et al.* New Drugs for Hepatic Fibrosis. *Front Pharmacol* **13**, 874408 (2022). <https://doi.org/10.3389/fphar.2022.874408>
- 164 Khalil, A. *et al.* New Developments and Challenges in Liver Transplantation. *J Clin Med* **12** (2023). <https://doi.org/10.3390/jcm12175586>
- 165 Arulraj, R. & Neuberger, J. Liver transplantation: filling the gap between supply and demand. *Clinical Medicine* **11**, 194-198 (2011). <https://doi.org/DOI.10.7861/clinmedicine.11-2-194>
- 166 Anstee, Q. M., Reeves, H. L., Kotsiliti, E., Govaere, O. & Heikenwalder, M. From NASH to HCC: current concepts and future challenges. *Nat Rev Gastroenterol Hepatol* **16**, 411-428 (2019). <https://doi.org/10.1038/s41575-019-0145-7>
- 167 Meyer, L. F., Musante, C. J. & Allen, R. A continuous-time Markov chain model of fibrosis progression in NAFLD and NASH. *Front Med (Lausanne)* **10**, 1130890 (2023). <https://doi.org/10.3389/fmed.2023.1130890>
- 168 Loomba, R. *et al.* Nonalcoholic fatty liver disease progression rates to cirrhosis and progression of cirrhosis to decompensation and mortality: a real world analysis of Medicare data. *Aliment Pharmacol Ther* **51**, 1149-1159 (2020). <https://doi.org/10.1111/apt.15679>
- 169 Lekakis, V. & Papatheodoridis, G. V. Natural history of metabolic dysfunction-associated steatotic liver disease. *Eur J Intern Med* **122**, 3-10 (2024). <https://doi.org/10.1016/j.ejim.2023.11.005>
- 170 Toubert, C. *et al.* Prolonged Survival after Recurrence in HCC Resected Patients Using Repeated Curative Therapies: Never Give Up! *Cancers (Basel)* **15** (2022). <https://doi.org/10.3390/cancers15010232>
- 171 Marrero, J. A. *et al.* Diagnosis, Staging, and Management of Hepatocellular Carcinoma: 2018 Practice Guidance by the American Association for the Study of Liver Diseases. *Hepatology* **68**, 723-750 (2018). <https://doi.org/10.1002/hep.29913>
- 172 Giannini, E. G. *et al.* Prognosis of untreated hepatocellular carcinoma. *Hepatology* **61**, 184-190 (2015). <https://doi.org/10.1002/hep.27443>
- 173 Armandi, A. & Bugianesi, E. Dietary and pharmacological treatment in patients with metabolic-dysfunction associated steatotic liver disease. *Eur J Intern Med* **122**, 20-27 (2024). <https://doi.org/10.1016/j.ejim.2024.01.005>
- 174 Aronne, L. J. *et al.* Continued Treatment With Tirzepatide for Maintenance of Weight Reduction in Adults With Obesity. *Jama* **331** (2024). <https://doi.org/10.1001/jama.2023.24945>
- 175 Frias, J. P. *et al.* Tirzepatide versus Semaglutide Once Weekly in Patients with Type 2 Diabetes. *New England Journal of Medicine* **385**, 503-515 (2021). <https://doi.org/10.1056/NEJMoa2107519>
- 176 Lincoff, A. M. *et al.* Semaglutide and Cardiovascular Outcomes in Obesity without Diabetes. *N Engl J Med* **389**, 2221-2232 (2023). <https://doi.org/10.1056/NEJMoa2307563>

- 177 Husain, M. *et al.* Oral Semaglutide and Cardiovascular Outcomes in Patients with Type 2 Diabetes. *N Engl J Med* **381**, 841-851 (2019). <https://doi.org:10.1056/NEJMoa1901118>
- 178 Wang, M. Y., Prabakar, K., Gaman, M. A. & Zhang, J. L. Vitamin E supplementation in the treatment on nonalcoholic fatty liver disease (NAFLD): Evidence from an umbrella review of meta-analysis on randomized controlled trials. *J Dig Dis* **24**, 380-389 (2023). <https://doi.org:10.1111/1751-2980.13210>
- 179 Aishwarya, T. S., Mounika, N., Vishwakarma, G. & Adela, R. Effect of obeticholic acid in non-alcoholic fatty liver disease (NAFLD) and non-alcoholic steatohepatitis (NASH) patients: a systematic review and meta-analysis. *RPS Pharmacy and Pharmacology Reports* **1** (2022). <https://doi.org:10.1093/rpsppr/rqac001>
- 180 Gadaleta, R. M. *et al.* Farnesoid X receptor activation inhibits inflammation and preserves the intestinal barrier in inflammatory bowel disease. *Gut* **60**, 463-472 (2011). <https://doi.org:10.1136/gut.2010.212159>
- 181 Fiorucci, S. *et al.* The nuclear receptor SHP mediates inhibition of hepatic stellate cells by FXR and protects against liver fibrosis. *Gastroenterology* **127**, 1497-1512 (2004). <https://doi.org:10.1053/j.gastro.2004.08.001>
- 182 Younossi, Z. M. *et al.* Obeticholic acid for the treatment of non-alcoholic steatohepatitis: interim analysis from a multicentre, randomised, placebo-controlled phase 3 trial. *Lancet* **394**, 2184-2196 (2019). [https://doi.org:10.1016/S0140-6736\(19\)33041-7](https://doi.org:10.1016/S0140-6736(19)33041-7)
- 183 Harrison, S. A. *et al.* A Phase 3, Randomized, Controlled Trial of Resmetirom in NASH with Liver Fibrosis. *N Engl J Med* **390**, 497-509 (2024). <https://doi.org:10.1056/NEJMoa2309000>
- 184 Keam, S. J. Resmetirom: First Approval. *Drugs* **84**, 729-735 (2024). <https://doi.org:10.1007/s40265-024-02045-0>
- 185 Shetty, S., Lalor, P. F. & Adams, D. H. Liver sinusoidal endothelial cells - gatekeepers of hepatic immunity. *Nat Rev Gastroenterol Hepatol* **15**, 555-567 (2018). <https://doi.org:10.1038/s41575-018-0020-y>
- 186 Wang, X. K. & Peng, Z. G. Targeting Liver Sinusoidal Endothelial Cells: An Attractive Therapeutic Strategy to Control Inflammation in Nonalcoholic Fatty Liver Disease. *Front Pharmacol* **12**, 655557 (2021). <https://doi.org:10.3389/fphar.2021.655557>
- 187 Nasiri-Ansari, N. *et al.* Endothelial Cell Dysfunction and Nonalcoholic Fatty Liver Disease (NAFLD): A Concise Review. *Cells* **11** (2022). <https://doi.org:10.3390/cells11162511>
- 188 Coelho, I., Duarte, N., Macedo, M. P. & Penha-Gonçalves, C. Insights into Macrophage/Monocyte-Endothelial Cell Crosstalk in the Liver: A Role for Trem-2. *Journal of Clinical Medicine* **10** (2021). <https://doi.org:10.3390/jcm10061248>
- 189 Du, W. & Wang, L. The Crosstalk Between Liver Sinusoidal Endothelial Cells and Hepatic Microenvironment in NASH Related Liver Fibrosis. *Front Immunol* **13**, 936196 (2022). <https://doi.org:10.3389/fimmu.2022.936196>
- 190 Reeves, H. L. & Friedman, S. L. Activation of hepatic stellate cells - A key issue in liver fibrosis. *Frontiers in Bioscience-Landmark* **7**, D808-D826 (2002). <https://doi.org:DOI 10.2741/reeves>
- 191 Kaur, S. *et al.* Increased number and function of endothelial progenitor cells stimulate angiogenesis by resident liver sinusoidal endothelial cells (SECs) in cirrhosis through paracrine factors. *J Hepatol* **57**, 1193-1198 (2012). <https://doi.org:10.1016/j.jhep.2012.07.016>
- 192 Velliou, R.-I., Legaki, A.-I., Nikolakopoulou, P., Vlachogiannis, N. I. & Chatzigeorgiou, A. Liver endothelial cells in NAFLD and transition to NASH and HCC. *Cellular and Molecular Life Sciences* **80** (2023). <https://doi.org:10.1007/s00018-023-04966-7>
- 193 Geraud, C. *et al.* Endothelial transdifferentiation in hepatocellular carcinoma: loss of Stabilin-2 expression in peri-tumourous liver correlates with increased survival. *Liver Int* **33**, 1428-1440 (2013). <https://doi.org:10.1111/liv.12262>
- 194 Passi, M. & Zahler, S. Mechano-Signaling Aspects of Hepatocellular Carcinoma. *J Cancer* **12**, 6411-6421 (2021). <https://doi.org:10.7150/jca.60102>

- 195 Benedicto, A. *et al.* Liver sinusoidal endothelial cell ICAM-1 mediated tumor/endothelial crosstalk drives the development of liver metastasis by initiating inflammatory and angiogenic responses. *Sci Rep* **9**, 13111 (2019). <https://doi.org/10.1038/s41598-019-49473-7>
- 196 Yazdani, U. & Terman, J. R. The semaphorins. *Genome Biol* **7**, 211 (2006). <https://doi.org/10.1186/gb-2006-7-3-211>
- 197 Kolodkin, A. *et al.* Fasciclin IV: Sequence, Expression, and Function during Growth Cone Guidance in the Grasshopper Embryo. *Neuron* **9**, 831-845 (1993).
- 198 Gherardi, E., Love, C. A., Esnouf, R. M. & Jones, E. Y. The sema domain. *Curr Opin Struct Biol* **14**, 669-678 (2004). <https://doi.org/10.1016/j.sbi.2004.10.010>
- 199 Kozlov, G. *et al.* Insights into function of PSI domains from structure of the Met receptor PSI domain. *Biochem Biophys Res Commun* **321**, 234-240 (2004). <https://doi.org/10.1016/j.bbrc.2004.06.132>
- 200 Treppe, L., Le Guelte, A. & Gavard, J. Emerging roles of Semaphorins in the regulation of epithelial and endothelial junctions. *Tissue Barriers* **1**, e23272 (2013). <https://doi.org/10.4161/tisb.23272>
- 201 Nakamura, F., Kalb, R. G. & Strittmatter, S. M. Molecular basis of semaphorin-mediated axon guidance. *J Neurobiol* **44**, 219-229 (2000). [https://doi.org/10.1002/1097-4695\(200008\)44:2<219::aid-neu11>3.0.co;2-w](https://doi.org/10.1002/1097-4695(200008)44:2<219::aid-neu11>3.0.co;2-w)
- 202 Jiao, B. *et al.* Class-3 semaphorins: Potent multifunctional modulators for angiogenesis-associated diseases. *Biomed Pharmacother* **137**, 111329 (2021). <https://doi.org/10.1016/j.biopha.2021.111329>
- 203 Negishi, M., Oinuma, I. & Katoh, H. Plexins: axon guidance and signal transduction. *Cell Mol Life Sci* **62**, 1363-1371 (2005). <https://doi.org/10.1007/s00018-005-5018-2>
- 204 Junqueira Alves, C., Yotoko, K., Zou, H. & Friedel, R. H. Origin and evolution of plexins, semaphorins, and Met receptor tyrosine kinases. *Sci Rep* **9**, 1970 (2019). <https://doi.org/10.1038/s41598-019-38512-y>
- 205 Zhang, X., Shao, S. & Li, L. Characterization of Class-3 Semaphorin Receptors, Neuropilins and Plexins, as Therapeutic Targets in a Pan-Cancer Study. *Cancers (Basel)* **12** (2020). <https://doi.org/10.3390/cancers12071816>
- 206 Valdembri, D., Regano, D., Maione, F., Giraudo, E. & Serini, G. Class 3 semaphorins in cardiovascular development. *Cell Adh Migr* **10**, 641-651 (2016). <https://doi.org/10.1080/19336918.2016.1212805>
- 207 Nogi, T. *et al.* Structural basis for semaphorin signalling through the plexin receptor. *Nature* **467**, 1123-1127 (2010). <https://doi.org/10.1038/nature09473>
- 208 Sharma, A., Verhaagen, J. & Harvey, A. R. Receptor complexes for each of the Class 3 Semaphorins. *Front Cell Neurosci* **6**, 28 (2012). <https://doi.org/10.3389/fncel.2012.00028>
- 209 Zhou, Y., Gunput, R. A. & Pasterkamp, R. J. Semaphorin signaling: progress made and promises ahead. *Trends Biochem Sci* **33**, 161-170 (2008). <https://doi.org/10.1016/j.tibs.2008.01.006>
- 210 Jackson, R. E. & Eickholt, B. J. Semaphorin signalling. *Curr Biol* **19**, R504-507 (2009). <https://doi.org/10.1016/j.cub.2009.04.055>
- 211 Jongbloets, B. C. & Pasterkamp, R. J. Semaphorin signalling during development. *Development* **141**, 3292-3297 (2014). <https://doi.org/10.1242/dev.105544>
- 212 Roth, L. *et al.* The many faces of semaphorins: from development to pathology. *Cell Mol Life Sci* **66**, 649-666 (2009). <https://doi.org/10.1007/s00018-008-8518-z>
- 213 Epstein, J. A., Aghajanian, H. & Singh, M. K. Semaphorin signaling in cardiovascular development. *Cell Metab* **21**, 163-173 (2015). <https://doi.org/10.1016/j.cmet.2014.12.015>
- 214 Schmidt, E. F., Togashi, H. & Strittmatter, S. M. in *Handbook of Cell Signaling* 1961-1966 (Elsevier, 2010).

- 215 Carulli, D., de Winter, F. & Verhaagen, J. Semaphorins in Adult Nervous System Plasticity and Disease. *Front Synaptic Neurosci* **13**, 672891 (2021). <https://doi.org/10.3389/fnsyn.2021.672891>
- 216 Takegahara, N. & Kumanogoh, A. Involvement of semaphorins and their receptors in neurological diseases. *Clinical and Experimental Neuroimmunology* **1**, 33-45 (2010). <https://doi.org/10.1111/j.1759-1961.2009.00004.x>
- 217 Kanth, S. M., Gairhe, S. & Torabi-Parizi, P. The Role of Semaphorins and Their Receptors in Innate Immune Responses and Clinical Diseases of Acute Inflammation. *Front Immunol* **12**, 672441 (2021). <https://doi.org/10.3389/fimmu.2021.672441>
- 218 Luo, Y. L., Raible, D. & Raper, J. A. Collapsin - a Protein in Brain That Induces the Collapse and Paralysis of Neuronal Growth Cones. *Cell* **75**, 217-227 (1993). [https://doi.org/10.1016/0092-8674\(93\)80064-L](https://doi.org/10.1016/0092-8674(93)80064-L)
- 219 Tamagnone, L. & Comoglio, P. M. Signalling by semaphorin receptors: cell guidance and beyond. *Trends Cell Biol* **10**, 377-383 (2000). [https://doi.org/10.1016/s0962-8924\(00\)01816-x](https://doi.org/10.1016/s0962-8924(00)01816-x)
- 220 Fujisawa, H. Discovery of semaphorin receptors, neuropilin and plexin, and their functions in neural development. *J Neurobiol* **59**, 24-33 (2004). <https://doi.org/10.1002/neu.10337>
- 221 Aizawa, H. *et al.* Phosphorylation of cofilin by LIM-kinase is necessary for semaphorin 3A-induced growth cone collapse. *Nature Neuroscience* **4**, 367-373 (2001). <https://doi.org/10.1038/86011>
- 222 Hayashi, M. *et al.* Osteoprotection by semaphorin 3A. *Nature* **485**, 69-74 (2012). <https://doi.org/10.1038/nature11000>
- 223 Pan, Q. *et al.* Blocking neuropilin-1 function has an additive effect with anti-VEGF to inhibit tumor growth. *Cancer Cell* **11**, 53-67 (2007). <https://doi.org/10.1016/j.ccr.2006.10.018>
- 224 Palodetto, B. *et al.* SEMA3A partially reverses VEGF effects through binding to neuropilin-1. *Stem Cell Res* **22**, 70-78 (2017). <https://doi.org/10.1016/j.scr.2017.05.012>
- 225 Vieira, J. M., Schwarz, Q. & Ruhrberg, C. Role of the neuropilin ligands VEGF164 and SEMA3A in neuronal and vascular patterning in the mouse. *Novartis Found Symp* **283**, 230-235; discussion 235-241 (2007). <https://doi.org/10.1002/9780470319413.ch18>
- 226 Bender, R. J. & Mac Gabhann, F. Dysregulation of the vascular endothelial growth factor and semaphorin ligand-receptor families in prostate cancer metastasis. *BMC Syst Biol* **9**, 55 (2015). <https://doi.org/10.1186/s12918-015-0201-z>
- 227 Bachelder, R. E. *et al.* Competing autocrine pathways involving alternative neuropilin-1 ligands regulate chemotaxis of carcinoma cells. *Cancer Res* **63**, 5230-5233 (2003).
- 228 Sang, Y. *et al.* Semaphorin3A inhibitor ameliorates renal fibrosis through the regulation of JNK signaling. *Am J Physiol Renal Physiol* **321**, F740-F756 (2021). <https://doi.org/10.1152/ajprenal.00234.2021>
- 229 Lu, Q. & Zhu, L. The Role of Semaphorins in Metabolic Disorders. *Int J Mol Sci* **21** (2020). <https://doi.org/10.3390/ijms21165641>
- 230 Aggarwal, P. K. *et al.* Semaphorin3a promotes advanced diabetic nephropathy. *Diabetes* **64**, 1743-1759 (2015). <https://doi.org/10.2337/db14-0719>
- 231 Cerani, A. *et al.* Neuron-derived semaphorin 3A is an early inducer of vascular permeability in diabetic retinopathy via neuropilin-1. *Cell Metab* **18**, 505-518 (2013). <https://doi.org/10.1016/j.cmet.2013.09.003>
- 232 Sang, Y. *et al.* Semaphorin3A-Inhibitor Ameliorates Doxorubicin-Induced Podocyte Injury. *Int J Mol Sci* **21** (2020). <https://doi.org/10.3390/ijms21114099>
- 233 Zhang, X., Klamer, B., Li, J., Fernandez, S. & Li, L. A pan-cancer study of class-3 semaphorins as therapeutic targets in cancer. *BMC Med Genomics* **13**, 45 (2020). <https://doi.org/10.1186/s12920-020-0682-5>
- 234 Yamada, D., Kawahara, K. & Maeda, T. mTORC1 is a critical mediator of oncogenic Semaphorin3A signaling. *Biochem Biophys Res Commun* **476**, 475-480 (2016). <https://doi.org/10.1016/j.bbrc.2016.05.147>

- 235 Butti, R., Kumar, T. V., Nimma, R. & Kundu, G. C. Impact of semaphorin expression on prognostic characteristics in breast cancer. *Breast Cancer (Dove Med Press)* **10**, 79-88 (2018). <https://doi.org/10.2147/BCTT.S135753>
- 236 Andryszak, N. *et al.* Expression of semaphorin 3A (SEMA3A) in breast cancer subtypes. *Sci Rep* **14**, 1969 (2024). <https://doi.org/10.1038/s41598-024-51796-z>
- 237 Kanemaru, H., Yamada, Y., Ohazama, A., Maeda, T. & Seo, K. Semaphorin 3A Inhibits Nerve Regeneration During Early Stage after Inferior Alveolar Nerve Transection. *Sci Rep* **9**, 4245 (2019). <https://doi.org/10.1038/s41598-018-37819-6>
- 238 Zhang, L. *et al.* Rewiring of regenerated axons by combining treadmill training with semaphorin3A inhibition. *Mol Brain* **7**, 14 (2014). <https://doi.org/10.1186/1756-6606-7-14>
- 239 Kaneko, S. *et al.* A selective Sema3A inhibitor enhances regenerative responses and functional recovery of the injured spinal cord. *Nat Med* **12**, 1380-1389 (2006). <https://doi.org/10.1038/nm1505>
- 240 Hou, S. T. *et al.* Semaphorin3A elevates vascular permeability and contributes to cerebral ischemia-induced brain damage. *Sci Rep* **5**, 7890 (2015). <https://doi.org/10.1038/srep07890>
- 241 Fu, L. Interplay of neuropilin-1 and semaphorin 3A after partial hepatectomy in rats. *World Journal of Gastroenterology* **18** (2012). <https://doi.org/10.3748/wjg.v18.i36.5034>
- 242 Samadan, L. *et al.* Do Semaphorins Play a Role in Development of Fibrosis in Patients with Nonalcoholic Fatty Liver Disease? *Biomedicines* **10** (2022). <https://doi.org/10.3390/biomedicines10123014>
- 243 Li, X. *et al.* Novel role of semaphorin 3A in the growth and progression of hepatocellular carcinoma. *Oncol Rep* **37**, 3313-3320 (2017). <https://doi.org/10.3892/or.2017.5616>
- 244 Bouvree, K. *et al.* Semaphorin3A, Neuropilin-1, and PlexinA1 are required for lymphatic valve formation. *Circ Res* **111**, 437-445 (2012). <https://doi.org/10.1161/CIRCRESAHA.112.269316>
- 245 Ricci, M. *et al.* Review of the Function of *SEMA3A* in Lymphatic Vessel Maturation and Its Potential as a Candidate Gene for Lymphedema: Analysis of Three Families with Rare Causative Variants. *Lymphology* **53**, 63-75 (2020).
- 246 Molica, F. *et al.* Pannexin1 links lymphatic function to lipid metabolism and atherosclerosis. *Sci Rep* **7**, 13706 (2017). <https://doi.org/10.1038/s41598-017-14130-4>
- 247 Eberhard, D. *et al.* Semaphorin-3A regulates liver sinusoidal endothelial cell porosity and promotes hepatic steatosis. *Nature Cardiovascular Research* **3**, 734-753 (2024). <https://doi.org/10.1038/s44161-024-00487-z>
- 248 Upschulte, E., Harmeling, S., Amunts, K. & Dickscheid, T. Contour proposal networks for biomedical instance segmentation. *Med Image Anal* **77**, 102371 (2022). <https://doi.org/10.1016/j.media.2022.102371>
- 249 Upschulte, E., Harmeling, S., Amunts, K. & Dickscheid, T. in *Competitions in Neural Information Processing Systems*. 1-12 (PMLR).
- 250 Ronneberger, O., Fischer, P. and Brox, T. in *Medical image computing and computer-assisted intervention—MICCAI 2015: 18th international conference* 234-241 (Springer International Publishing, Munich, Germany, 2015).
- 251 Xie, S., Girshick, R., Dollár, P., Tu, Z. & He, K. in *Proceedings of the IEEE conference on computer vision and pattern recognition*. 1492-1500.
- 252 Alvarez, D. JUWELS Cluster and Booster: Exascale Pathfinder with Modular Supercomputing Architecture at Juelich Supercomputing Centre. *Journal of large-scale research facilities JLSRF* **7** (2021). <https://doi.org/10.17815/jlsrf-7-183>
- 253 Schindelin, J. *et al.* Fiji: an open-source platform for biological-image analysis. *Nat Methods* **9**, 676-682 (2012). <https://doi.org/10.1038/nmeth.2019>
- 254 Arganda-Carreras, I. *et al.* Trainable Weka Segmentation: a machine learning tool for microscopy pixel classification. *Bioinformatics* **33**, 2424-2426 (2017). <https://doi.org/10.1093/bioinformatics/btx180>

- 255 Schmittgen, T. D. & Livak, K. J. Analyzing real-time PCR data by the comparative C(T) method. *Nat Protoc* **3**, 1101-1108 (2008). <https://doi.org:10.1038/nprot.2008.73>
- 256 Bora, P. *et al.* p38-MAPK-mediated translation regulation during early blastocyst development is required for primitive endoderm differentiation in mice. *Commun Biol* **4**, 788 (2021). <https://doi.org:10.1038/s42003-021-02290-z>
- 257 Wang, Y. *et al.* Ephrin-B2 controls VEGF-induced angiogenesis and lymphangiogenesis. *Nature* **465**, 483-486 (2010). <https://doi.org:10.1038/nature09002>
- 258 Taniguchi, M. *et al.* Disruption of semaphorin III/D gene causes severe abnormality in peripheral nerve projection. *Neuron* **19**, 519-530 (1997). [https://doi.org:10.1016/s0896-6273\(00\)80368-2](https://doi.org:10.1016/s0896-6273(00)80368-2)
- 259 Licht, A. H., Raab, S., Hofmann, U. & Breier, G. Endothelium-specific Cre recombinase activity in flk-1-Cre transgenic mice. *Dev Dyn* **229**, 312-318 (2004). <https://doi.org:10.1002/dvdy.10416>
- 260 Madisen, L. *et al.* A robust and high-throughput Cre reporting and characterization system for the whole mouse brain. *Nat Neurosci* **13**, 133-140 (2010). <https://doi.org:10.1038/nn.2467>
- 261 Cogger, V. C., O'Reilly, J. N., Warren, A. & Le Couteur, D. G. A standardized method for the analysis of liver sinusoidal endothelial cells and their fenestrations by scanning electron microscopy. *J Vis Exp*, e52698 (2015). <https://doi.org:10.3791/52698>
- 262 Martinez, I. *et al.* The influence of oxygen tension on the structure and function of isolated liver sinusoidal endothelial cells. *Comp Hepatol* **7**, 4 (2008). <https://doi.org:10.1186/1476-5926-7-4>
- 263 Xu, B. *et al.* Capillarization of hepatic sinusoid by liver endothelial cell-reactive autoantibodies in patients with cirrhosis and chronic hepatitis. *Am J Pathol* **163**, 1275-1289 (2003). [https://doi.org:10.1016/S0002-9440\(10\)63487-6](https://doi.org:10.1016/S0002-9440(10)63487-6)
- 264 Miyao, M. *et al.* Pivotal role of liver sinusoidal endothelial cells in NAFLD/NASH progression. *Lab Invest* **95**, 1130-1144 (2015). <https://doi.org:10.1038/labinvest.2015.95>
- 265 Balwani, S. *et al.* Regulation of NF-kappaB activation through a novel PI-3K-independent and PKA/Akt-dependent pathway in human umbilical vein endothelial cells. *PLoS One* **7**, e46528 (2012). <https://doi.org:10.1371/journal.pone.0046528>
- 266 Zheng, Y., Wang, J., Wang, J., Xie, H. & Zhao, T. Effect of Curcumol on the Fenestrae of Liver Sinusoidal Endothelial Cells Based on NF-kappaB Signaling Pathway. *Evid Based Complement Alternat Med* **2020**, 8590638 (2020). <https://doi.org:10.1155/2020/8590638>
- 267 Fujisawa, H. & Okuno, S. Regulatory mechanism of tyrosine hydroxylase activity. *Biochem Biophys Res Commun* **338**, 271-276 (2005). <https://doi.org:10.1016/j.bbrc.2005.07.183>
- 268 Nystoriak, M. A. *et al.* Ser1928 phosphorylation by PKA stimulates the L-type Ca²⁺ channel CaV1.2 and vasoconstriction during acute hyperglycemia and diabetes. *Sci Signal* **10** (2017). <https://doi.org:10.1126/scisignal.aaf9647>
- 269 Lu, X. *et al.* Macrophage Colony-stimulating Factor Mediates the Recruitment of Macrophages in Triple negative Breast Cancer. *Int J Biol Sci* **15**, 2859-2871 (2019). <https://doi.org:10.7150/ijbs.39063>
- 270 Hu, P. C. *et al.* CREB1/Lin28/miR-638/VASP Interactive Network Drives the Development of Breast Cancer. *Int J Biol Sci* **15**, 2733-2749 (2019). <https://doi.org:10.7150/ijbs.36854>
- 271 Metz, K. S. *et al.* Coral: Clear and Customizable Visualization of Human Kinome Data. *Cell Syst* **7**, 347-350 e341 (2018). <https://doi.org:10.1016/j.cels.2018.07.001>
- 272 Jiao, X. *et al.* Mevalonate Cascade and Neurodevelopmental and Neurodegenerative Diseases: Future Targets for Therapeutic Application. *Curr Mol Pharmacol* **10**, 115-140 (2017). <https://doi.org:10.2174/1874467209666160112125446>
- 273 Fan, Y., Gong, Y., Ghosh, P. K., Graham, L. M. & Fox, P. L. Spatial coordination of actin polymerization and ILK-Akt2 activity during endothelial cell migration. *Dev Cell* **16**, 661-674 (2009). <https://doi.org:10.1016/j.devcel.2009.03.009>

- 274 Furman, C. *et al.* Ena/VASP is required for endothelial barrier function in vivo. *J Cell Biol* **179**, 761-775 (2007). <https://doi.org:10.1083/jcb.200705002>
- 275 Luo, X. Y. *et al.* Autophagic degradation of caveolin-1 promotes liver sinusoidal endothelial cells defenestration. *Cell Death & Disease* **9** (2018). <https://doi.org:ARTN 576>
10.1038/s41419-018-0567-0
- 276 Ip, C. K., Cheung, A. N., Ngan, H. Y. & Wong, A. S. p70 S6 kinase in the control of actin cytoskeleton dynamics and directed migration of ovarian cancer cells. *Oncogene* **30**, 2420-2432 (2011). <https://doi.org:10.1038/onc.2010.615>
- 277 Scott, R. W. *et al.* LIM kinases are required for invasive path generation by tumor and tumor-associated stromal cells. *J Cell Biol* **191**, 169-185 (2010). <https://doi.org:10.1083/jcb.201002041>
- 278 Bamburg, J. R. & Bernstein, B. W. Roles of ADF/cofilin in actin polymerization and beyond. *F1000 Biol Rep* **2**, 62 (2010). <https://doi.org:10.3410/B2-62>
- 279 Ross-Macdonald, P. *et al.* Identification of a nonkinase target mediating cytotoxicity of novel kinase inhibitors. *Mol Cancer Ther* **7**, 3490-3498 (2008). <https://doi.org:10.1158/1535-7163.MCT-08-0826>
- 280 Trak-Smayra, V. *et al.* Pathology of the liver in obese and diabetic ob/ob and db/db mice fed a standard or high-calorie diet. *Int J Exp Pathol* **92**, 413-421 (2011). <https://doi.org:10.1111/j.1365-2613.2011.00793.x>
- 281 Millar, J. S., Cromley, D. A., McCoy, M. G., Rader, D. J. & Billheimer, J. T. Determining hepatic triglyceride production in mice: comparison of poloxamer 407 with Triton WR-1339. *Journal of Lipid Research* **46**, 2023-2028 (2005). <https://doi.org:10.1194/jlr.D500019-JLR200>
- 282 Meyer, J., Gonelle-Gispert, C., Morel, P. & Buhler, L. Methods for Isolation and Purification of Murine Liver Sinusoidal Endothelial Cells: A Systematic Review. *PLoS One* **11**, e0151945 (2016). <https://doi.org:10.1371/journal.pone.0151945>
- 283 Szafranska, K. *et al.* Quantitative analysis methods for studying fenestrations in liver sinusoidal endothelial cells. A comparative study. *Micron* **150**, 103121 (2021). <https://doi.org:10.1016/j.micron.2021.103121>
- 284 Chang, J. *et al.* A survey of compute nodes with 100 TFLOPS and beyond for supercomputers. *CCF Transactions on High Performance Computing* **6**, 243-262 (2024). <https://doi.org:10.1007/s42514-024-00188-w>
- 285 Kavzoglu, T. Increasing the accuracy of neural network classification using refined training data. *Environmental Modelling & Software* **24**, 850-858 (2009). <https://doi.org:10.1016/j.envsoft.2008.11.012>
- 286 Durkee, M. S., Abraham, R., Clark, M. R. & Giger, M. L. Artificial Intelligence and Cellular Segmentation in Tissue Microscopy Images. *Am J Pathol* **191**, 1693-1701 (2021). <https://doi.org:10.1016/j.ajpath.2021.05.022>
- 287 Gage, B. K. *et al.* Generation of Functional Liver Sinusoidal Endothelial Cells from Human Pluripotent Stem-Cell-Derived Venous Angioblasts. *Cell Stem Cell* **27**, 254-269 e259 (2020). <https://doi.org:10.1016/j.stem.2020.06.007>
- 288 Cogger, V. C. *et al.* The response of fenestrations, actin, and caveolin-1 to vascular endothelial growth factor in SK Hep1 cells. *Am J Physiol Gastrointest Liver Physiol* **295**, G137-G145 (2008). <https://doi.org:10.1152/ajpgi.00069.2008>
- 289 Guttmann-Raviv, N. *et al.* Semaphorin-3A and semaphorin-3F work together to repel endothelial cells and to inhibit their survival by induction of apoptosis. *J Biol Chem* **282**, 26294-26305 (2007). <https://doi.org:10.1074/jbc.M609711200>
- 290 Takahashi, T. *et al.* Plexin-neuropilin-1 complexes form functional semaphorin-3A receptors. *Cell* **99**, 59-69 (1999). [https://doi.org:10.1016/s0092-8674\(00\)80062-8](https://doi.org:10.1016/s0092-8674(00)80062-8)
- 291 Betz, N. *Compatibility of the Pierce BCA Protein Assay with Promega Lysis Buffers and Lytic Assay Reagents*, <<https://www.promega.de/en/resources/pubhub/enotes/compatibility-of-pierce-bca-protein-assay-with-promega-lysis-buffers-and-lytic-reagents/>> (2003).

- 292 Kus, E. *et al.* LSEC Fenestrae Are Preserved Despite Pro-inflammatory Phenotype of Liver Sinusoidal Endothelial Cells in Mice on High Fat Diet. *Front Physiol* **10**, 6 (2019). <https://doi.org/10.3389/fphys.2019.00006>
- 293 Steffan, A. M., Gendrault, J. L. & Kirn, A. Increase in the number of fenestrae in mouse endothelial liver cells by altering the cytoskeleton with cytochalasin B. *Hepatology* **7**, 1230-1238 (1987). <https://doi.org/10.1002/hep.1840070610>
- 294 Pasarin, M. *et al.* Sinusoidal endothelial dysfunction precedes inflammation and fibrosis in a model of NAFLD. *PLoS One* **7**, e32785 (2012). <https://doi.org/10.1371/journal.pone.0032785>
- 295 Carpenter, B. *et al.* VEGF is crucial for the hepatic vascular development required for lipoprotein uptake. *Development* **132**, 3293-3303 (2005). <https://doi.org/10.1242/dev.01902>
- 296 Herzog, B., Pellet-Many, C., Britton, G., Hartzoulakis, B. & Zachary, I. C. VEGF binding to NRP1 is essential for VEGF stimulation of endothelial cell migration, complex formation between NRP1 and VEGFR2, and signaling via FAK Tyr407 phosphorylation. *Mol Biol Cell* **22**, 2766-2776 (2011). <https://doi.org/10.1091/mbc.E09-12-1061>
- 297 Koch, S. & Claesson-Welsh, L. Signal transduction by vascular endothelial growth factor receptors. *Cold Spring Harb Perspect Med* **2**, a006502 (2012). <https://doi.org/10.1101/cshperspect.a006502>
- 298 Takamatsu, H. & Kumanogoh, A. Diverse roles for semaphorin-plexin signaling in the immune system. *Trends Immunol* **33**, 127-135 (2012). <https://doi.org/10.1016/j.it.2012.01.008>
- 299 Luo, S. *et al.* NRP2 promotes atherosclerosis by upregulating PARP1 expression and enhancing low shear stress-induced endothelial cell apoptosis. *FASEB J* **36**, e22079 (2022). <https://doi.org/10.1096/fj.202101250RR>
- 300 Pellet-Many, C., Frankel, P., Jia, H. & Zachary, I. Neuropilins: structure, function and role in disease. *Biochem J* **411**, 211-226 (2008). <https://doi.org/10.1042/BJ20071639>
- 301 Zachary, I. Neuropilins: role in signalling, angiogenesis and disease. *Chem Immunol Allergy* **99**, 37-70 (2014). <https://doi.org/10.1159/000354169>
- 302 Nagatsu, T. The catecholamine system in health and disease - Relation to tyrosine 3-monooxygenase and other catecholamine-synthesizing enzymes. *Proceedings of the Japan Academy Series B-Physical and Biological Sciences* **82**, 388-415 (2006). <https://doi.org/DOI10.2183/pjab.82.388>
- 303 Yokomori, H. *et al.* LSEC in the ageing liver. *Textbook of Hepatology: From Basic Science to Clinical Practice* **29**, 77 (2008).
- 304 Richardson, P. & Withrihngton, P. Responses of the canine hepatic arterial and portal venous vascular beds to dopamine. *European Journal of Pharmacology* **48**, 337--349 (1977).
- 305 Oda, M. *et al.* in *Gastrointestinal Microcirculation* Vol. 17 103-128 (Karger Publishers, 1990).
- 306 Hou, S., Guan, H. & Ricciardi, R. P. Phosphorylation of serine 337 of NF-kappaB p50 is critical for DNA binding. *J Biol Chem* **278**, 45994-45998 (2003). <https://doi.org/10.1074/jbc.M307971200>
- 307 Luedde, T. & Schwabe, R. F. NF-kappaB in the liver--linking injury, fibrosis and hepatocellular carcinoma. *Nat Rev Gastroenterol Hepatol* **8**, 108-118 (2011). <https://doi.org/10.1038/nrgastro.2010.213>
- 308 Gorovoy, M. *et al.* LIM kinase 1 coordinates microtubule stability and actin polymerization in human endothelial cells. *J Biol Chem* **280**, 26533-26542 (2005). <https://doi.org/10.1074/jbc.M502921200>
- 309 Yokomori, H. New insights into the dynamics of sinusoidal endothelial fenestrae in liver sinusoidal endothelial cells. *Med Mol Morphol* **41**, 1-4 (2008). <https://doi.org/10.1007/s00795-007-0390-7>

- 310 Tateya, S. *et al.* The role of vasodilator-stimulated phosphoprotein (VASP) in the control of hepatic gluconeogenic gene expression. *PLoS One* **14**, e0215601 (2019). <https://doi.org/10.1371/journal.pone.0215601>
- 311 Price, C. J. & Brindle, N. P. J. Vasodilator-stimulated phosphoprotein is involved in stress-fiber and membrane ruffle formation in endothelial cells. *Arteriosclerosis Thrombosis and Vascular Biology* **20**, 2051-2056 (2000). <https://doi.org/10.1161/01.Atv.20.9.2051>
- 312 Clement, O., Puceat, M., Walsh, M. P. & Vassort, G. Protein kinase C enhances myosin light-chain kinase effects on force development and ATPase activity in rat single skinned cardiac cells. *Biochem J* **285 (Pt 1)**, 311-317 (1992). <https://doi.org/10.1042/bj2850311>
- 313 Riggio, M. *et al.* AKT1 and AKT2 isoforms play distinct roles during breast cancer progression through the regulation of specific downstream proteins. *Sci Rep* **7**, 44244 (2017). <https://doi.org/10.1038/srep44244>
- 314 Salminen, A. & Kaarniranta, K. Insulin/IGF-1 paradox of aging: regulation via AKT/IKK/NF-kappaB signaling. *Cell Signal* **22**, 573-577 (2010). <https://doi.org/10.1016/j.cellsig.2009.10.006>
- 315 Creeden, J. F. *et al.* Hepatic kinome atlas: An in-depth identification of kinase pathways in liver fibrosis of humans and rodents. *Hepatology* **76**, 1376-1388 (2022). <https://doi.org/10.1002/hep.32467>
- 316 Sayuti, N. H. *et al.* Preventative and Therapeutic Effects of Astaxanthin on NAFLD. *Antioxidants (Basel)* **12** (2023). <https://doi.org/10.3390/antiox12081552>
- 317 Geraud, C. *et al.* Liver sinusoidal endothelium: a microenvironment-dependent differentiation program in rat including the novel junctional protein liver endothelial differentiation-associated protein-1. *Hepatology* **52**, 313-326 (2010). <https://doi.org/10.1002/hep.23618>
- 318 Verin, A. D. *et al.* Microtubule disassembly increases endothelial cell barrier dysfunction: role of MLC phosphorylation. *Am J Physiol Lung Cell Mol Physiol* **281**, L565-574 (2001). <https://doi.org/10.1152/ajplung.2001.281.3.L565>
- 319 Bergen, J. *et al.* Exposure to dietary fatty acids oleic and palmitic acid alters structure and mechanotransduction of intestinal cells in vitro. *Arch Toxicol* **97**, 1659-1675 (2023). <https://doi.org/10.1007/s00204-023-03495-3>
- 320 Guest, P. C. & Rahmoune, H. Characterization of the db/db mouse model of type 2 diabetes. *Pre-Clinical Models: Techniques and Protocols*, 195-201 (2019).
- 321 Manicardi, N. *et al.* Transcriptomic Profiling of the Liver Sinusoidal Endothelium during Cirrhosis Reveals Stage-Specific Secretory Signature. *Cancers (Basel)* **13** (2021). <https://doi.org/10.3390/cancers13112688>
- 322 Moin, A. S. M., Al-Qaissi, A., Sathyapalan, T., Atkin, S. L. & Butler, A. E. Soluble Neuropilin-1 Response to Hypoglycemia in Type 2 Diabetes: Increased Risk or Protection in SARS-CoV-2 Infection? *Front Endocrinol (Lausanne)* **12**, 665134 (2021). <https://doi.org/10.3389/fendo.2021.665134>
- 323 Elpek, G. O. Neuropilins and liver. *World J Gastroenterol* **21**, 7065-7073 (2015). <https://doi.org/10.3748/wjg.v21.i23.7065>
- 324 Polyzos, S. A. & Goulis, D. G. Menopause and metabolic dysfunction-associated steatotic liver disease. *Maturitas* **186**, 108024 (2024). <https://doi.org/10.1016/j.maturitas.2024.108024>
- 325 Van Kempen, T. A., Milner, T. A. & Waters, E. M. Accelerated ovarian failure: a novel, chemically induced animal model of menopause. *Brain Res* **1379**, 176-187 (2011). <https://doi.org/10.1016/j.brainres.2010.12.064>
- 326 Shimizu, I. & Ito, S. Protection of estrogens against the progression of chronic liver disease. *Hepato Res* **37**, 239-247 (2007). <https://doi.org/10.1111/j.1872-034X.2007.00032.x>
- 327 Hutchison, A. L., Tavaglione, F., Romeo, S. & Charlton, M. Endocrine aspects of metabolic dysfunction-associated steatotic liver disease (MASLD): Beyond insulin resistance. *J Hepatol* **79**, 1524-1541 (2023). <https://doi.org/10.1016/j.jhep.2023.08.030>

- 328 Pucci, G. *et al.* Sex- and gender-related prevalence, cardiovascular risk and therapeutic approach in metabolic syndrome: A review of the literature. *Pharmacol Res* **120**, 34-42 (2017). <https://doi.org:10.1016/j.phrs.2017.03.008>
- 329 Regitz-Zagrosek, V. & Seeland, U. Sex and gender differences in clinical medicine. *Sex and Gender Differences in Pharmacology*, 3-22 (2012).
- 330 Migliore, L., Nicoli, V. & Stoccoro, A. Gender Specific Differences in Disease Susceptibility: The Role of Epigenetics. *Biomedicines* **9** (2021). <https://doi.org:10.3390/biomedicines9060652>
- 331 Ji, H., Cheng, S. & Heart-Liver Axis Research, C. Sex differences in prevalence and prognosis of steatotic liver disease phenotypes: Biological sex matters. *J Hepatol* **80**, e68-e69 (2024). <https://doi.org:10.1016/j.jhep.2023.08.013>
- 332 Booijink, R., Ramachandran, P. & Bansal, R. Implications of innate immune sexual dimorphism for MASLD pathogenesis and treatment. *Trends Pharmacol Sci* (2024). <https://doi.org:10.1016/j.tips.2024.05.004>
- 333 Bockhorn, M. *et al.* VEGF is important for early liver regeneration after partial hepatectomy. *J Surg Res* **138**, 291-299 (2007). <https://doi.org:10.1016/j.jss.2006.07.027>
- 334 Liu, X. *et al.* Semaphorin 3A Shifts Adipose Mesenchymal Stem Cells towards Osteogenic Phenotype and Promotes Bone Regeneration In Vivo. *Stem Cells Int* **2016**, 2545214 (2016). <https://doi.org:10.1155/2016/2545214>
- 335 Mohamed, R. *et al.* Urinary semaphorin 3A correlates with diabetic proteinuria and mediates diabetic nephropathy and associated inflammation in mice. *J Mol Med (Berl)* **92**, 1245-1256 (2014). <https://doi.org:10.1007/s00109-014-1209-3>
- 336 Kikuchi, K. *et al.* In vitro and in vivo characterization of a novel semaphorin 3A inhibitor, SM-216289 or xanthofulvin. *J Biol Chem* **278**, 42985-42991 (2003). <https://doi.org:10.1074/jbc.M302395200>
- 337 Zheng, C. J., Sohn, M. J. & Kim, W. G. Vinaxanthone, a new FabI inhibitor from *Penicillium* sp. *J Antimicrob Chemother* **63**, 949-953 (2009). <https://doi.org:10.1093/jac/dkp058>
- 338 Ivakhnitskaia, E., Chin, M. R., Siegel, D. & Guaiquil, V. H. Vinaxanthone inhibits Semaphorin3A induced axonal growth cone collapse in embryonic neurons but fails to block its growth promoting effects on adult neurons. *Sci Rep* **11**, 13019 (2021). <https://doi.org:10.1038/s41598-021-92375-w>
- 339 Zhou, J. *et al.* Inhibition of neuropilin-1 improves non-alcoholic fatty liver disease in high-fat-diet induced obese mouse. *Minerva Endocrinol (Torino)* **48**, 194-205 (2023). <https://doi.org:10.23736/S2724-6507.22.03895-7>
- 340 Ito, Y. *et al.* Age-related changes in the hepatic microcirculation in mice. *Exp Gerontol* **42**, 789-797 (2007). <https://doi.org:10.1016/j.exger.2007.04.008>
- 341 Hunt, N. J. *et al.* Manipulating fenestrations in young and old liver sinusoidal endothelial cells. *Am J Physiol Gastrointest Liver Physiol* **316**, G144-G154 (2019). <https://doi.org:10.1152/ajpgi.00179.2018>
- 342 Mohamad, M. *et al.* Ultrastructure of the liver microcirculation influences hepatic and systemic insulin activity and provides a mechanism for age-related insulin resistance. *Aging Cell* **15**, 706-715 (2016). <https://doi.org:10.1111/accel.12481>
- 343 Gallage, S. *et al.* A researcher's guide to preclinical mouse NASH models. *Nat Metab* **4**, 1632-1649 (2022). <https://doi.org:10.1038/s42255-022-00700-y>
- 344 Maione, F. *et al.* Semaphorin 3A overcomes cancer hypoxia and metastatic dissemination induced by antiangiogenic treatment in mice. *J Clin Invest* **122**, 1832-1848 (2012). <https://doi.org:10.1172/JCI58976>
- 345 Karlsson, M. *et al.* A single-cell type transcriptomics map of human tissues. *Sci Adv* **7** (2021). <https://doi.org:10.1126/sciadv.abh2169>
- 346 Uhlen, M. *et al.* Proteomics. Tissue-based map of the human proteome. *Science* **347**, 1260419 (2015). <https://doi.org:10.1126/science.1260419>

- 347 *CDH5 protein expression summary - The Human Protein Atlas*,
<<https://www.proteinatlas.org/ENSG00000179776-CDH5>> (
- 348 Rastovic, U. *et al.* Human Precision-Cut Liver Slices: A Potential Platform to Study Alcohol-
Related Liver Disease. *Int J Mol Sci* **25** (2023). <https://doi.org/10.3390/ijms25010150>
- 349 Yamazaki, R. *et al.* The Semaphorin 3A inhibitor SM-345431 preserves corneal nerve and
epithelial integrity in a murine dry eye model. *Sci Rep* **7**, 15584 (2017).
<https://doi.org/10.1038/s41598-017-15682-1>
- 350 Bjorkegren, J. L. M. & Lusis, A. J. Atherosclerosis: Recent developments. *Cell* **185**, 1630-1645
(2022). <https://doi.org/10.1016/j.cell.2022.04.004>
- 351 Fraser, R., Clark, S. A., Day, W. A. & Murray, F. E. Nicotine decreases the porosity of the rat
liver sieve: a possible mechanism for hypercholesterolaemia. *Br J Exp Pathol* **69**, 345-350
(1988).
- 352 Fu, Y. *et al.* Inhibition of semaphorin-3a alleviates lipopolysaccharide-induced vascular
injury. *Microvasc Res* **142**, 104346 (2022). <https://doi.org/10.1016/j.mvr.2022.104346>

12. Declaration

Ich, Sydney Miriam Balkenhol, versichere an Eides statt, dass die vorliegende Dissertation von mir selbstständig und ohne unzulässige fremde Hilfe unter Beachtung der „Grundsätze zur Sicherung guter wissenschaftlicher Praxis an der Heinrich-Heine-Universität Düsseldorf“ erstellt worden ist.



Düsseldorf, 22. August 2024

Sydney Balkenhol

13. Acknowledgements

First and foremost, I'd like to thank Prof. Dr. Eckhard Lammert for being a great doctoral supervisor by always providing guidance, knowledge, and support, whenever it was needed, and suggesting me for the scholarship that allowed me to do my PhD at his lab.

Thank you, Ecki!

Secondly, I would also like to thank Prof. Dr. Simone Prömel for being my second supervisor.

Thirdly, I would like to thank Dr. Daniel Eberhard for being my co-supervisor, and for always having a sympathetic ear for both scientific and non-scientific matters, for his ever-present support and guidance through the rollercoaster called PhD, and always sharing his vast knowledge. I especially thank you for taking me on as a master student nearly 5 years ago, allowing me to find my passion for fenestrae, thus making this PhD project possible.

I'd also like to thank all current and former lab members of the "lablammert" for a great time during my PhD! Thank you, Paula, Philip, Leonie, Jana, Oliver, Fabienne, Angela, Linda, Elena, and Celina for making a great team and a fun time!

I would also like to thank Esther, Barbara, Silke, and Andrea for being there for radio music in the lab, experimental support and organizational questions, and a good time during lunch hour!

Philip and Paula, you already know you are the definition of **office besties** and I couldn't have asked for better company in-between experiments and outside of the lab! I'm so thankful that life brought us together and I now know EXACTLY why German trash TV is so good and glühwein should be enjoyed with care ♥

I'd also like to thank my boyfriend, Niklas B. for his never-ending support and love during all these ups and downs! I really do not know how I could've done this without you and only god knows how many times you had to dry tears because some stupid cells suddenly decided to look bad under the SEM (many, many times!). Even though there were times where this degree got the best of me, I will be forever thankful that it brought me to you!



I would also like to thank the old WG for being there for me through green and not so green and always being interested and listening to what I do at work. Thank you all for many great memories and laughs during that time! Nils, I especially thank you, for all your mental support, open ear, and showing me what friendship is all about :) (and also giving people flowers when I'm not around!)

Last, but most definitely not least, I'd like to thank my wonderful family for being my biggest cheerleaders! Thank you Mum (Danke, dass auch wenn ich hier was ganz Nettes mache, du mir immer das Gefühl gegeben hast, so oder so stolz auf mich zu sein!) and Paps (Danke, dass du immer hinter mir gestanden hast, und mir gezeigt hast, wie wichtig es ist an sich selbst zu glauben!) , Tina (sog. Mama Nr. ②, danke für dein immer offenes Ohr und dass du mir nie böse warst, dass ich dauernd heimlich den Pudding aufgeessen hab!) and Bernd (sog. Papa Nr. ②, danke, dass du in all dem Wirbel, den das Leben bringt, mir immer ein Ruhepol mit einem großen Lächeln warst ☺), Oma and Opa (Danke für all die Grillabende und Reisen, ob groß oder klein, die wir gemacht haben, mein Jott haben wir jelacht und jesoffen in der Zeit!), Neve (der kleine Bruder), Elli (die große-kleine Schwester), und Lissi (die kleine-kleine Schwester)!

Ohne euch wäre ich niemals da, wo ich jetzt bin! ♥♥♥